Advanced Source Reconstruction and Volume Conductor Modeling for Fetal Magnetocardiography

BY

Rong Tao

Submitted to the graduate degree program in Bioengineering and the Graduate Faculty of the University of Kansas in partial fulfillment of the requirements for the degree of Doctor of Philosophy.

_____

Chairperson, Dr. Carl Luchies

_____

Co-Chair, Dr. Mihai Popescu

_____

Dr. Shannon Blunt

_____

Dr. William M. Brooks

_____

Dr. Xinmai Yang

Date defended: January 27th, 2015

The Dissertation Committee for Rong Tao certifies that this is the approved version of the following dissertation:

Advanced Source Reconstruction and Volume Conductor Modeling for Fetal Magnetocardiography

_____

Chairperson Dr.Carl Luchies

Date approved:

Abstract

Fetuses that are identified with cardiac hypotrophy, hypertension and metabolic anomalies have higher risk of suffering from various health problems in their later life. Therefore, the early detection of congenital heart anomalies is critical for monitoring or prompt interventions, which can reduce the risks of congestive heart failure. Compared to adult cardiac monitoring, fetal electrophysiological heart monitoring using fetal ECG is extremely difficult due to the low signal amplitude and interferences from the maternal cardiac signal and to the complex environment inside the mother's womb. This problem is even worse in conditions such as diabetic pregnancies because of further signal reduction due to maternal obesity. At the same time, the prevalence of congenital heart anomalies is higher for fetuses of diabetic mothers. The purpose of this thesis is to develop and test fetal magnetocardiography (fMCG) techniques as an alternative diagnostic tool for the detection and monitoring of the fetal heart. fMCG is a novel technique that records the magnetic fields generated by the fetal heart's electric activity. From the aspect of signal processing, magnetic signals generated by the fetal heart are less affected by the low electrical conductivity of the surrounding fetal and maternal tissues compared to the electric signals recorded over the maternal abdomen, and can provide reliable recordings as early as 12 weeks of gestation. However, the fetal heart signals recorded with an array of magnetic sensors at a small distance from the maternal abdomen are affected by the source-to-sensor distance as well as by the geometry of the volume conductor, which is variable in different subjects or in the same subject when recordings are made at

different gestational ages. The scope of this thesis is to develop a novel methodology for modeling the fetal heart and volume conductor and to use advanced source reconstruction techniques that can reduce the effect of these confounding factors in evaluating heart magnetic signals. Furthermore, we aim to use these new methods for developing a normative database of fMCG metrics at different gestational ages and test their reliability to detect abnormal patterns of cardiac electrophysiology in pregnancies complicated by maternal diabetes.

In the first part of the thesis, we review three current fetal heart monitoring modalities, including fetal electrocardiography (ECG), ultrasonography, and fetal magnetocardiography (fMCG). The advantages and drawbacks of each technique are comparatively discussed. Finally, we discuss the developmental changes of fetal heart through gestation as well as the electromagnetic characteristics of the fetal cardiac activation.

Acknowledgements

I would like to thank Dr. Mihai Popescu for advising and administrating the project, Dr. Anda Popescu and Dr. Drake for data collection and signal preprocessing, and the study coordinator JoAnn Lierman. RNC, PhD. This work was supported in part by grant R21EB006776 from the National Institute of Biomedical Imaging and Bioengineering.

Table of Contents

CHAPTER 1 FETAL MAGNETOCARDIOGRAPHY: A NEW METHOD FOR THE EVALUATION OF THE FETAL HEART *IN UTERO*

1.1. Techniques for monitoring the fetal heart in clinical settings

A variety of non-invasive techniques exists for obtaining information about the anatomy and function of the fetal heart. Three of the most recognized methods are fetal electrocardiography (fECG), ultrasound imaging (including B-mode, Doppler and M-mode ultrasound) and fetal magnetocardiography (fMCG). Back in the 19th century, fetal heart rate was monitored by means of auscultation. Later in 1906, Cremer *et al.* (Cremer 1906) was the first to record fetal heart electrical activity by attaching electrodes on the mother's abdomen to pick up fetal QRS waves. In the more recent years, numerous methods have been developed to investigate the electromagnetic characteristics of the fetal heart based on fECG (Mazzeo 1994, Peters *et al.* 2001, Quartero *et al.* 2002). Despite the advantage of being a low cost and easily accessible mean of assessing the fetal heart function, fECG remains difficult to perform at early gestation due to the weak fetal cardiac signal amplitude. In addition, fECG is severely limited around 28 to 32 weeks of gestation because of the poor signal-to-noise ratio due to the formation of vernix caseosa around the fetal body, which acts as a strong electrical insulator (Comani *et al.* 2004).

Another widely used fetal heart monitoring method is based on ultrasound techniques, including B-mode ultrasound, Doppler and M-mode ultrasound.

Ultrasound based techniques became popular during 1980s and are now the most widely used monitoring method in clinical settings. Conventional B-mode is primarily used to aquire two-dimensional cross-sectional images of the fetus and to provide structural information about the fetal body such as head circumference (HC), biparietal diameter (BPD), abdominal circumference (AC) and femur lengh (FL). Altough it can also provide information about the fetal heart structure, this anatomical information is typically achieved with a greater level of detail using M-mode ultrasound. In M-mode imaging, cross-sections of the fetal heart are scanned continuously to increase the temporal resolution of the readings and allow structural measurements to be performed and compared at the same time during the cardiac cycle. M-mode ultrasound imaging provides important fetal heart structural information such as left- / right-ventricular wall thickness, left-/right-ventricular diastolic/systolic diameter, and interventricular septum thickness. To assess the accuracy of the biomagnetic techniques, B-mode and M-mode ultrasound techniques were used in our study and compared to the fMCG. Apart from B-mode and M-mode ultrasound imaging which provide structural information of the fetus and fetal heart, Doppler ultrasound imaging is used to investigate the fetal circulation and to obtain fetal *cardiogtocogram* for the purpose of measuring fetal heart rate. This technique measures Doppler shifts that occur when particles such as blood cells or structures such as heart wall shift from the ultrasound transducer (Zheng *et al.* 2006). This allows for monitoring the fetal heart and for the detection of fetal arrhythmias. More recently, three-dimensional (3D) color-Doppler echocardiography has been developed

to provide volumetric information of the fetus. In this technique, sound waves are sent at different angles, and the returning echoes are reconstructed later to a build a 3D fetus model (Chaoui *et al.* 2004). Similar to 3D Doppler, 4D fetal Doppler echocardiography allow the 3-D ultrasound image to be rendered in real time, thus to minimize the influence of lag during image reconstruction.

Although the ultrasound-based fetal heart monitoring, such as B-mode, M-mode and Doppler ultrasound are nowadays the most used methods in clinical settings, these modalities have a number of limitations. For example, ultrasound M-mode analysis allows an estimation of atrial and ventricular coordination, as well as an estimation of the PR intervals but provide little information about the electrophysiological aspects of the fetal heart function. Also, recordings of Doppler ultrasound imaging are complicated by artifacts and noise, and require the use of advanced signal processing techniques (Pieri *et al.* 2001). When interpreting the fetal heart rate, ultrasound based methods typically report an averaged heart rate without providing a more precise information about the beat-to-beat variability (Peters *et al.* 2001). Fetal electrocardiography (fECG) can overcome these difficulties and offer the potential for monitoring beat-to-beat variability and performing electrocardiogram morphological analysis. Its disadvantage, however, is that its reliability is only of about 60 % (Peters *et al.* 2001), although it is the only technique that offers truly long-term ambulatory monitoring. All ultrasound techniques require an optimal positioning of the ultrasound probe according to the fetal positioning and good quality images, which is not always possible thus limiting the success rate of these

measurements. Another concern about obstetric ultrasonography is the safety issue. Although ultrasound scanning is generally safe for fetus, some studies have shown that prolonged ultrasound exposure leads to abnormal brain cell migration in mice (Ang *et al.* 2006). In a review summarizing studies of obstetrical ultrasound safety across thirty years, they find that the safety of obstetrical ultrasound screen relies largely on ultrasound users (Houston *et al.* 2009). This issue is generally smaller for B-mode imaging, but bigger for Doppler modalities. In addition, first trimester Doppler exams are strongly discouraged due to potential temperature elevations and the teratogenicity of hyperthermia (ACOG 1997).

1.2. Introduction of SQUID system and fetal magnetocardiography

1.2.1. The development of SQUID system for fetal magnetocardiography

The invention of superconducting quantum interference device (SQUID) -magnetometer system makes it possible to detect magnetic fields generated outside of the body by the heart electrical currents (Baule and McFee 1963). The first experiment was performed using two large coils over the subject's chest. Later David Cohen *et al.* (Cohen *et al.* 1970) tested magnetic shielded rooms to reduce the background environmental noise. The first SQUID sensor was later built of a superconducting loop interrupted by two josephson junctions. Until the middle of 1980s, almost all biomagnetic measurements were carried out using single-channel magnetometers with pickup and compensation coils wound of superconducting wire on three-dimensional formers. Because the single channel system suffered from low

sensitivity and a high interference from external electromagnetic sources, researchers soon developed multichannel SQUID for mapping simultaneously a wider spatial pattern of the magnetic field caused by various sources (Kleiner *et al.* 2004). During the first period, most biomagnetic systems were used to record signals from the adult heart and brain. The first fetal magnetocardiography recording was performed by Kariniemi *et al*. (Kariniemi *et al.* 1974) using a sensor setup developed originally for adult recordings. Following this, other researchers designed magnetometer arrays specifically for fetal recordings (Kandori *et al.* 1999, SE *et al.* 2001). Using these biomagnetometer systems, several studies (Kahler *et al.* 2001, Wakai *et al.* 1998b, Wakai *et al.* 2000, van Leeuwen *et al.* 1999, Menendez *et al.* 2001) documented fetal arrthymia and congenital heart disease by means of fetal magnetocardiography.

1.2.2. Reliability of fetal magnetocardiography (fMCG) in fetal cardiac assessment

The development of SQUID sensors makes fMCG an attractive technique that records the magnetic field generated by the electrical currents flowing within the fetal heart. The major advantage of fMCG compared to fECG is the notably superior signal quality as the magnetic field recordings are not compromised by the presence of tissues with low electrical conductivity (Cuffin 1978). The magnetic fields generated by fetal myocardial currents allow high resolution recordings from the second trimester of gestation to birth. Several fMCG studies in healthy pregnancies aimed to characterize developmental changes in signal amplitude, cardiac time intervals and heart rate variability (Leuthold *et al.* 1999, Horigome *et al.* 2000, Kähler *et al.* 2002,

van Leeuwen *et al.* 2004b). It has been also proven that using these measurements of fetal heart electrophysiology fMCG enables the identification of certain pathologies, including intrauterine growth retardation (Leeuwen *et al.* 2000), congenital heart disease (Wakai *et al.* 1998a), long QT syndrome (Hamada *et al.* 1999, Cuneo *et al.* 2003), and supraventricular tachycardia (Wakai *et al.* 2003).

fMCG was shown to provide high quality recordings despite maternal obesity and/or presence of vernix caseosa (Peters *et al.* 2001). Several studies have demonstrated unique advantages of fMCG in characterizing fetal arrhythmias in obese patients, where conventional ultrasound-based methods can fail (Comani *et al.* 2004). While most fMCG studies were limited to investigating the coarse temporal waveform features on the recorded sensor signals, we aimed in this study to develop and test novel strategies that enable access to more accurate details of the fetal cardiac signal amplitude and morphology, overcoming difficulties due to: 1) the lack of control on fetal position and orientation relative to the sensing system, and 2) the unknown geometry of the tissues surrounding the fetal heart, which can modulate the measured magnetic field at each sensor through volume conductor effects. The proposed approach is based on signal acquisition and processing methodology developed in our laboratory, which combines fMCG data with 3D ultrasound images of the feto-abdominal anatomy, thus allowing advanced source reconstruction techniques for estimation of the fetal cardiac vectors to address the above mentioned limitations.

1.3. Layout of the thesis

In chapter 1, three different techniques (fetal ECG, ultrasound imaging and fetal MCG) of monitoring fetal heart are compared and discussed. While ultrasound imaging records structural images of fetal heart, fetal ECG and fetal MCG can gain additional information about cardiac electrophysiology. Among them, ultrasound techniques are the most widely used in the clinical environment. However, previous studies pointed out to its limited success rate in diagnosing congenital heart disease in diabetic patients. On the other hand, due to the poor signal quality, fetal ECG is rarely recorded successfully in obese patients, and it is considerably compromised by the natural formation of the electrically insulating vernix caseosa, a naturally occurring fetal skin barrier produced in late pregnancy as a result of sebaceous and epidermal lipids combined with desquamation of maturing fetal corneocytes.

In chapter 2, we discussed the developmental changes of fetal heart through gestation. The physiological basis of bioelectromagnetism is also covered in this chapter.

In chapter 3 the concept of volume conductor and the volume conductor effect on the forward electromagnetic field will be introduced. The volume conductor consists of all tissues surrounding the fetal heart that allow the flow of volume currents. As the currents generated in the fetal heart flow through these tissues, the geometry and conductivity of these tissues influence the magnetic field recorded at each sensor position over the maternal abdomen. Since the direct measurement of the current density in the fetus and maternal abdomen is not possible in practice, simulations are

used in our study in order to estimate the effects of the volume conductor.

In this chapter, we introduce two different kinds of volume conductor models which were widely used in other biomagnetic applications such as magnetoencephalography (MEG): spherical volume conductor and realistic volume conductor. The latter is reconstructed from a series of 2D ultrasound images of the fetal body and maternal abdomen. We also discussed two source modeling approaches to represent the fetal cardiac source: the single current dipole model and the multiple-dipole model. These cardiac source models combined with the volume conductor models will be used to calculate the forward magnetic fields in simulations studies in chapter 5. The mathematical basis as well as the numerical techniques (Boundary Element Method) needed to perform the simulations are discussed as well in chapter 3.

Chapter 4 describes the experimental design of the study as well as signal preprocessing using ICA filtering. In this chapter the basic structure of SQUID system (Omega 2000 system produced by CTF Systems Inc.) located at Hoglund Brain Imaging Center is described. Then ultrasound system setup is also introduced, which uses a GE Logiq-P5 ultrasound system interfaced with a 4C 1.4-4.8 MHz wide band convex transducer.

In chapters 5, we perform a series of simulation experiments to estimate the effect of volume conductor modeling on the estimation of cardiac vectors in fetal magnetocardiography. The accuracy simulations using spherical volume conductor and realistic volume conductor are discussed and compared.

In chapter 6 and 7, we apply the methodology in chapter 5 to two different groups of subjects: fetus of diabetic mothers and control group. A normative database of metrics (amplitude, latencies and time integrals) obtained with the proposed methodology to characterize the reconstructed fetal cardiac vectors at different gestational ages in control subjects is presented. To evaluate the effectiveness of the proposed methodology in detecting abnormal patterns of fetal heart electrophysiology, the proposed methodology is used to investigate if fetal cardiac hypertrophy (assessed by m-mode ultrasound) is reflected in abnormal values of the cardiac vector metrics. To achieve this aim, we compare the reconstructed fetal cardiac vectors in uncomplicated pregnancies and in a group of pregnant women with diabetes mellitus. This choice (addressed in more detail in the next section of this chapter) is based on previous evidence showing a high incidence of fetal cardiac hypertrophy associated with maternal diabetes (Weber *et al.* 1991, Rizzo *et al.* 1995, Veille *et al.* 1992, Gandhi *et al.* 1995a).

Finally, in chapter 8 summaries will be formulated and recommendations for further improvement.

1.4. Fetal cardiac assessment in diabetic pregnancies

Based on the 2002 birth data in the US (Martin *et al.* 2003), maternal diabetes affects more than 321,760 of the 4,021,726 live birth and is a significant cause of maternal and fetal morbidity. A significant number of previous studies used ultrasound-based techniques to assess the general evolution of fetal myocardium

throughout gestation, the influence of poor maternal metabolic control on fetal heart structure and function, and the evolution of congenital heart disease (Hornberger 2006). However, a recent retrospective study reported that nearly one third of diabetic pregnant women had incomplete imaging due to factors like maternal obesity and/or suboptimal fetal positioning (Sekhavat *et al.* 2010), difficulties that cannot be simply overcome by more experienced experts or advanced ultrasound devices (Hendler *et al.* 2004). Since the current assessment of fetal cardiac development can be significantly limited by maternal obesity, it is of great importance to develop alternative methods that can fill the gap introduced by the ultrasound limitations in screening diabetic patients.

fMCG has proved the unique advantage for assessment of fetal cardiac electrophysiology despite of maternal obesity (Weber *et al.* 1991, Rizzo *et al.* 1995, Veille *et al.* 1992, Gandhi *et al.* 1995a). Hence, one of the specific objectives of our study is to evaluate the effectiveness of the proposed methodology in detecting abnormal patterns of fetal heart electrophysiology, by testing the hypothesis that fetal cardiac hypertrophy (assessed by m-mode ultrasound) is reflected in abnormal values of the cardiac vector metrics. To achieve this aim, we will compare the reconstructed fetal cardiac vectors between normal subjects and subjects from a group of pregnant women with diabetes mellitus.

CHAPTER 2 FETAL HEART ELECTROPHYSIOLOGY

The electromagnetic characteristics of fetal cardiac signal are different from adult heart in that it is influence by fetal heart development inside uterus. This chapter will discuss the basis of fetal magnetocardiography from the aspect of fetal heart growth and electrophysiology, such as ion channels and propagation of action potential.

2.1. Fetal heart development

The heart is the first functional organ in human embryo. It begins with the formation of two endocardial tubes which merge to form primitive heart tube (Moorman and Lamers 1994). The primitive tube soon converts into four cardiac chambers and paired arterial trunks. The fetal heart begins beating at approximately 28 days of conception. The atrium septum divides the atrium in two at around 30 days. Myocardial walls, or so called primary myocardium, of the heart tube also form at this stage (Moorman *et al.* 2003)(table 2.1).

The walls of the fetal heart are composed of cardiac muscle, called *myocardium*. Cardiac muscle separates fetal heart into four compartments: the right and left ventricles. The left ventricular free wall and the septum are thicker than the right ventricular wall. This is because the left ventricle pumps blood to the systemic circulation, where the pressure is considerably higher than for the pulmonary circulation, which arises from right ventricular outflow. The cardiac muscles are oriented spirally and are divided into four groups: two groups of muscle winds around

the outside of both ventricles. The third group winds around both ventricles, while the fourth group winds only around the left ventricle. In this case, the myocardium is oriented more tangentially than radically. Therefore, the magnetic field produced by heart muscle cells (*myocytes*) activation has a radial distribution, pointing from heart apex to bottom (figure 2.1).

Table 2.1 Timeline for fetal heart formation (Jens 2012)

Timing	**Event**
Days 21-22	Single heart tube forms, pericardial cavity forms
Days 25- 28	Atrioventricular canal forms, common atrium forms, septum primal appears
Days 28	Heart begins to beat, ventricular septum appears as a small ridge in common ventricle, ventricles begin to dilate
Days 28-35	Four-chambered heart forms
Days 35-42	Coronary arteries form, inferior vena cave forms
Days 43- 49	Formation of muscular interventricular septum, superior vena cave forms, coronary sinus forms

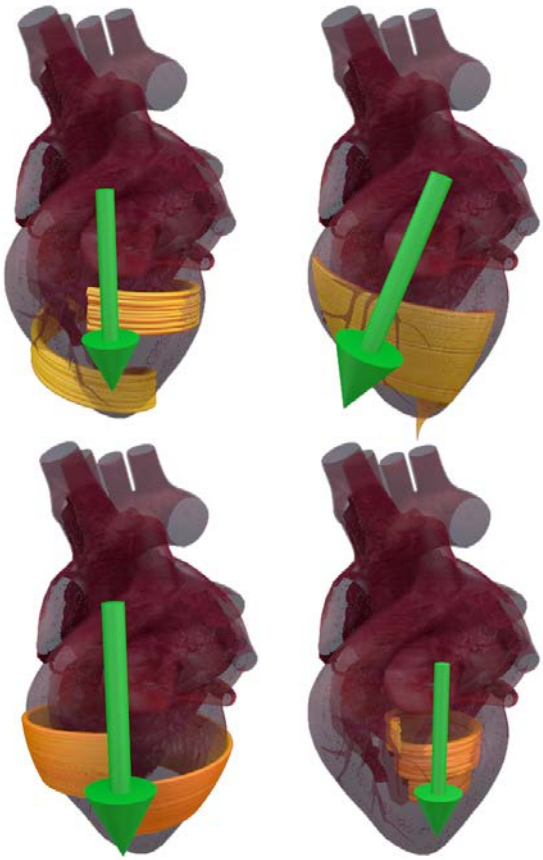

Figure 2.1 Orientation of cardiac muscle of four different myocardium groups. The green arrow indicates direction of cardiac vector.

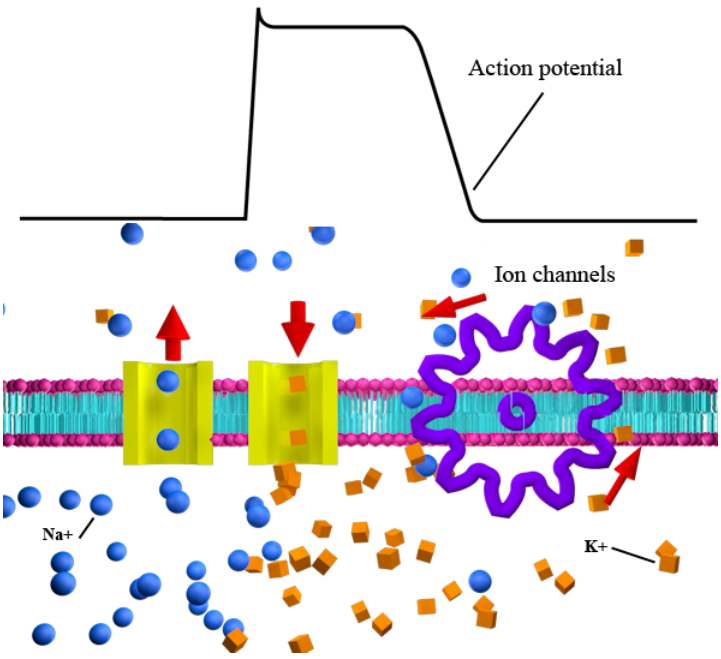

Figure 2.2 Illustration of action potential and ion channels.

2.2. Physiological basis of fetal magnetocardiography: ion channels

The magnetic field picked up by SQUID coil as well as the electric field measured at the mother's abdominal surface is generated by the fetal cardiac muscle. Due to ion concentration difference, electrical potentials exist across the membranes of cardiac muscle cells. The electric activation of myocytes has the same mechanism as in the nerve cell. In normal cardiac fibers, the powerful sodium-potassium pump actively transports sodium and potassium ions through the membrane. Thus, the potassium concentration is great inside the membrane but very low outside the membrane and vice versa for the sodium concentration. In the rest state, the membrane is highly permeable to potassium but only slightly permeable to sodium, it is logical that the diffusion of potassium contributes far more to the membrane potential than does the diffusion of sodium. As the diffusion of potassium ions, they carry positive electrical charges to the outside, thus creating electropositivity outside and electronegativity inside. When the diffusion potential is great enough (-90mV), further potassium diffusion is blocked despite the high concentration gradient.

During the activation state, the sodium channels instantaneously become activated and allow up to a 5000-fold increase in sodium conductance. The normal state of -90 mV is immediately neutralized by the inflowing positively charged sodium ions. The potential difference rises to +30 mV. At the same time, the slow calcium-sodium channels are activated and remain open for several tenths of a second. As a result, a large quantity of both calcium and sodium ions flows through these channels to the interior of the cardiac fibers, and this maintains a prolonged period of depolarization,

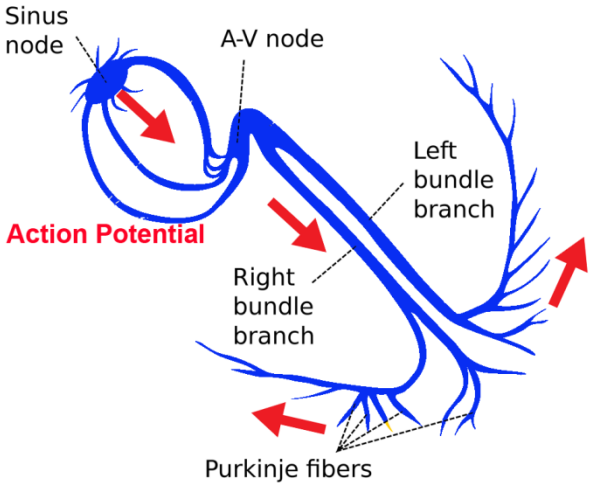

Figure 2.3 Conduction system of heart

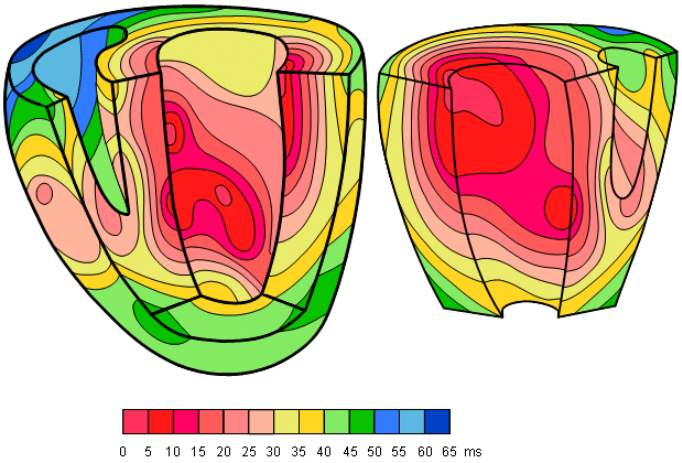

Figure 2.4 Isochronic surfaces of the ventricular activation. (Durrer *et al.* 1970)

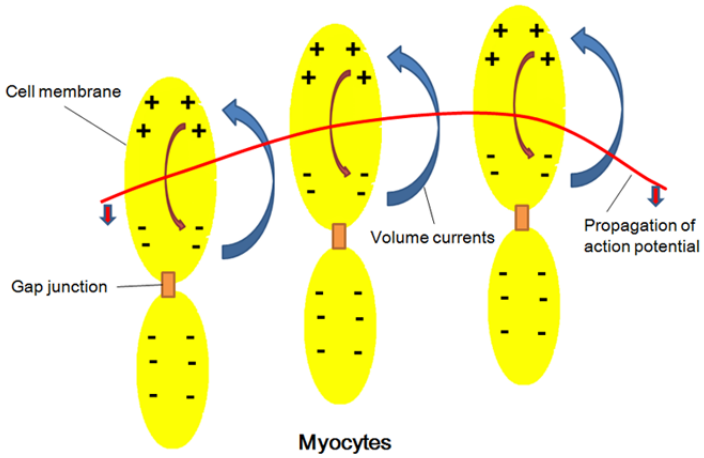

Figure 2.5 Generation of volume currents inside myocytes, red curve indicates the wavefront of action potential.

causing the plateau in the action potential (figure 2.2).

The amplitude of the action potential for cardiac muscle is around 100 mV. The duration of the cardiac muscle impulse is two orders of magnitude longer than that in either nerve cell or skeletal muscle. A plateau phase follows cardiac depolarization, and repolarization takes place after that. As in the nerve cell, repolarization is a consequence of the outflow of potassium ions. The duration of the action impulse is about 300 ms, as shown in figure 2.2. After the period, the membrane becomes highly permeable to sodium ions, the sodium channels and calcium-sodium channel begin to close and potassium channels open. The rapid diffusion of potassium ions to the exterior re-establishes the normal negative resting membrane potential. Associated with the electric activation of cardiac muscle cell is its mechanical contraction, which occurs a little later. In cardiac muscle cells, the action potential propagates in both directions. As a result, the activation wavefronts have complex shape.

The propagation of action potential starts from sinus node (SA) which consists of specialized self-excitatory muscle cells. From the sinus node, activation propagates throughout the atria to the atrioventricular node (AV node) located at the boundary between the atria and ventricles. Propagation from the AV node to the ventricles is provided by the bundle of His. The bundle of His separates into two bundle branches propagating along each side of the septum where they ramify into Purkinje fibers that diverge to the inner sides of the ventricular walls (as shown in figure 2.3).

The propagation of action potential inside ventricle is cell-to-cell based activation. From the inner side of the ventricular wall, the many activation sites cause the

formation of a wavefront which propagates through the ventricular mass toward the outer wall. After each ventricular muscle region has depolarized, repolarization occurs. Repolarization is not a propagating phenomenon, and because the duration of the action impulse is much shorter at the outer side of the cardiac muscle than at the inner side, the termination of activity appears as if it were propagating from ventricle inner side toward the outer side (figure 2.4).

The activation of heart cells generates small volume currents (figure 2.5). These volume currents propagate through various tissues up to the outer surface of the maternal abdomen. The potential difference can be picked up by fetal ECG sensors to reflect fetal heart activity. The volume currents as well as the currents flowing within the cardiac muscle cells give also rise to a magnetic field that can be detected by SQUID sensors. The conductivities of different tissues surrounding fetal heart have an influence on the electrical field as well as magnetic field (Czapski *et al.* 1996). However, the interpretation of fetal MCG signals requires less detailed knowledge of the tissues around the fetal heart, which makes it possible to obtain more precise information as early as 20 weeks of gestation.

Although measuring fetal heart magnetic field is more reliable compared to electric currents, this magnetic field is still very weak (less than a millionth of the magnetic field of the earth) and therefore requires extremely sensitive sensors and magnetic shielded room for precise measurements, which will be described in chapter 3 and chapter 4.

CHAPTER 3 THE FORWARD ELECTROMAGNETIC PROBLEM IN FETAL MAGNETOCARDIOGRAPHY: SOURCE AND VOLUME CONDUCTOR MODELING

Neural current sources of fetal heart produce external magnetic fields and surface potentials that can be measured using magnetocardiography (MCG) and electrocardiography (ECG). The electrical currents confined to the maternal abdomen consist of two components, the primary currents and the passive currents. The primary currents refer to the impressed microscopic passive cellular currents, and the passive currents are a result of the associated macroscopic electric field. The currents generated by the fetal heart travel through all the tissue layers to the surface of maternal abdomen and can be picked up the electric sensors used in fECG. Thus the electric field as well as the magnetic field are influenced by the geometry and electrical conductivity of tissue layers (volume conductor) surrounding the fetal heart. In adult measurements, the ECG is measured at fixed positions to ensure that the influence of volume conductor is similar for each subject. However, in fetal ECG and MCG volume conductors vary from subject-to-subject or for the same subject when measurements are performed at different gestational ages. Therefore, to allow for a reliable diagnosis by means of fetal MCG or fetal ECG, the influence on the measured signal of the tissues surrounding the fetal heart should be estimated.

3.1. Volume conductor modeling in fMCG

The volume conductor refers to the three-dimensional layers of conduction medium, including fetus, amniotic sac and maternal abdomen. In MCG and ECG, the currents from the fetal heart travel through tissues to the abdominal skin. The conductance of the tissues hence influences the recorded signals. Unlike adult ECG and MCG, the signal of fetal ECG and MCG are influenced by two significant problems: 1) the large variability in the position and orientation of the fetuses relative to the sensing system, which modulate the signals recorded at different locations over the maternal abdomen, and 2) the unknown effect of the variable geometry of the tissue and fluid layers surrounding the fetal heart on the measured signals. These factors introduce confounding effects on the amplitude and general morphology of the signals recorded over the maternal abdomen, so that it is often difficult to explain the inter-subject variations in signal distribution across the sensor array as being generated by differences in cardiac electrophysiology, common inconsistencies in the fetal presentation or variable anatomy of the fetal-maternal unit.

A mathematical model is constructed to estimate the effects of volume conduction. The magnetic field distribution near the maternal abdomen and potential distribution at the surface of maternal abdominal skin are calculated. For this purpose, the maternal-fetal unit is divided into discrete volumes and each of these volumes is assigned an effective conductivity and dielectric permittivity (as shown in figure 3.1) based on observations reported by other studies.

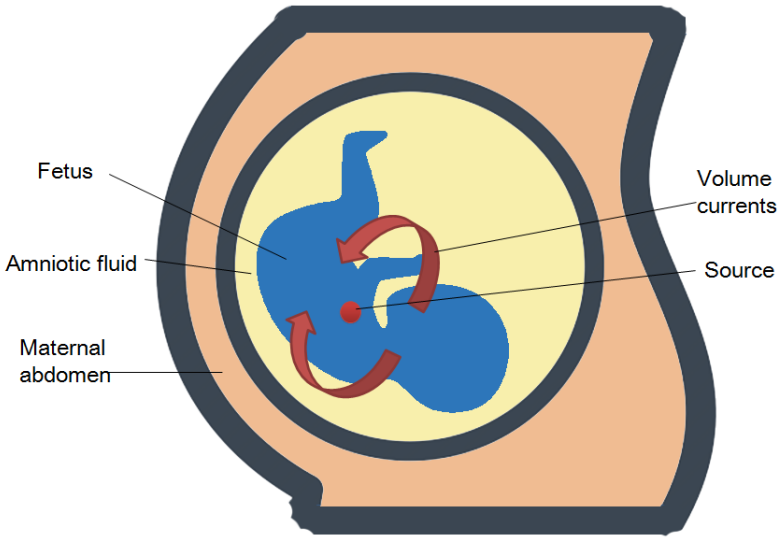

Figure 3.1 Illustration of fetal volume conductor subdivided into three homogeneous compartments, the fetus, the amniotic fluid and the maternal abdomen. Red arrows are volume currents generated from fetal heart.

For the biological signals of interest in fMCG, the time-derivatives of the associated electric and magnetic fields are sufficiently small to be ignored in Maxwell's equation (Hamalainen *et al.* 1993, Mosher *et al.* 1999). The following static magnetic field equations are considered when describing the properties of the compartments:

$$\nabla \times \mathbf{B}(\mathbf{r}) = \mu_0 \mathbf{J}(\mathbf{r})$$

$$\nabla \bullet \mathbf{B}(\mathbf{r}) = 0 \qquad (3.1)$$

which means the curl of the magnetic field at location r is proportional to the current density, and the divergence of the magnetic field is zero. Our problem is to study the current density $\mathbf{J}(\mathbf{r})$ in a closed volume of finite conductivities. Outside the volume the conductivity and current density are zero. Equation 3.1 can be rewritten into the Biot-Savart law,

$$\mathbf{B}(\mathbf{r}) = \frac{\mu_0}{4\pi}\int_G \mathbf{J}(\mathbf{r}') \times \mathbf{d} / d^3 d\mathbf{r}' \tag{3.2}$$

where $\mathbf{d}$ is the distance between the observation point $\mathbf{r}$ and the source point $\mathbf{r}'$, the integration is carried out over a closed volume G.

The currents can be decomposed into two components, passive and primary. The passive currents are a result of the macroscopic electric field in the conducting medium of the volume, $\mathbf{J}_v(\mathbf{r}) = \sigma(\mathbf{r})\mathbf{E}(\mathbf{r})$. All other currents are considered primary currents, $\mathbf{J}_p(\mathbf{r}) = J(\mathbf{r}) - J_v(\mathbf{r})$. The problem is to locate these primary currents and evaluate their properties, since they are the sources of fetal heart activity. Substituting interpretation of $\mathbf{J}(\mathbf{r})$ into the equation (3.2) for the quasi-static magnetic field yields

$$\mathbf{B}(\mathbf{r}) = \frac{\mu_0}{4\pi}\int_G (\mathbf{J}_p(\mathbf{r}') - \sigma(\mathbf{r}')\nabla\mathbf{V}(\mathbf{r}')) \times \mathbf{d} / d^3 d\mathbf{r}' . \tag{3.3}$$

In fMCG, typical volume conductor models assume that the fetal-maternal unit may be represented by three to four regions, e.g., fetus, amniotic fluid, maternal abdominal skin. The vernix caseosa compartment is only included in late gestational age. In the general formulation of the model, we assume the volume can be divided into M+ 1 different region with conductivities σ_i, i = 1, ..., M+1. These regions are separated from adjacent regions by a total of $m \geq M$ surfaces S_i. We can rewrite the volume integral in (3.3) as a sum of surface integrals,

$$\mathbf{B}(\mathbf{r}) = \mathbf{B}_\infty(\mathbf{r}) - \frac{\mu_0}{4\pi}\sum_{i=1}^{m}(\sigma_i^- - \sigma_i^+)\left(\int_{S_i} v(\mathbf{r}')\mathbf{n}_i(\mathbf{r}') \times \mathbf{d} / d^3\right) da' \tag{3.4}$$

$$\mathbf{B}_\infty(\mathbf{r}) = \frac{\mu_0}{4\pi}\int_G \mathbf{J}_p(\mathbf{r}') \times \mathbf{d} / d^3 d\mathbf{r}' \tag{3.5}$$

where $\mathbf{n}_i(\mathbf{r}')$ is the outward directed unit vector normal to the i^{th} surface, $\mathbf{B}_\infty(\mathbf{r})$ is the primary field due to the primary current only, and $v(\mathbf{r}')$ is the current potential at location $\mathbf{r}'$.

To compute the magnetic field in (3.4) we must know the potential $v(\mathbf{r})$ on all boundaries. Using Green's theorem, we can obtain a surface integral equation for $v(\mathbf{r})$ (Sarvas 1987a):

$$v_\infty(\mathbf{r}) = \frac{(\sigma_i^- + \sigma_i^+)}{2} v(\mathbf{r}) + \frac{1}{4\pi} \sum_{i=1}^{m} (\sigma_i^- - \sigma_i^+) \int_{S_i} v(\mathbf{r}') \mathbf{n}_i(\mathbf{r}') \bullet \mathbf{d} / d^3 da', \quad \mathbf{r} \in S_j \tag{3.6}$$

where $v_\infty(\mathbf{r})$ is the primary potential. Assuming the conduction medium to be infinite homogeneous, equation (3.6) can be simplified into

$$v_\infty(\mathbf{r}) = \frac{1}{4\pi} \int_G \mathbf{J}_p(\mathbf{r}') \times \mathbf{d} / d^3 d\mathbf{r}' \tag{3.7}$$

Thus the magnetic field and the electric field can be calculated from equation (3.4) and (3.6). In a simplified spherical volume conductor model, since we are interested in the radial component $B_r(\mathbf{r})$ of the field at sensor location $\mathbf{r}$, the contribution from passive volume currents vanishes. Equation (3.4) is therefore simplified to $B_r(\mathbf{r}) = \mathbf{B}_\infty(\mathbf{r}) \bullet \mathbf{r} / r$. Hence the Biot-Savart equation can be solved with analytical solutions in spherical volume conductors.

3.2. Modeling the fetal heart volumetric source

After setting up the maternal-fetal volume conductor, we need to build a model of the cardiac current sources in order to compute the forward magnetic field. A cardiac vector source refer to one or a group of fetal heart current vectors that produce

external magnetic fields and surface potentials that can be measured using magnetocardiography (MCG) and electrocardiography (ECG). The fields in the maternal abdomen consist of two components, the primary current and the passive volume current. The primary current refers to the impressed microscopic passive cellular currents, and the passive currents are a result of the macroscopic electric field. The primary currents are considered to be the sources of interest in fetal MCG, since they represent the areas of myocytes activity of the fetus.

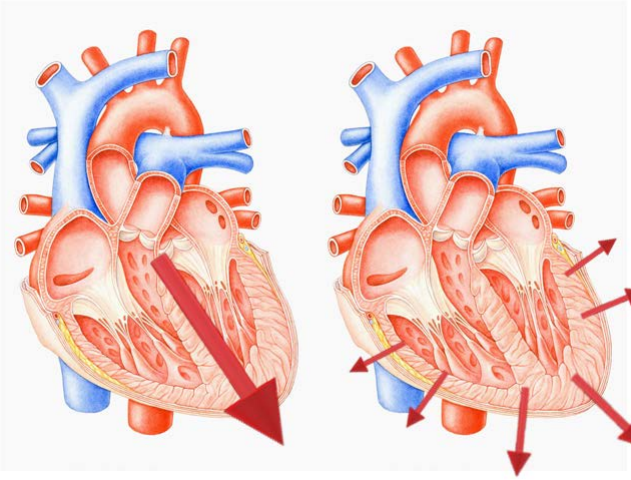

Figure 3.2 Single dipole model (left) is based on a single dipole with fixed location, variation and magnitude. Multiple dipole model (right) includes several dipoles, each representing a certain anatomical region of the heart. These dipoles are fixed in location and have varying magnitude and varying orientation.

There are several basic volume source models for modeling fetal heart source as shown in figure 3.2. The single dipole model of the heart represents cardiac electrical activity as a single, time-varying vector. The origin of this vector is the center of the heart and the end of the vector sweeps through the trunk in a quasi-periodic path. In

infinite homogenous volume conductor model, the source of the volume conductor model is expressed as the divergence of the source currents, as

$$v(\mathbf{r}) = -\frac{1}{4\pi\sigma}\iiint \frac{\nabla \bullet \mathbf{J}_s(\mathbf{r}')}{\|\mathbf{r}-\mathbf{r}'\|} d\mathbf{V}' \tag{3.8}$$

and the magnetic field is

$$\mathbf{B}(\mathbf{r}) = \nabla \frac{\mu_0}{4\pi}\iiint_V \frac{\nabla \bullet \mathbf{J}_s(\mathbf{r}')}{\|\mathbf{r}-\mathbf{r}'\|} d\mathbf{V}' \tag{3.9}$$

When using a compartment volume conductor model, the boundary element method can be used to transform the fields to meet the boundary conditions at the interfaces between the compartments. To reduction the computation complexity, the source term on the left is decomposed using Legendre polynomials, resulting,

$$v(\mathbf{r}) = -\mathrm{Re}[\frac{1}{4\pi\sigma}\sum_{n=0}^{\infty}\sum_{n=0}^{n}\left[\frac{Y_{nm}(\theta,\phi)}{r^{n+1}}\right]\iiint (\mathbf{r}')^n \bar{Y}_{nm}(\theta',\phi')\nabla \bullet \mathbf{J}_s(\mathbf{r}')d\mathbf{V}'] \tag{3.10}$$

$$B(\mathbf{r}) = -\mathrm{Re}[\frac{\mu_0}{4\pi}\sum_{n=0}^{\infty}\sum_{n=0}^{n}\nabla\left[\frac{Y_{nm}(\theta,\phi)}{r^{n+1}}\right]\times\iiint (\mathbf{r}')^n \bar{Y}_{nm}(\theta',\phi')\nabla \bullet \mathbf{J}_s(\mathbf{r}')d\mathbf{V}'] \tag{3.11}$$

Omitting the high order terms in equation 3.10 and 3.11 we have

$$\varpi(\mathbf{r}) = -\frac{\mathbf{r}\bullet\mathbf{q}}{4\pi\sigma\mathbf{r}^3} \quad \text{where} \quad \mathbf{q} = \iiint \mathbf{J}_s(\mathbf{r}')d\mathbf{V}' \tag{3.12}$$

And

$$\mathbf{B}(\mathbf{r}) = \frac{\mu_0\mathbf{q}\times\mathbf{r}}{4\pi\mathbf{r}^3} \tag{3.13}$$

where **q** is the current dipole moment. The single dipole model is placed in heart center to minimize the contribution of higher-order moments. The Legendre polynomials approach reduces the computational complexity by neglecting the high

order moments in the expansion, which only is correct under the assumption that the fetal heart is distant from detector and single current dipole model.

In spherical volume conductors, the normal vector of the surface is $\mathbf{n}(\mathbf{r}') = \mathbf{r}'/|\mathbf{r}'|$ for all $\mathbf{r}'$ on all surfaces. Thus, we could examine only the radial component of the field on all surfaces at location $\mathbf{r}, B_r = \mathbf{B}(r)\bullet\mathbf{r}/|\mathbf{r}|$, then the contribution due to the passive volume currents vanish. We obtain the primary current model from equation (3.13)

$$\mathbf{B}(\mathbf{r}) = \frac{\mu_0 \mathbf{q}\times\mathbf{r}(\mathbf{r}-\mathbf{r}_q)\bullet\mathbf{r}}{4\pi|\mathbf{r}-\mathbf{r}_q|^3|\mathbf{r}|} = \frac{\mu_0 \mathbf{r}_q\times\mathbf{q}\bullet\mathbf{r}}{4\pi|\mathbf{r}-\mathbf{r}_q|^3|\mathbf{r}|} \qquad (3.14)$$

Since no currents exist out the maternal-fetal unit, the radial magnetic field B_r can be used to derive the scalar magnetic potential $U(r)$, as $\mathbf{B}(\mathbf{r}) = -\mu_0\nabla U(r)$, and (3.14) can be written into

$$\mathbf{B}(\mathbf{r}) = \frac{\mu_0}{4\pi\mathbf{F}^2}(\mathbf{F}\mathbf{q}\times\mathbf{r}_q - (\mathbf{q}\times\mathbf{r}_q\bullet\mathbf{r})\nabla\mathbf{F}) \qquad (3.15)$$

$$\mathbf{F} = \mathbf{F}(\mathbf{r},\mathbf{r}_q) = a(ra + r^2 - (\mathbf{r}_q\bullet\mathbf{r})) \qquad (3.16)$$

$$\nabla\mathbf{F} = \nabla\mathbf{F}(\mathbf{r},\mathbf{r}_q) = (r^{-1}a^2 + a^{-1}(\mathbf{a}\bullet\mathbf{r}) + 2a + 2r)\mathbf{r} - (a + 2r + a^{-1}(\mathbf{a}\bullet\mathbf{r}))\mathbf{r}_q \qquad (3.17)$$

where $\mathbf{F}$ is the scalar function, $\nabla\mathbf{F}$ is a vector function, and both are functions of $\mathbf{r}$ and $\mathbf{r}_q$, $\mathbf{a} = \mathbf{r} - \mathbf{r}_q$, $a = |\mathbf{a}|$, and $r = |\mathbf{r}|$

Beginning from the single dipole model, we can expand the method to the multiple-dipole situation. We can rewrite equation 3.13 as

$$\mathbf{B}(i) = \frac{\mu_0\mathbf{Q}\times\mathbf{r}(i)}{4\pi\mathbf{r}(i)^3} \quad \text{where} \quad \mathbf{r}(i) = \mathbf{R}(i) - \mathbf{L} \qquad (3.18)$$

where $\mathbf{L}$ is the dipole location, $\mathbf{R}(\mathrm{i})$ is the i^{th} measurement sensor location, and $\mathbf{B}_{\mathrm{source}}(\mathrm{i})$ is the magnetic field at $\mathbf{R}(\mathrm{i})$. Our study uses the SQUID biomagnetometer to acquire the magnetic field at position $\mathbf{R}(\mathrm{i})$, which is only one component of the three-dimensional field. Thus, only a scalar measurement is made:

$$\mathrm{B}(\mathrm{i}) = \mathbf{B}(\mathrm{i})\bullet\mathbf{s}(\mathrm{i}) \tag{3.19}$$

where $\mathbf{s}(\mathrm{i})$ is the unit orientation of the i^{th} sensor. Combining equation (3.13) and (3.19) yields

$$\mathrm{B}(\mathrm{i}) = \frac{\mu_0\left(\mathbf{R}(\mathrm{i})-\mathbf{L}\right)\times\mathbf{s}(\mathrm{i})\bullet\mathbf{Q}}{4\pi\left|\mathbf{R}(\mathrm{i})-\mathbf{L}\right|^3} = \mathbf{g}(\mathrm{i})\bullet\mathbf{Q} \tag{3.20}$$

The vector $\mathbf{g}(\mathrm{i})$ can be viewed as a gain vector, relating the moment intensity of the dipole to the measurement at position $\mathbf{R}(\mathrm{i})$. The gain vector can be represented as $\mathbf{1}\times\mathbf{3}$ row vector and the moment as a $\mathbf{3}\times\mathbf{1}$ column vector, then the equation (3.20) can be arranged to the matrix form:

$$\mathbf{B} = \begin{bmatrix} \mathrm{B}(1) \\ \vdots \\ \mathrm{B}(\mathrm{m}) \end{bmatrix} = \frac{\mu_0}{4\pi}\begin{bmatrix} \dfrac{\left(\mathbf{R}(1)-\mathbf{L}\right)\times\mathbf{s}(1)}{\left|\mathbf{R}(1)-\mathbf{L}\right|^3} \\ \vdots \\ \dfrac{\left(\mathbf{R}(\mathrm{m})-\mathbf{L}\right)\times\mathbf{s}(\mathrm{m})}{\left|\mathbf{R}(\mathrm{m})-\mathbf{L}\right|^3} \end{bmatrix}\bullet[\mathbf{Q}] = \begin{bmatrix} \mathbf{g}(1) \\ \vdots \\ \mathbf{g}(\mathrm{m}) \end{bmatrix} = \mathrm{G}(\mathbf{L})\mathbf{Q} \tag{3.21}$$

The matrix $\mathrm{G}(\mathbf{L})$ can be considered to be the gain or relationship between a unit moment source at $\mathbf{L}$ and the column vector measurements at locations $\{\mathbf{R}(\mathrm{i})\}$. Each column in G is viewed as the model for three elementary dipoles at the same location, but along different orientations. Referring the collocated elementary dipoles as components of a single dipole, with moment $\mathbf{Q}$, this model extends to the multiple dipoles case, for p dipoles

$$\mathbf{B} = [G_1 \cdots G_p] \begin{bmatrix} \mathbf{Q}_1 \\ \vdots \\ \mathbf{Q}_p \end{bmatrix} \tag{3.22}$$

For m sensors and p dipoles, vector $\mathbf{B}$ is $m \times 1$, matrix G is $m \times 3p$, and $\begin{bmatrix} \mathbf{Q}_1 \\ \vdots \\ \mathbf{Q}_p \end{bmatrix}$ is $3p \times 1$.

3.3. Boundary element method

As stated previously, one problem with spherical volume conductors is that it results in large inaccuracies of fetal cardiac source reconstruction. The fetal MCG volume conductors are clearly not spherical. To improve estimation accuracy, we can derive realistic volume conductor models from ultrasound anatomical images (as shown in figure 3.3). The realistic volume conductor model assumes a set of contiguous isotropic regions, each with constant electrical conductivity. In realistic models, the integral in equation (3.9) must be solved using numerical solutions. For this purpose, we use *Boundary element method* (BEM) for solving realistic volume conductor model problems (Ferguson *et al.* 1994, Kybic *et al.* 2005, Mosher *et al.* 1995, Schlitt *et al.* 1995).

To briefly summarize the BEM approach, which is used to compute the surface integral of the voltages $v(\mathbf{r})$, we first tessellate each surface S_i into suitable d_i triangles, $\Delta_k^i, k = 1, ..., d_i$. The area of each triangle is denoted μ_k^i. If we assume that the voltage is constant across each triangle, and then integrate (3.6) over one triangle, we can develop a set of linear equations (Mosher *et al.* 1995),

$$\mathbf{V}^{i} = \sum_{j=1}^{d_i} \mathbf{H}^{ij}\mathbf{V}^{j} + \mathbf{g}^{i} \quad i = 1, \cdots, m \tag{3.23}$$

where vector $\mathbf{g}$ is lineally related to the primary voltage $\mathbf{V}_0$ and matrix $\mathbf{H}$ is only computed once the conductor geometry is decided. We then deflate $\mathbf{H}$ to $\tilde{\mathbf{H}}$ to uniquely solve the system of N equations,

$$\left(\mathbf{I} - \tilde{\mathbf{H}}\right)\mathbf{V} = \mathbf{g} \tag{3.24}$$

where $\mathbf{I}$ is an $\mathbf{N} \times \mathbf{N}$ identity matrix.

After solving for $\mathbf{V}$, we have essentially solved the ECG forward problem for all surface elements in the maternal abdomen volume.

The magnetic field is found from a discrete form of (3.4), where we can approximate the integration using the cancroids of the triangles, yielding

$$\mathbf{B}(\mathbf{r}) = \mathbf{B}_0(\mathbf{r}) + \mathbf{A}(\mathbf{I} - \tilde{\mathbf{H}})^{-1}\mathbf{g} \tag{3.25}$$

where matrix **A** represents the linear transfer function that relates V to the contribution that the passive currents add to the magnetic field at point **r**. The matrix **A** is a function of the sensor location and the volume conductor geometry and can be computed without the knowledge of source currents.

Equation (3.25) represents a linear relationship between the cardiac dipole moment **q** and magnetic field **B** as well as potential measurement V. Therefore we can represent each model as $\mathbf{B} = \mathbf{K}(\mathbf{r}, \mathbf{r}_q)\mathbf{q}$ or $V = \mathbf{K}(\mathbf{r}, \mathbf{r}_q)\mathbf{q}$, where **K** is a matrix kernel. To use the matrix kernel, we first convert the cross-product operator to the product of a matrix and a vector as below,

$$\mathbf{a}\times\mathbf{b} = \mathbf{C}_a\mathbf{b} = \begin{bmatrix} 0 & -a_z & a_y \\ a_z & 0 & -a_x \\ -a_y & a_x & 0 \end{bmatrix}\begin{bmatrix} b_x \\ b_y \\ b_z \end{bmatrix} \quad (3.26)$$

Substitute (3.26) into (3.15) and , we have

$$\begin{aligned} \mathbf{B}_s(\mathbf{r}) &= \frac{\mu_0}{4\pi F^2}((-F)\mathbf{C}_{\mathbf{r}_q}\mathbf{r}_q + (\nabla F)(\mathbf{r}^T\mathbf{C}_{\mathbf{r}_q}\bullet\mathbf{q})) \\ &= \left[\frac{\mu_0}{4\pi}\frac{\left[\nabla F\mathbf{r}^T - F\mathbf{I}\right]}{F^2}\mathbf{C}_{\mathbf{r}_q}\right]\mathbf{q} = \mathbf{K}_s(\mathbf{r},\mathbf{r}_q)\mathbf{q} \end{aligned} \quad (3.27)$$

where **I** is the identity matrix. Therefore the boundary element method is expressed as

$$\mathbf{B}_{bem}(\mathbf{r}) = \left[\mathbf{K}(\mathbf{r},\mathbf{r}_q) + \mathbf{A}\mathbf{K}_{v(bem)}(\mathbf{r},\mathbf{r}_q)\right]\mathbf{q} = \mathbf{K}_{b(bem)}(\mathbf{r},\mathbf{r}_q)\mathbf{q} \quad (3.28)$$

$$v_{bem} = \left[(\mathbf{I}-\bar{\mathbf{H}})^{-1}\mathbf{G}_v\right]\mathbf{q} = \mathbf{K}_{v(bem)}(\mathbf{r},\mathbf{r}_q)\mathbf{q} \quad (3.29)$$

In each case, the bracket term is represented by the 3×3 kernel matrix $\mathbf{K}(\mathbf{r},\mathbf{r}_q)$, which is a function of the observation point and the dipole point only.

3.4. Boundary element method (BEM): feasibility studies

The BEM algorithms used throughout this study and the specific implementation strategies are described in (Ferguson *et al.* 1994, Hamalainen *et al.* 1993, Mosher and Leahy 1999). The numerical algorithms were tested for accuracy in two feasibility studies. First (feasibility experiment 1) we aimed to characterize the numerical errors bounds of the BEM forward solutions. Since for a radial source in a spherically symmetric conductor the primary and volume currents counterbalance each other's contribution to the magnetic field, geometries approaching a sphere in combination with radial sources can introduce larger numerical errors. We defined a 4-layer spherically symmetric volume conductor, with radii of 6, 6.2, 8 and 15 cm, and

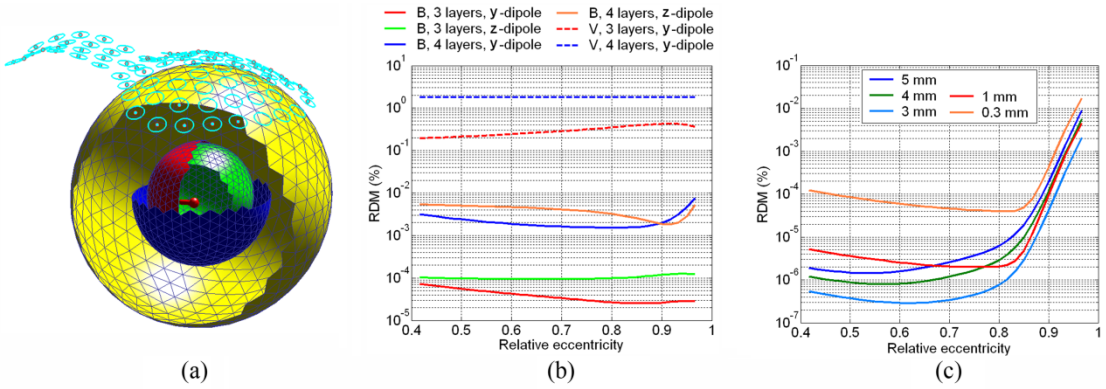

Figure 3.3. (a) Setup of the simulations in feasibility experiment 1. (b) RDMs for different orientations of a dipole with strength of 300 nAm, and for the 3- and 4-shells models. Due to spherical symmetry, RDMs for the electric potential are shown only for dipoles orientated along the y-axis. Results are shown for the linear-collocation approach. (c) Results from feasibility experiment 2. RDMs are shown for a four-shells volume conductor, with the center of the third sphere shifted with 3 cm on both y and z axes with respect to the center of the outermost sphere, and the center of the first and second spheres shifted with 1 cm on the x axis relative to the center of the third sphere. RDMs are computed relative to the solution obtained with 2mm thickness.

conductivities of 0.22, 2×10-6, 1.4, and 0.05 S/m (Oostendorp et al. 1989a, Stinstra et al. 2002a) to replicate the approximate size and conductivity of the fetal body, vernix, amniotic fluid and surrounding tissues, respectively. Each of the spherical surfaces was triangulated using 642 triangles per surface. In a second approach, the thin resistive layer was excluded leading to a 3-layer model of the volume conductor. For each case, the analytical solution of the electric potential on the external surface, computed using the Legendre polynomials method (Zhang 1995) with 24 terms in the truncated expansion, and the analytical solution of the magnetic field (Sarvas 1987b) for axial gradiometer sensors were compared with the BEM

forward solutions for dipoles oriented along the y and z axes, respectively. The dipole position was varied on the x axis. The BEM solutions were computed for both linear-collocation and linear-Galerkin implementations (Mosher and Leahy 1999). For the 4-layer model, the BEM solutions were computed with the Isolated Problem Approach (IPA) (Hämäläinen and Sarvas 1989). Relative Difference Measures (RDM) between the analytical and numerical solutions (figure 3.3b) indicated adequate accuracy for the BEM linear-collocation approach. The linear-Galerkin approach provided slightly smaller RDMs over a range of source eccentricities, but the computational time was significantly increased. Since the linear-collocation provided accurate solutions and efficient computational times, it was considered optimal for the current studies. In a second series of simulations (experiment 2) we assessed the errors that can be introduced by variations in the thickness of the vernix. Volume conductors that were not spherically symmetric were obtained by positioning the inner compartments in figure 3.3a (representing the AS and fetus covered by a thin resistive layer) at different locations inside the outermost spherical compartment.

The thickness of the resistive layer was varied at 0.3, 1, 2, 3, 4 and 5 mm. We used the BEM solution (linear-collocation approach with IPA) obtained for 2 mm thickness as a reference, and we computed the RDMs between this reference and the solutions obtained for other thickness values. The results (figure 3.3c) show that thickness variations of the resistive layer lead to very small differences in the magnetic field. Hence, throughout the simulations in this study, we therefore considered a uniform, 5 mm thick vernix layer. This choice is motivated by the fact that the inner and outer

surfaces of the thin layer should in principle be tessellated using triangles of a size comparable to the thickness of the layer, which increases considerably the computational burden for very thin layers.

CHAPTER 4 INSTRUMENTATION AND SIGNAL PROCESSING

The first part of the chapter discusses the instrumentation used for the fetal MCG recordings and modeling of realistic volume conductors in fMCG. In the second part, we review the ICA filtering techniques for maternal signal removing and the signal reconstruction method (recursive multiple signal classification) for solving the inverse problem.

4.1. Superconducting quantum interference devices (SQUIDs)

All the fMCG tests in this study were performed using an 83-channel fetal biomagnetometer available at Hoglund Brain Imaging Center, University of Kansas Med Center (CTF Systems Inc., subsidiary of VSM MedTech Ltd.), housed in a magnetically shielded room. The hardware components include the fMCG, EEG and patient monitoring subsystems (as shown in figure 4.1a). During the test, the subject is asked to lie in a supine position (figure 4.1b) underneath the cryostat filled with liquid helium. Measurements are taken inside the magnetic shielded room and recordings are transferred to the computer system located outside the shielded room. During recording, the sensing system is positioned over the maternal abdomen. The 81 sensory array ensures a full coverage of the maternal abdomen. The MCG channel electronics includes SQUID magnetic flux-voltage converters immersed in the liquid helium in the dewar, low noise amplifiers at the top of the dewar and cables to connect the amplifiers to the electronics rack outside the shielded room. The digital flux-locked loop electronics is an over-sampled digital sample stream whose binary

values are directly proportional to the magnetic field sensed by the SQUID pickup coils. The data is filtered and down-sampled before being transmitted to the DSP electronics.

Superconducting quantum interference devices (SQUIDs) are sensitive detectors capable of detecting the magnetic flux. The basic unit of a SQUID sensor, depicted schematically in figure 4.2, consists of a low inductance ring interrupted by two Josephson junctions (X) shunted with resistors (R).). These weak links limit the flow of the supercurrent and are characterized by the maximum critical current *i* that can be sustained without loss of superconductivity. The spatial distribution of the axial gradiometer sensors with a 5 cm baseline ensures a full coverage of the maternal abdomen, with the cryostat being placed above the upper abdominal surface.

The magnetic fields from the fetal heart are extremely weak (typically 50-500 fT) compared with ambient magnetic-field. The earth's geomagnetic field, for example, is 109 or 108 times of fetal heart signals. Thus magnetic shielded rooms (MSR) are used to reject outside interferences. MSR is very useful for shielding at low frequencies of external magnetic noise spectrum, which is usually the result of moving magnetic objects (cars, etc.), located at various distance from the biomagnetometer.

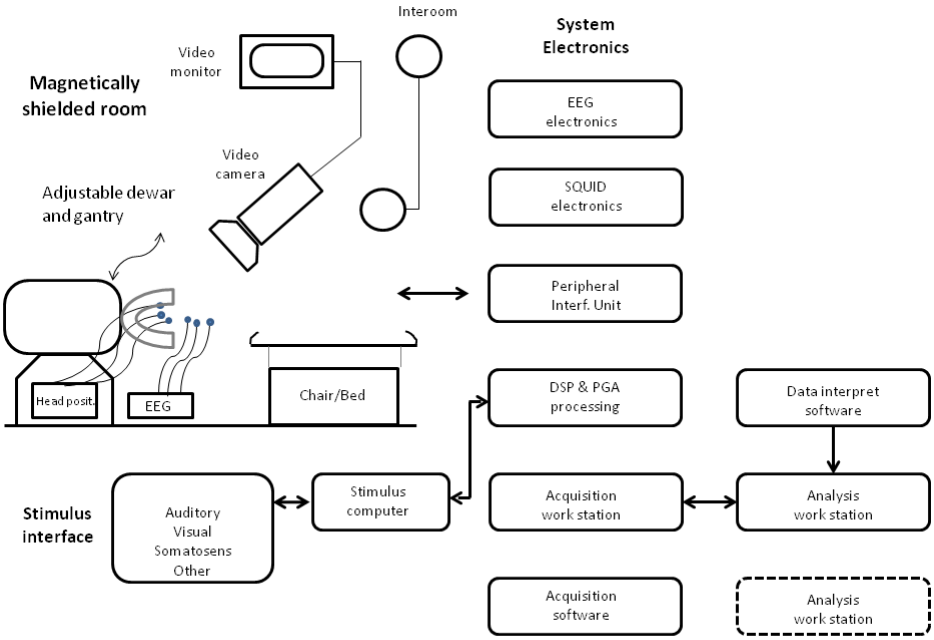

(a)

(b)

Figure 4.1 (a) Illustration of SQUID system (b) magnetic shielded room

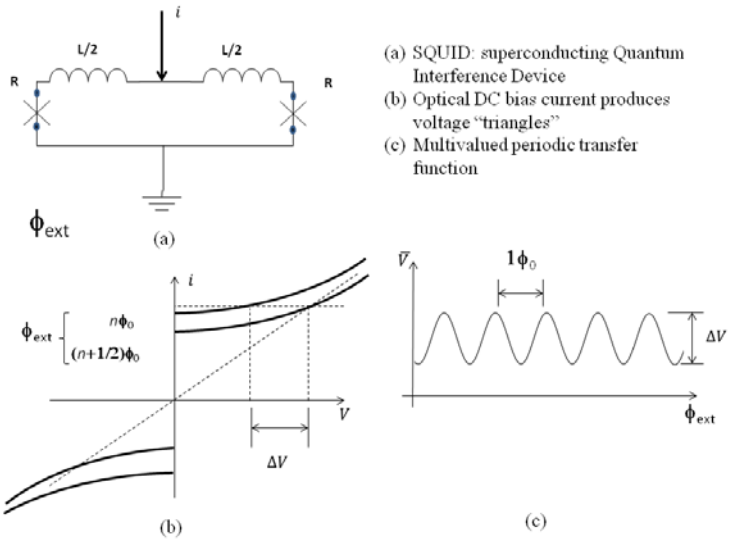

Figure 4.2 Properties of SQUID sensors

4.2. 3D ultrasound tracking system

To reconstruct a realistic volume conductor, we need first to obtain a 3D ultrasound image volume using the free hand techniques with a position sensor fixed at the ultrasound transducer. The free hand 3D ultrasound tracking system has been applied to various other applications in previous studies on fetal development. (Fenster *et al.* 2004) use this technique to quantify and visualize carotid disease. (Yagel *et al.* 2007) reviews and confirms the contribution of 3D ultrasound on monitoring fetal cardiovascular system development. For our study, we utilize this system to obtain the location of B-scan images to reconstruct a realistic volume conductor.

The freehand 3D ultrasound system is very powerful for tracing ultrasound probe movements in a fixed external coordinate system, as the situation in our study that the pregnant women were asked to lying in a spine position on the ultrasound chair. The

electromagnetic Trakstar sensor is placed on the ultrasound probe to measure the induced electrical current generated by the movement of the probe (Gee *et al.* 2003). The measured currents can be used to calculate the location of sensor in relative to three localization coils, which are place on the subject's abdomen.

One problem of the freehand 3D ultrasound system is that the system tracks and records the 3D location of the Trakstar sensor, rather than ultrasound scan plane, as shown in Figure 4.3. Therefore, the application requires finding the position and orientation of the scan plane relative to the coordinate system of the stationary localization coils, which were attached on the subject's abdomen. This transformation from sensor space to external world space is determined by probe calibration as in equation 4.1. The coordinates of localization coils defines the world coordinate system, and the position sensor is the mobile part (Berg *et al.* 1999).

$$T = \begin{pmatrix} \cos\alpha\cos\beta & \cos\alpha\sin\beta\sin\gamma - \sin\alpha\cos\gamma & \cos\alpha\sin\beta\cos\gamma + \sin\alpha\sin\gamma \\ \sin\alpha\cos\beta & \cos\alpha\sin\beta\sin\gamma + \cos\alpha\cos\gamma & \sin\alpha\sin\beta\cos\gamma - \cos\alpha\sin\gamma \\ -\sin\beta & \cos\beta\sin\lambda & \cos\beta\cos\gamma \end{pmatrix} p + \begin{pmatrix} t_x \\ t_y \\ t_z \end{pmatrix}$$

(4.1)

Where t_x, t_y and t_z are the translations, α, β and γ are the rotation about the x, y and z axis, p is the recorded coordinates of sensor, and T defines the transformation from sensor space to world space..

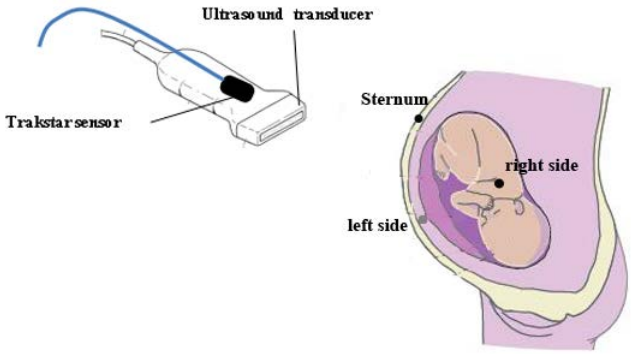

Figure 4.3 Illustration of Trakstar sensor and localization coils.

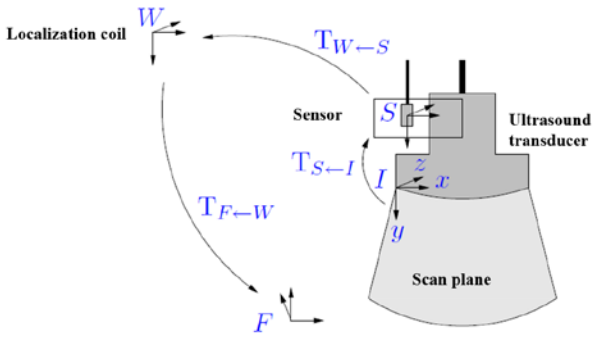

Figure 4.4: The coordinates associated with a freehand 3D ultrasound system. $T_{B\leftarrow A}$ defines a translation from the coordination system A to coordination B.

To perform probe calibration, we need to scan an object with known dimensions, such as cross-wires (Krupa 2006) or spherical object (Barratt *et al.* 2006) (figure 4.5). Once the ball object has been located in world space by the continuous B scan across the phantom, it can be mapped to the localization coils' coordinate system by the inverse of the position sensor readings. Once the probe calibration is completed, a transformation matrix can be calculated and stored to estimate the location of B scan images obtained from later ultrasound screenings. Co-registration of the ultrasound images with the fMCG sensor array is accomplished using three fiducial markers

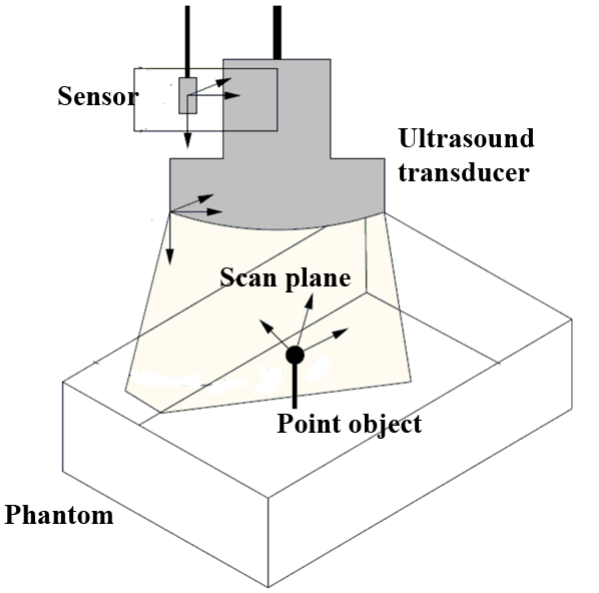

Figure 4.5 Geometry of the point phantom.

placed at non-collinear locations on the maternal abdomen (right side, left side, and sternum) (figure 4.3). Each marker's location is recorded by positioning the center of the ultrasound probe at that location and recording the corresponding frames. These frames are used to identify the markers locations on the volumetric image. The markers positions relative to the fMCG sensors are determined in the biomagnetometer by localizing three coils placed at those locations.

4.3. Data processing using Independent Component Analysis

fMCG recordings are complicated by the strong maternal MCG and contaminations from mother breathing and uterine contractions (figure 4.6). To separate the fetal heart signal from maternal signal and remove interferences such as maternal breathing, the fMCG signals are processed by ICA using an infomax-based ICA algorithm (Bell and Sejnowsky 1995) implemented in the EEGLAB software

(Delorme and Makeig 2004). ICA components of maternal cardiac activity, muscle activity and other artifacts are rejected; the de-noised fMCG signal is reconstructed from the remaining ICA components. fMCG actocardiography techniques developed in our laboratory (Popescu *et al.* 2007) are used to identify gross fetal body movements during the recordings based on the beat-to-beat variability of the QRS peak amplitude in single channel signals (Zhao and Wakai 2002) and in ICA components of fetal cardiac activity (figure. 4.7).

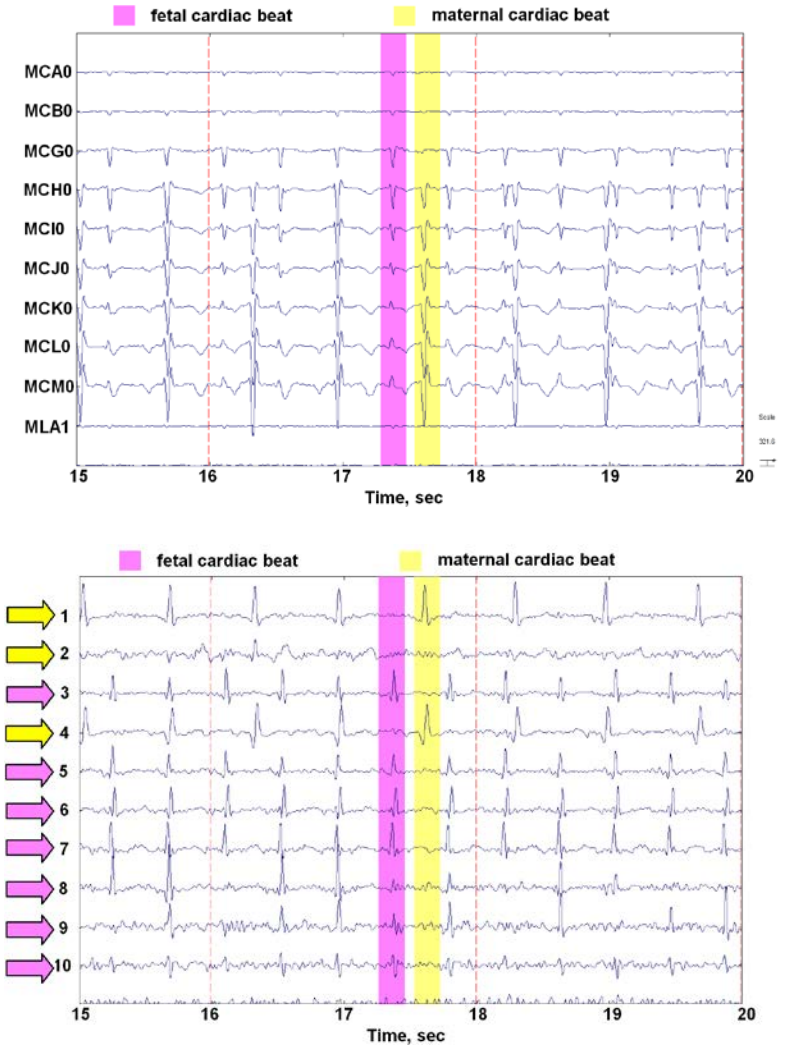

Figure 4.6 Channel data (top) and ICA (bottom) components of maternal and fetal cardiac beat before (top) and after (bottom) ICA filtering.

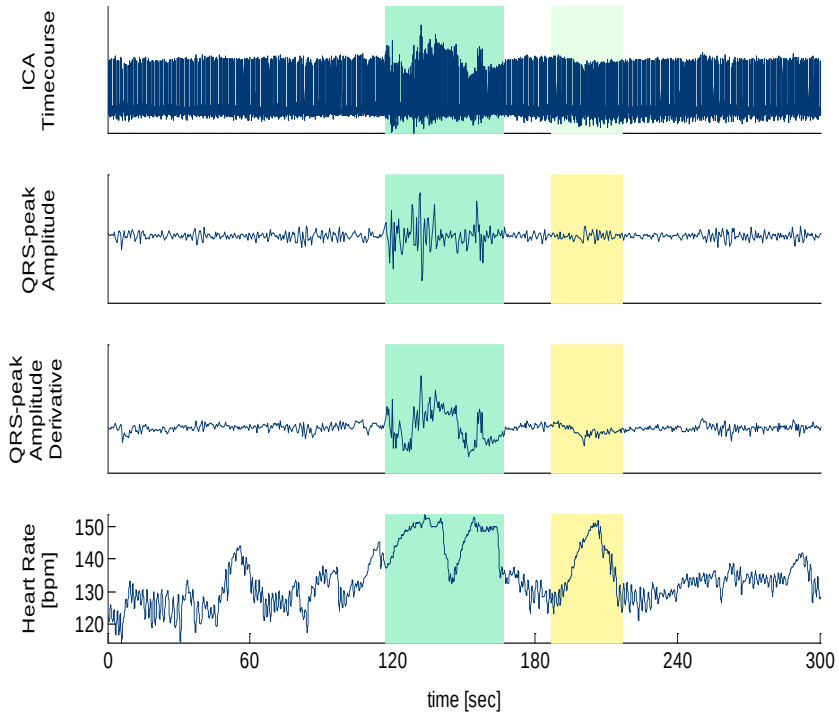

Figure 4.6 Detection of fetal movement is shown on a 5 min fMCG recording from a 34 week old fetus. The upper trace shows a fetal cardiac ICA component. The second trace shows the QRS peak amplitude, and the third trace shows the derivative of the QRS peak amplitude signal. Significant signal variability due to fetal movement is noticed around 140 sec, and is accompanied by an increased heart rate (bottom trace). The technique allows discriminating between spontaneous (yellow) and movement-related (green) heart rate accelerations.

4.4. Solving the inverse problem: recursive multiple signal classification

The inverse problem of fMCG can be interpreted as converting fMCG measurements, which in the 83-channel recordings in our study, into information about fetal cardiac vector. To solve the inverse problem, a previous study (Popescu *et al.* 2006b) has proposed and tested a recursive multiple signal classification (R-MUSIC) algorithm for multichannel fMCG data, using a 300-dipole simulated

heart model. Compared to other reconstruction algorithms such as Downhill Simplex Method, R-MUSIC estimates the cardiac source based on the spatio-temporal data (instead of spatial mapping only) using the covariance of the measured data over a temporal interval , and can provide the time-course of activity over that temporal interval rather than at a single snapshot. The R-MUSIC algorithm described in (Mosher and Leahy 1999, Mosher and Leahy 1998, Popescu *et al.* 2006b) is implemented in our study and the retrieved dipoles are subsequently used to estimate the time-course of the cardiac vector on the duration of the averaged QRS complex.

4.5 .The Effect of Source Correlation on the Reconstructed Cardiac Vectors in Fetal Magnetocardiography

The study of (Popescu *et al.* 2006b) finds that the accuracy of R-MUSIC may degrade when the cardiac axis is radially oriented. To evaluate the role of source correlation on estimation of fetal cardiac vectors and the effect the model order underestimation, we fit multi-dipole circumstances with single dipole model in a series of simulation experiments. The performance of a subspace correlation metric to select the model order was also examined.

Simulations were made at three depths with different, fully correlated (figure 4.8), Gaussian-shaped dipole pairs, whose positions were systematically varied across horizontal (xy) cross-sections throughout the source space. For each dipole set, six distances between dipole pair were selected at each time, 0.6, 1.2 and 2.0 cm along x-axis, and the same for y-axis. For each pair of locations, the orientation of each of

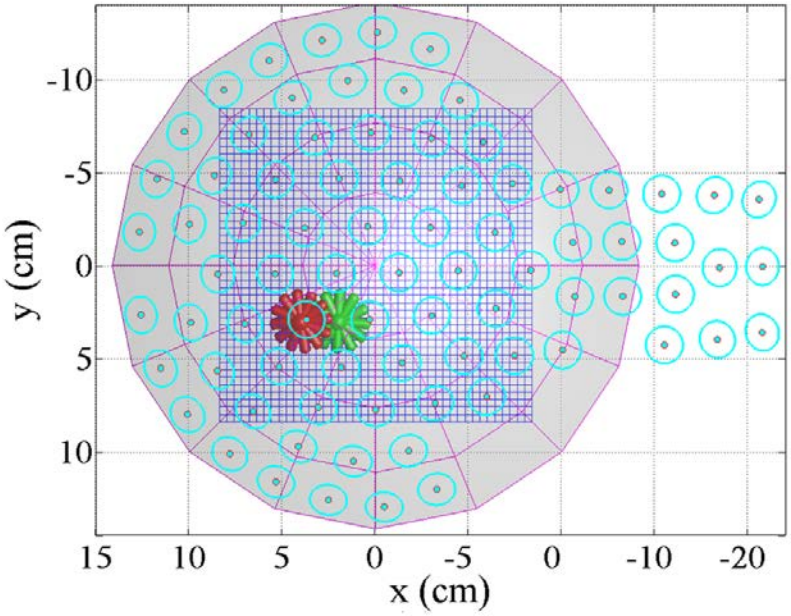

Figure 4.8 Setup of the simulation experiments focusing on the effect of source correlations. The biomagnetic sensors, spherical volume conductor and the reconstruction grid are shown along with the simulated dipolar sources in one condition.

the dipoles was varied in steps of π/12 rad with respect to the local declination direction within the corresponding tangential plane to a spherical volume conductor.

We find that when source correlation is not taken into account, the MUSIC metric may exhibit spatial peaks at locations corresponding to "virtual" sources, whose leadfield vectors ("gains") achieve best approximations for a linear combination of the leadfield vectors of the correlated sources (exemplified in Figure 4.9).

The results also show that localization error increases with the increase of angle and distance between two sources (figure 4.10). Absolute amplitude is minimized when the angle is close to π/2 rad, and increase when it approaches 0 or π rad. Absolute and relative mean amplitude errors show a significant change with source position and orientation. In conclusion, single dipole model provides good estimators

of the net current when two correlated sources are in close proximity, relatively far from sensors and with a 2π/3 orientation. Also, the subspace correlation metric can be used to aid the selection of the model order.

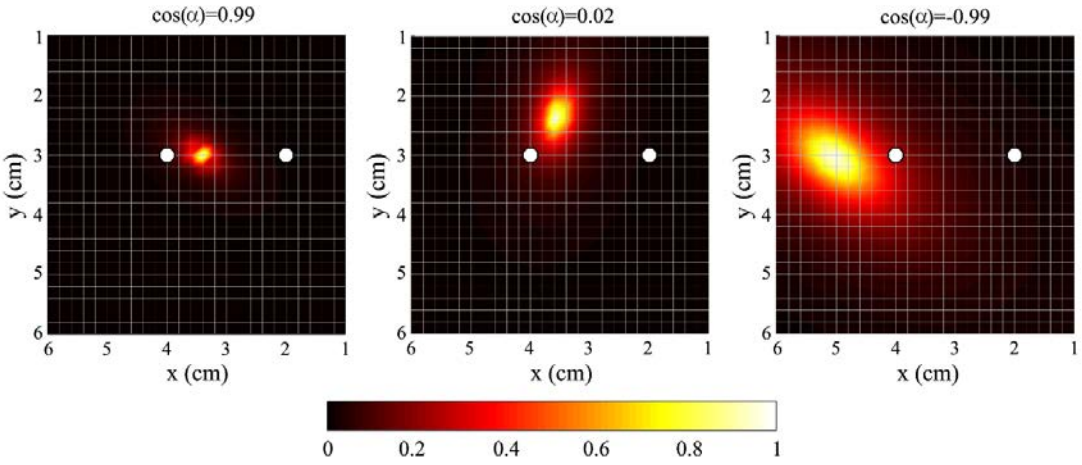

Figure 4.9 An example of simulation experiments focusing on the effect of source correlation (a) Parallel dipoles, (b) orthogonal dipoles, and (c) anti-parallel dipoles.

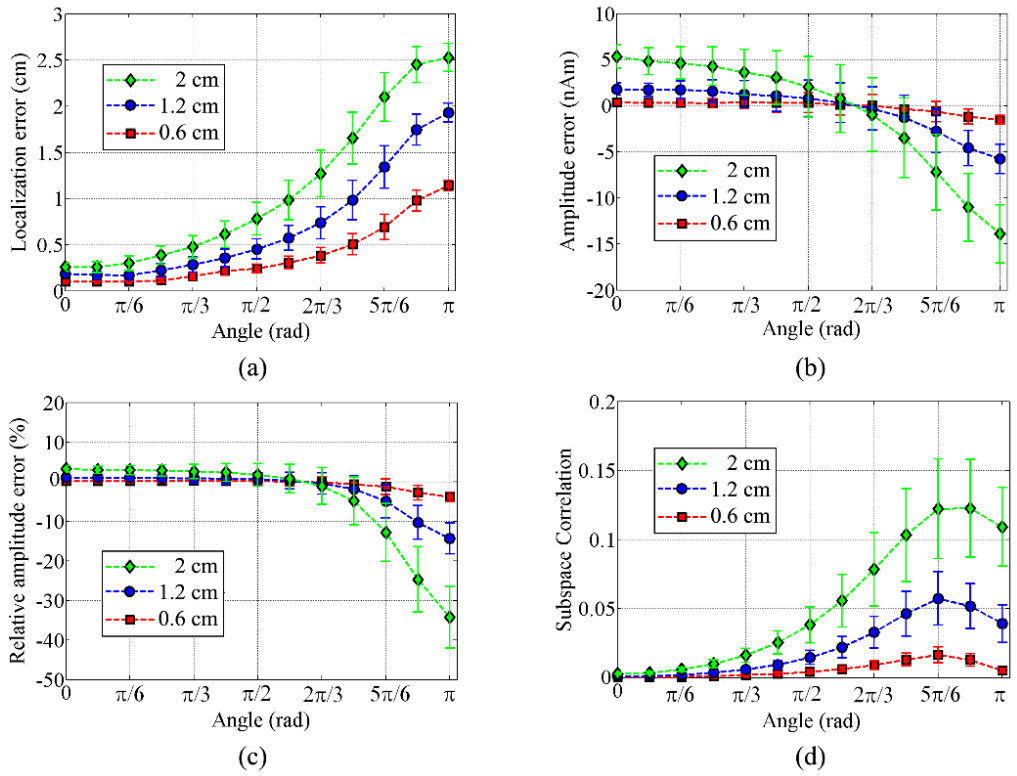

Figure 4.10 Summary of results across all simulated conditions. Localization errors (a), amplitude errors (b), relative amplitude errors (c), and subspace correlation (d) are shown as mean and SD. The angles between the simulated dipoles were clustered in bins ($\pi/12$ rad wide) and results were plotted at the center of each bin.

CHAPTER 5 THE EFFECT OF VOLUME CONDUCTOR MODELING ON THE ESTIMATION OF CARDIAC VECTORS IN FETAL MAGNETOCARDIOGRAPHY

Previous studies based on fetal magnetocardiographic (fMCG) recordings used simplified volume conductor models to estimate the fetal cardiac vector as an unequivocal measure of the cardiac source strength. However, the effect of simplified volume conductor modeling on the accuracy of the fMCG *inverse solution* remains largely unknown. Aiming to determine the sensitivity of the source estimators to the details of the volume conductor model, we performed simulations using fetal–maternal anatomical information from ultrasound images obtained in 20 pregnant women in various stages of pregnancy. The magnetic field produced by a cardiac source model was computed using the boundary-element method for a piecewise homogeneous volume conductor with three nested compartments (fetal body, amniotic fluid and maternal abdomen) of different electrical conductivities. For late gestation, we also considered the case of a fourth highly insulating layer of *vernix caseosa* covering the fetus. The errors introduced for simplified volume conductors were assessed by comparing the reconstruction results obtained with realistic versus spherically symmetric models. The results show that the present methodology overcomes the drawbacks of conventional ECD fitting, by providing robust estimators of the cardiac vector. Additional evaluation with real fMCG data show fetal cardiac vectors whose morphology closely resembles that obtained in adult MCG.

5.1. Introduction

Fetal magnetocardiography (fMCG) has emerged as an attractive technique for *in utero* assessment of cardiac electrophysiology, especially for its significant potential in assessing pathophysiological conditions (Leeuwen *et al.* 2000, Wakai *et al.* 1998a, Hamada *et al.* 1999, Cuneo *et al.* 2003, Comani *et al.* 2004). The major advantage of fMCG over fetal electrocardiography (fECG) is given by its notably superior signal quality, as the magnetic field is considerably less affected by tissues with low electrical conductivity (Cuffin 1978), which can drastically diminish the amplitude of the fECG signals. As a result, fECG is rarely recorded successfully in obese individuals, and it is considerably compromised by the formation of the electrically insulating *vernix caseosa* in late pregnancy. In contrast, the magnetic recordings allow high-resolution measurements from the second trimester of gestation to birth.

The fECG and fMCG signal morphology is influenced by the fetus position relative to the sensing system and by the geometry and electrical conductivity of fetal and maternal tissues surrounding the fetal heart. These factors modulate the recorded cardiac cycle waveforms and may prevent a straightforward comparison of the signals amplitude across subjects. One approach to this problem is to examine the fetal cardiac activity in source space rather than sensor space. Early fECG studies investigated the role of volume conductor on the estimation of fetal cardiac vectors and fetal vector loops (FVL) (Oostendorp *et al.* 1989c). Before 28 weeks of gestation, the electric potential distribution at the maternal abdomen was quite well approximated by homogeneous conductors and a dipole model of the fetal heart.

FVLs obtained with this approach were similar to those of newborns (Ellison and Restieaux 1972), but the source strength was significantly underestimated when compared to predicted data from animal studies (Nelson *et al.* 1975). The vector magnitude (VM) estimates were improved by refining the volume conductors to account for the fetal body and amniotic fluid. After 28 weeks, however, the fECG amplitude drops significantly, and the volume conductor requires additional compartments to model the insulating vernix. Also, the possible presence of non-uniformities or holes in the vernix may play a significant role on the amplitude and distribution of the electric potential measured by fECG.

The volume conductor non-homogeneities affect differently the electric potential (measured by fECG) versus the magnetic field (measured by fMCG). One consequence is that the electric potential on the maternal abdomen vanishes in the presence of insulating layers, while the magnetic field does not. In addition, plane-parallel layered volume conductors or those with nested compartments approaching spherical symmetry can be approximated by simplified homogeneous models in biomagnetic applications, overcoming the need to know the electrical conductivity or to account for the presence and precise geometry of compartments with different conductivities. Assuming that magnetic fields are less influenced by nonhomogeneities in the conductivity of the maternal abdomen and fetal body compartments, more recent fMCG studies (van Leeuwen *et al.* 2004c, Horigome *et al.* 2001, Popescu *et al.* 2006a) used reconstruction techniques to estimate the fetal cardiac vectors by considering either half-space or spherically symmetric volume

conductors. These simplified models allow using closed-form analytical solutions of the forward field (Sarvas 1987b, Ilmoniemi *et al.* 1985) and do not necessarily require imaging of the fetal–maternal unit, which could represent substantial practical benefits. Although each of these studies acknowledged the potential limitations of the strategy, the results of this effort showed promise for characterizing the strength of the cardiac vector with fetal growth (van Leeuwen *et al.* 2004b), or to diagnose prenatal hypertrophy (Horigome *et al.* 2001). On the other hand, data from computational studies indicate that the influence of non-homogeneities in fetal–maternal anatomy on the *forward solution* of the magnetic field can be substantial (Stinstra *et al.* 2002b). The extent to which these modulations affect the inverse fMCG solution when simplified conductors are employed remains however uncertain.

One way to address this issue is to conduct a systematic investigation looking at how the simplified volume conductor modeling is directly reflected in the accuracy of the fMCG *inverse solution*. For this purpose, we used realistic approximations of the volume conductor derived from 3D ultrasound images of the fetal–maternal anatomy. Computer simulations were carried out to characterize middle and late gestation by considering three-compartment (i.e. fetal body, amniotic fluid and maternal abdomen) volume conductors, with a fourth compartment added to account for an *uniform* layer of *vernix caseosa* in late gestation. More complex models, e.g., including holes in the vernix have also been considered by studies using forward magnetic field simulations (Stinstra *et al.* 2002b). For the purpose of our study, however, we focus on only two cases with 3 or 4 nested compartments separated by closed surfaces, which can in

principle favor the use of simplified spherical models. The impact of more complex modeling of the vernix layer will be discussed in the last section, in light of the present findings. The geometry of the boundary surfaces for compartments of different conductivity varies significantly between subjects and gestational ages (GA). In addition, the accuracy of the inverse biomagnetic solution may also depend on such factors like the source model, choice of source space and optimization algorithm. Thus, we determined that the use of, e.g., a single or just a few setups to characterize the effect of volume conductor modeling is insufficient, since the way the findings generalize would remain unknown. To overcome these issues, we use ultrasound data from a relatively large number of subjects, and we evaluate the accuracy of the inverse solution for two optimization schemes, in scenarios that incorporate different volume conductor models, and none or minimal information on the approximate source location. This strategy allows us to cross-validate the results and to demonstrate the effect of volume conductor modeling on the accuracy of the inverse fMCG solution. Finally, a comparison of the inverse solutions obtained with realistic approximations of the volume conductor versus spherically symmetric models is conducted using real fMCG data recorded in mid-gestation.

5.2. Methods

5.2.1. Cardiac vector estimation in fMCG

The cardiac muscle depolarization involves spatially propagating waves that can be described by a dense distribution of current sources (Malmivuo and Plonsey 1995).

When measurements are performed at relatively large distances from the source distribution, the magnetic field appears to be generated by an equivalent current dipole (ECD), such that the ECD strength and orientation approximate at any time the vector summation of all simultaneously active current sources. This represents the magnetic equivalent of the electric cardiac vector concept applied in adult ECG.

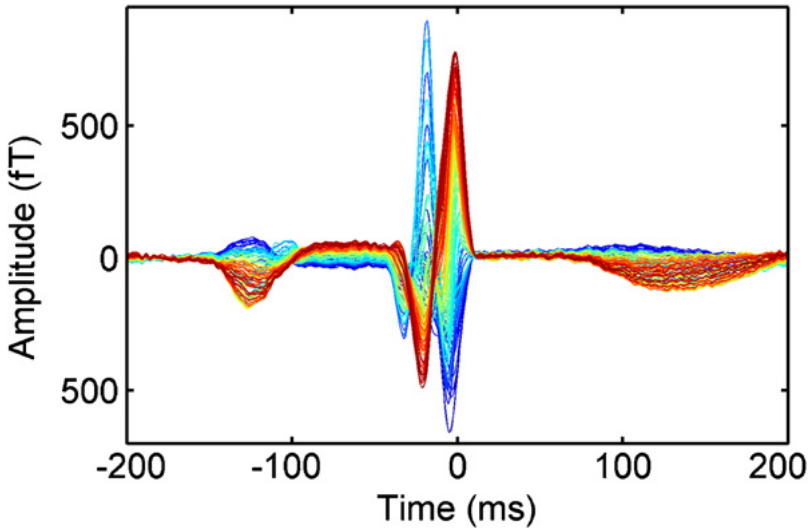

Figure 5.1 fMCG signals exemplifying an averaged QRS complex from a 36 week old fetus.

Under this hypothesis, initial studies have used the ECD model to fit the fMCG data at the peak of the QRS complex (Van Leeuwen *et al.* 2004a, Horigome *et al.* 2001). Since the ventricular depolarization generates fMCG signals that differ substantially across sensors (figure 5.1), one potential difficulty is to select the QRS time point that corresponds to a unique and well-defined phase of ventricular depolarization, e.g., the instant of maximum net cardiac current or the maximum cardiac VM (MCVM). Using a single (e.g. most sensitive) channel or the mean global field (MGF) across channels to determine the time point of highest signal amplitude remains vulnerable to uncertainties introduced by the time-varying behavior of the cardiac vector orientation. In addition, the ECD model is predicated on the

assumption of a small size of the fetal heart and a relatively large source-to-sensor distance. The validity of this assumption relates to the spatial resolvability of dipolar sources and depends on factors, such as the (unknown) source parameters, or the (known) sensors distribution and configuration. In general, the number of large singular values of the spatio-temporal data matrix indicates that a single fixed dipole may not necessarily explain well the whole QRS data in fMCG recordings. Thus, in our study, we evaluate two alternative approaches, which offer more flexible frameworks for fitting the fMCG data on the whole QRS interval: a rotating dipole and a multiple-dipole model. A rotating dipole may be viewed as three collocated fixed dipoles with independent time series, such that its orientation varies with time. The multi-dipole model does not require individual dipoles to be co-located. In this case, the cardiac vector is obtained from the vector summation of all individual dipoles. Estimating the cardiac vector at any instant in time allows for a direct identification of the MCVM latency on the VM waveforms. Furthermore, the time course of the VM would in principle enable other cardiac measurements of interest, such as the waves duration or time-amplitude integrals.

5.2.2. Ultrasound recordings

Using realistic approximations of the volume conductors in fMCG requires the 3D segmentation of the boundary surfaces of several fetal–maternal anatomical compartments with different electrical conductivities (Stinstra *et al.* 2002a). The 3D images of the fetus and maternal abdominal tissues must be acquired immediately

before or after the fMCG recording (to minimize the risk of fetal repositioning), limiting the use of MRI. For the current study, we used the so-called free-hand 3D ultrasound, in which a 3D digitizer is attached to an ultrasound probe to record the positions and orientations of the probe simultaneously with the B-scans, for subsequent co-registration and reconstruction of the volumetric data. To achieve this task, we used the Stradwin 3D Ultrasound Acquisition and Visualization software (Cambridge University, UK) with a GE Logiq-P5 ultrasound system and a TrakSTAR positioning digitizer system (Ascension Technology Corporation, USA) attached to the ultrasound probe. The calibration of the probe-digitizer system was performed with an ultrasound phantom. For the purpose of our simulation studies, 3D images of the fetus and maternal abdominal tissues were acquired from 20 pregnant women. Informed consent was obtained from each subject before participation in the experiment. The study was approved by the Institutional Review Board of the University of Kansas Medical Center. Data from 10 subjects were recorded between 22 and 28 weeks of gestation, while the remaining 10 subjects were recorded between 32 and 36 weeks. For each case, series of images were acquired by scanning the maternal abdominal surface from side to side and upper to lower abdomen for a total number of ~5000–6000 frames.

Co-registration of the ultrasound images with the fMCG sensor array was accomplished using three fiducial markers placed at non-collinear locations on the maternal abdomen (right side, left side, and sternum). Each marker's location was recorded by positioning the center of the ultrasound probe at that location and

recording the corresponding frames. These frames were used to identify the markers locations on the volumetric image, but were excluded from subsequent processing. The markers positions relative to the fMCG sensors were determined in the biomagnetometer by localizing three coils placed at those locations.

5.2.3. Processing of volumetric ultrasound images

We developed a standard approach to model the fetal body compartment of the volume conductor. The fetal head and trunk were approximated for each subject with a sphere and an ellipsoid, respectively. This methodology relied on the manual identification of two fiduciary points and on performing two standard biometric ultrasound measurements: the abdominal circumference (AC) and the head circumference (HC). Based on these measurements, two parameters used to model the fetal body were derived: (1) the extent of the small axis of the ellipsoid used to model the fetal trunk (using AC) and (2) the radius of a sphere used to model the fetal head (using HC). The fiduciary points used to model the fetal body were the fetal head center and the fetal coccyx, which were manually identified on the recorded B-scans. The long axis of the ellipsoid (fetal trunk) was defined from the head center to the coccyx, with the ellipsoid center set at the middle of this line. The fetal body was subsequently modeled as the merged volume of the ellipsoid and sphere determined as described above. The amniotic sac (AS) was approximated by an ellipsoid with size and position determined from manually identified fiduciary points. These points defined the ends of the long axis of the sac ellipsoid in longitudinal cross-sections

through the fetal head and spinal cord, and the AS center (middle of the long axis), and were used to estimate the length of the short axis of the ellipsoid (passing through the AS center).

The ultrasound volumes were then resliced using planes oriented in the axial direction relative to the maternal abdomen. Resliced frames along with the coordinates of the fiduciary points were processed in Matlab to set the voxels of the fetal body and AS compartments to predefined intensity levels. An additional dark gray layer has been added to represent the outer maternal abdominal skin. The images were transformed to ANALYZE format for a final processing step involving the segmentation of the different compartments (performed with CURRY 5.0, Compumedics Neuroscan). All compartments were visually inspected, and the AS compartment was locally adjusted using regional 3D dilation and/or setting pass markers to improve its local shape and to ensure that the fetal body and AS compartments did not intersect with each other. The triangularization of the boundary surfaces was done using average triangle sides of 5, 10 and 20 mm for the fetal body, AS and abdominal compartments, respectively. For late gestational data, a 5 mm dilation of the fetus compartment was used to derive a vernix mesh with an average triangle side of 5 mm. Source space points were created inside the middle part of the fetal trunk as a regular grid with 3 mm average spacing and no points at less than 5 mm from the fetal body surface. Surfaces (exemplified in figure 2) and source space points were used for further processing in Matlab. Across subjects and models, the total number of vertices varied between 2598 and 9828.

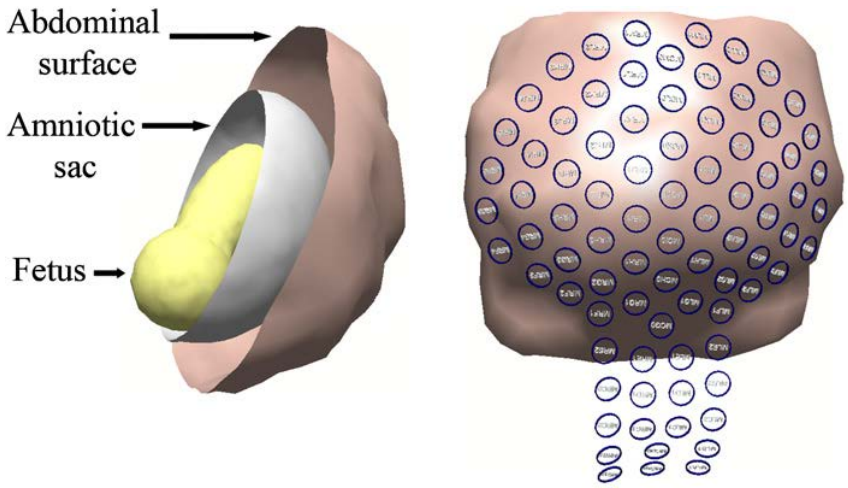

(a) (b)

Figure 5.2 (a) Exemplification of boundary surfaces modeling for a three-compartment volume conductor. (b) Top view of the outer abdominal surface co-registered with the biomagnetic sensor array.

5.2.4. Simulation experiments

Simulation experiments were performed for the sensor array of the CTF fetal biomagnetometer with 83 axial gradiometers (with 5 cm distance between the pick-up coils of each sensor). The magnetic field was simulated under two conditions. First, we defined three-compartment volume conductors for the whole set of 20 subjects (using both middle and late gestation setups).We assigned conductivities of 0.22 S m^{-1} to the fetus, 1.4 S m^{-1} to the amniotic fluid and 0.05 S m^{-1} to the maternal abdomen(Stinstra *et al.* 2002a). In a second condition, setups from late gestation (10 subjects) were also used in simulations with four-compartment volume conductors. In this case, a fourth compartment (5 mm thick, conductivity of 2×10^{-6} S m^{-1}) covered the fetus to test for potential differences introduced by the presence of vernix.

The general principle of our simulation approach is that the cardiac electrical activity can be described as a current distribution of elementary current sources that summate into a few effective dipoles, which can be reconstructed from multi-channel fMCG measurements. The number of effective dipoles depends on factors such as the position and orientation of the heart with respect to the sensor array as well as the heart size and, therefore, can show significant inter-subject variability. Since the number of effective dipoles is unknown a priori, we modeled the heart using a large number of elementary currents, and we tested the reconstruction algorithms for retrieving the data-driven or subject-dependent (small) number of effective dipoles. Thus, to simulate the forward magnetic field, we used a fetal heart source model that approximates the propagation of the depolarization wavefront through the ventricular walls during the QRS interval (Popescu *et al.* 2006a). The model uses a modulated profile cylindrical surface to seed elementary current dipoles around the cardiac axis. For middle gestation, the radius of the largest heart circumference was R = 0.75 cm, and the ventricular dimension along the heart axis was Z = 1.5 cm. For late gestation, we selected R = 1.5 cm and Z = 3.0 cm. The peak current latencies were parameterized to generate a traveling wave progressing from the apex to the ventricles' upper part. A total of 480 time samples were generated with 1200 Hz sampling rate. The VM was derived by vector summation of all currents at each time point, and the currents strengths were scaled such that the peak VM was 853 and 1706 nAm for middle and late gestation, respectively. The heart source model was positioned at the fetal heart location identified on ultrasound images and the forward magnetic field was computed at the

sensor positions using the BEM linear-collocation approach. White Gaussian noise (RMS = 3 fT) was added to the data.

5.2.5. Source reconstruction and evaluation of the volume conductor effects

Source reconstruction results were evaluated for two algorithms: (1) a multiple-dipole search using R-MUSIC (Mosher *et al.* 1999), and (2) fitting of a single rotating-dipole using a least-squares source scanning (RDSS) to find the location which minimizes the relative residual deviation, ε, between the measured (B) and estimated data (R_i) on the QRS interval:

$$\varepsilon = \frac{\left\| \boldsymbol{R}_i - \boldsymbol{B} \right\|}{\left\| \boldsymbol{B} \right\|} = \frac{\left\| \boldsymbol{L}_i \boldsymbol{L}_i^{+} \boldsymbol{B} - \boldsymbol{B} \right\|}{\left\| \boldsymbol{B} \right\|}, \qquad (5.1)$$

where L_i is the $m \times 3$ location-wise gain matrix, and (+) denotes the pseudoinverse of a matrix. Note that in a spherically symmetric volume conductor, currents along the radial direction do not produce any magnetic field outside the volume conductor (Sarvas 1987b), and in this case L_i is the $m \times 2$ matrix formed by the gain column vectors along each of the two local tangential directions.

The source-space scanning approach for fitting a rotating dipole has been preferred to alternative nonlinear minimization algorithms, since the latter can sometimes provide erroneous results due to their vulnerability to getting trapped in local minima(Popescu *et al.* 2006b).The R-MUSIC algorithm searches over a 3D grid to find locations for which a linear combination of columns of the gain matrix $\mathbf{L_i}$ projects entirely onto the *signal subspace* of the spatio-temporal data matrix. This is achieved using *subspace correlation* metrics (Mosher and Leahy 1999). Once a first dipole is

identified, the algorithm is repeated to search for other sources which explain the remaining data. The rank of the signal subspace was set to 5 for all the experiments presented herein. Also, we used a threshold value of 0.95 for the subspace correlation to represent an adequate correlation of a source. The recursions stop when the number of dipoles found equals the signal subspace rank, or when no more sources satisfying the threshold subspace correlation are found. When the algorithm stops, the dipoles magnitudes are estimated by multiplying the data matrix by the pseudo-inverse of the dipoles gains matrix.

Each reconstruction scheme was applied within three scenarios characterized by a different choice of the *volume conductor model* and/or *source space* selection. First (*scenario 1*), we evaluated the reconstruction strategies for the case when perfect knowledge of the volume conductor is available and the source space is confined to the middle part of the fetal trunk volume. This evaluation is necessary to characterize the errors introduced by the limited number of sensors, presence of noise in the data, and intrinsic properties of the reconstruction algorithms. Second (*scenario 2*), a sphere fitted to the sensors was used as a simplified volume conductor model. This scenario assumes also that minimal information about the fetal body position is available, such as an approximate fetal heart-to-sensors distance (as proposed, e.g., by Horigome *et al* 2001). To account for this, the source space was selected to coincide with the grid in scenario 1, *i.e.* confined to the middle part of the fetal trunk. The gains were computed using the Sarvas equations of the forward magnetic field (Sarvas 1987). Finally, *scenario 3* assumed the same spherical volume conductor model, with a source space

that spanned a large (14 cm x 25 cm x 18 cm) rectangular volume inside the upper hemisphere of the volume conductor, to replicate conditions in which anatomical information is unavailable.

The performance of the two reconstruction schemes was evaluated by means of the estimated cardiac *vector magnitude* ($\tilde{VM}$). For R-MUSIC, $\tilde{VM}$ is the net current strength derived at each time by vector summation of the reconstructed dipoles. Amplitude errors were assessed by the *relative error* of the peak $\tilde{VM}$ *(reVM)* with respect to the known peak *VM* amplitude. We use the convention that positive and negative errors indicate VM underestimation and overestimation, respectively. The localization performance was evaluated by the Euclidian distance between the heart geometrical center and the average location of the retrieved dipoles (R-MUSIC) or the location of the best-fit rotating dipole (RDSS). The relative residual deviation (1) was used to characterize the goodness-of-fit.

5.3. Results

5.3.1. Three-compartment volume conductors

Figure 5.4 a, b exemplifies the estimated VMs and summarizes the results for data simulated with 3-compartment volume conductor models (panels c, d). With perfect knowledge of the volume conductor (scenario 1), the R-MUSIC and RDDS schemes provide good VM estimates (overall mean errors of 3.0±9.5% and 1.0±11.5%, respectively) and small localization errors (overall mean values of 0.9±0.4 cm and 1.0±0.5 cm, respectively), irrespective of the gestational age (early vs. late). The *reVM*

data for both R-MUSIC and RDSS passed D'Augustino-Pearson omnibus normality tests ($K2$s<023, ps>0.89), and subsequent two-tailed t-tests indicated that mean *reVM* values were not significantly different than zero (ts<1.4, ps>0.18). In order to test if any reconstruction scheme performs better for this scenario, we treated the *reVM* as a dependent variable, and we conducted a 2x2 ANOVA with independent factors *reconstruction algorithm* (with repeated measures for R-MUSIC vs. RDSS) and *gestational age* (early vs. late). The test showed no significant main effects or interaction (Fs<0.32, ps>0.58).

The use of simplified volume conductors led to relatively large *reVM*s for each reconstruction scheme and source space selection. *reVM*s were positive for all subjects and scenarios (2 and 3) tested, indicating a clear trend of underestimating the true VM. Similar 2x2 ANOVAs as explained above were conducted separately for scenarios 2 and 3, indicating a significant main effect of *reconstruction algorithm* in each case (scenario 2: F=9.6, p=0.004; scenario 3: F=5.3, p=0.03), but no significant main effects of gestational age or interactions. The optimal reconstruction algorithm in these scenarios (*i.e.* RDSS) has been further tested to see if the selection of the source space affects its performance. This was done using separate 2x2 ANOVAs with the *localization error* and *reVM* as the dependent variables, and independent factors *scenario* (with repeated measures for scenario 2 vs. scenario 3) and *gestational age* (early vs. late). These tests indicated a significant main effect of scenario (F=11.2, p=0.003) on the localization error, but no significant main effects on *reVM* (Fs<1.15, ps>0.29). Thus, the high *reVM*s are largely determined by the mismatch between the

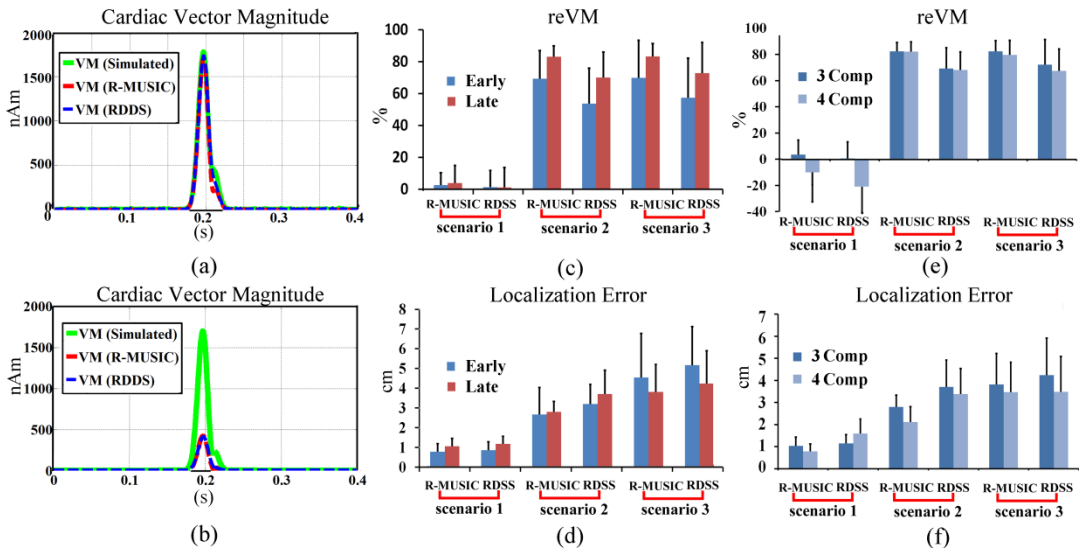

Figure 5.4 (a) Exemplification of cardiac VM estimation for one subject (32 weeks of gestation, 3-layer case, scenario 1). (b) Exemplification of cardiac VM estimation for the same subject in scenario 3. (c) rEVM for different scenarios. (d) Localization errors for different scenarios. (e) rEVMs for 3-layer and 4-layer volume conductors in late gestation. (f) Localization error for 3-layer and 4-layer volume conductors in late gestation.

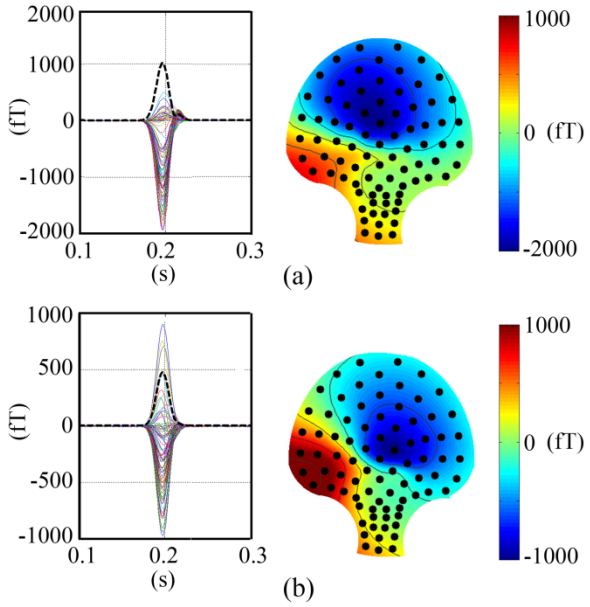

Figure 5.5 Exemplification of simulated data with 3-compartment (a) and 4-compartment (b) volume conductors. The dotted lines show the mean global field. The peak-magnetic field distribution is shown on the right.

gains in realistic and simplified models, and so, they are not significantly improved by the confinement of the source space to the fetal trunk. The *residual deviation* increases with the use of simplified volume conductors. In *scenario 1* both R-MUSIC and RDSS solutions explained well the signals (overall mean residual deviation of 7.6±6.0% and 5.6±3.8%%, respectively, pooled over gestational ages). For simplified volume conductors however, a significant part of the signals remains unexplained: the mean residual deviation was 48.4±30.6% in scenario 2 and 40.9±28.2% in scenario 3 for R-MUSIC, and 31.1 ±13.8% in scenario 2 and 25.8±11.3% in scenario 3 for RDSS.

5.3.2. Impact of vernix caseosa

Figure 4e, f compares the results for 3-compartment vs. 4-compartment volume conductors. Since both models are derived from the same group of subjects (late gestation), the differences reflect the role of the insulating layer of vernix. This layer can change the magnetic field distribution and typically lowers the mean global field across sensors (Figure. 5.5).

A 2x2 ANOVA was conducted for *scenario 1*, with the dependent variable *reVM* and independent factors *reconstruction algorithm* and *volume conductor model* (with repeated measures for 3-compartment vs. 4-compartment). The test showed a significant main effect of *volume conductor model* (F=6.4, p=0.02), indicating a trend for both R-MUSIC and RDSS to retrieve less accurate solutions for the 4-compartment data. Similar ANOVAs for scenario 2 and 3 showed no significant effects or interactions (Fs<0.65, ps>0.64). Thus, the presence of an uniform layer of vernix does

not change the effect of imperfect volume conductor modeling. ANOVAs for the localization error showed no significant effects in any scenario ($Fs<1.6$, $ps>0.22$).

5.3.3. Assessment on real fMCG data

The use of realistic approximations of the volume conductor was tested in a preliminaryevaluation with real fMCG measurements collected in mid-gestation, to avoid uncertainties about the presence of vernix. Fifteen pregnant women (GA 23 to 25 weeks) undergone a continuous 4 min fMCG recording (1200 Hz sampling rate, 0.5–200 Hz band pass). The signals were filtered using ICA (Mantini *et al.* 2006) to segregate the contribution of the fetal cardiac source. Data from four subjects were discarded due to gross fetal body movements during the recording, identified as non-stationarities of the QRS amplitude in the sensor signals, associated with shifts of

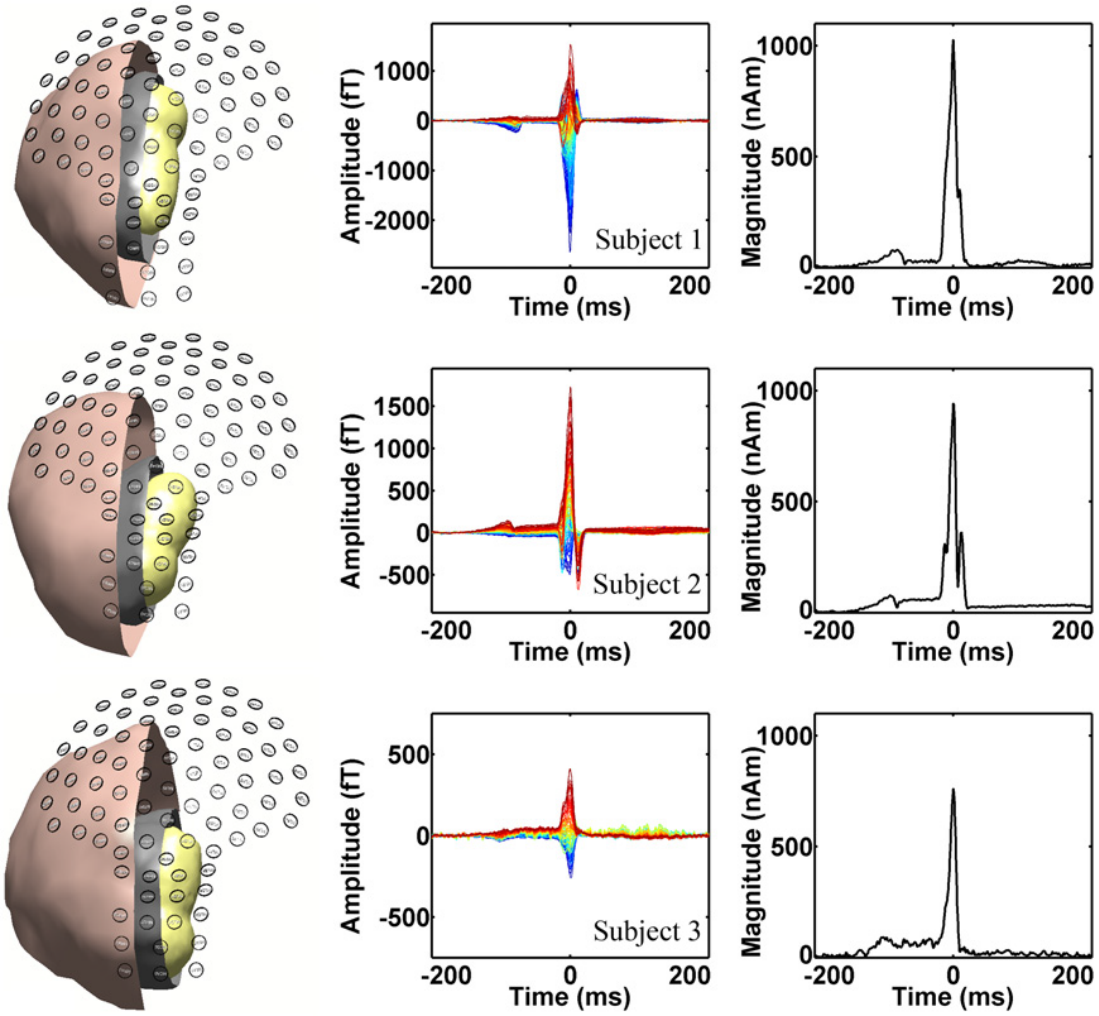

Figure 5.6. Estimates of cardiac VM using realistic approximations of the volume conductor are exemplified for three subjects. The left panels show the volume conductor co-registered with the sensor array. One fetus (subject 1, data recorded at 23 weeks, 6 days) was in breech position, while the other two fetuses (subjects 2 and 3, data recorded at 24 weeks, 4 days for each of these two fetuses) were in cephalic positions. The middle panels show the averaged fMCG data, and the right panels show the corresponding VMs. The three cases were selected to exemplify the large variability in amplitude and morphology of the fMCG signals across subjects: the peak-to-peak QRS amplitude varies between ~4 pT (subject 1) and ~0.7 pT (subject 3).

the fetal cardiac source activity from one independent component to another. For the remaining subjects without observable fetal body movement, the QRS peak was detected by an automatic algorithm, and the averaged cardiac beat was estimated and used for source reconstruction. Free-hand ultrasound images acquired immediately after the fMCG recordings were processed as explained in section 2 to derive three-layer realistic approximations of the volume conductor. Figure 4.6 exemplifies the averaged fMCG data and the reconstructed cardiac vectors using R-MUSIC. Out of the 11 subjects, a good fitting (>90% explained data variance) was obtained in five cases, a moderately good fitting (between 75% and 90% explained data variance) was obtained in four cases, and a low-quality fit (<75% explained data variance) was obtained in two cases. The mean cardiac vector peak magnitude was 747 ± 259 nA m across the five subjects with good fitting, and 872 ± 319 nA m across all nine subjects with good and moderately good fitting. Simplified spherical models were also used for comparison: with this strategy, the mean peak-magnitude obtained across the same nine subjects was 227 ± 103 nA m, and the mean explained variance was 52 ± 0.25%. These results allow making several observations. First, the peak-magnitude estimators obtained with simplified volume conductors generally agree with the ones reported by previous fMCG (Leeuwen *et al* 2004, Horigome *et al* 2001) and fECG (Oostendorp *et al.* 1989b) studies using similar reconstruction strategies. Second, the refinement of the volume conductor to include non-homogeneities introduced by the fetal body and AS *increases* the estimated values of the vector peak magnitude and improves the goodness-of-fit for most subjects. Finally, the values of the vector peak magnitude in

these cases are closer to those predicted by studies on vertebrate animals, which indicate an expected mean value of ~750 nA m for this range of GA (Nelson *et al.* 1975, Alexander *et al.* 1998). Thus, although the magnetic field is apparently less sensitive to the details of the volume conductor than the electric potential, these results indicate that the refinement of the volume conductor model for mid-gestation to account for inhomogeneities introduced by the fetal body and AS apparently improves the VM estimation in fMCG in a similar manner as previously reported for fECG (Oostendorp *et al* 1989b).

5.4. Discussion

A reliable methodology for the estimation of the cardiac signal strength from fMCG data can extend its clinical usefulness by allowing studies of fetal cardiac electrophysiology in conditions associated with increased risk of cardiac hypertrophy. Our study used realistic approximations of the volume conductor for a relatively large number of subjects and demonstrated the limitations of using simplified models to achieve this objective. These findings are similar to observations made by earlier studies using fECG (Oostendorp *et al* 1989b) and challenge the view that magnetic recordings would be less sensitive to the details of the volume conductor to such extent that they would allow the use of simplified models in experimental applications.

We showed that the simplified volume conductor models lead to significant and consistent underestimation of the cardiac vector, with a mean-retrieved peak amplitude ranging from 20% to 50% across the scenarios tested in our study, irrespective of

factors like the selection of the source space or reconstruction scheme. These results, as well as our preliminary findings with real fMCG measurements, can largely explain an apparent discrepancy between the vector peak magnitude reported previously by fMCG studies using simplified models (Leeuwen *et al* 2004, Horigome *et al* 2001) and the values predicted by studies on vertebrate animals (Nelson *et al* 1975).

For late gestation, the above observations were made using simulations in two limit cases, i.e. in the complete absence or presence of a uniform layer of vernix. In real experiments, it is likely that intermediate states (i.e. patches of vernix covering partially the fetal body) may be encountered after 28 weeks of gestation. The presence of holes in the vernix has been shown to change the amplitude and distribution of the electric potential on the maternal abdomen, as well as the forward magnetic field (Oostendorp *et al* 1989b, Stinstra *et al* 2002). The errors in the fMCG inverse solution for simplified models that approximate conductors with nested compartments and uniform layers of vernix indicate that similar or larger inaccuracies would be also obtained for such spherically symmetric approximations of more complex conductors that include additional inhomogeneities introduced by the presence of holes in the vernix. Since there is no reliable way to gain evidence for the presence of vernix in practical applications, or to determine the existence and size of its holes, effort to define and use realistic approximations of the volume conductors will most likely find applications in a 'window of opportunity' between approximately 22 weeks of gestation (when reliable fMCG recordings can be obtained) to approximately 28 weeks (when uncertainties about the presence of vernix would start to impact the modeling and its success rate).

From this perspective, fMCG measurements have several advantages compared to the early fECG studies: (1) the availability of large arrays systems with dense sensor coverage, (2) the availability of new computational methods for eliminating interferences from maternal cardiac and other artifacts (e.g. ICA), which allow more accurate estimation of the averaged fetal cardiac signals and (3) recent advances in *free-hand* ultrasound recording and processing, which can facilitate the definition of realistic approximations of the volume conductor. While the use of simplified volume conductors offers the advantage that inverse calculations do not need to account *explicitly* for the effect of *volume currents*, the BEM modeling implies (1) the availability of *free-hand* ultrasound systems to collect fetal–maternal anatomical information, (2) additional experimental time for ultrasound recordings and (3) an increased computational burden. Furthermore, BEM modeling requires the 3D segmentation of the compartments with different electrical conductivity from ultrasound images. In this study, we used a standardized approach for modeling the different volume conductor compartments, which is robust to inherent inter-individual variations in ultrasound image quality, but it requires manual definition of several fiduciary points and local manual correction of the AS boundaries. A fully automatic segmentation of the different compartments of the volume conductor remains contingent to additional development of the image-processing techniques. Our preliminary results obtained for real fMCG data in mid-gestation show promise, but additional studies are necessary to address the sensitivity of the source estimators to slight variations in the geometry of the individual volume conductor compartments,

within the range of errors that are inherent to the proposed methodology. Definitive answers regarding the sensitivity and specificity of such an approach for the detection of hypertrophy based on the cardiac vector strength await also further studies in fetuses with cardiac hypertrophy confirmed by *m*-mode cardiac ultrasound examination.

CHAPTER 6 CARDIAC VECTOR ESTIMATION IN HEALTHY HUMAN FETUS USING MAGNETOCARDIOGRAPHY AND REALISTIC APPROXIMATIONS OF THE VOLUME CONDUCTOR

This chapter sought to characterize the developmental changes of three measures used to describe the morphology of the fetal cardiac vector: QRS peak-amplitude, QRS duration and QRS time-amplitude integral. To achieve this objective, we rely on a recently developed methodology for fetal cardiac vector estimation, using multichannel fetal magnetocardiographic (fMCG) recordings and realistic approximations of the volume conductors obtained from *free-hand* ultrasound imaging. Fetal magnetocardiographic recordings and 3D ultrasound images were obtained from 23 healthy, uncomplicated pregnancies for a total of 77 recordings performed at gestational ages between 22 weeks and 37 weeks. We report the developmental changes of the cardiac vector parameters with respect to gestational age and estimated fetal weight, as well as their dependence on the estimated ventricular mass derived from cardiac dimensions measured with M-mode ultrasound. The normative values can be used along with the cardiac time intervals reported by previous fMCG studies to assist future clinical studies investigating conditions that affect fetal cardiac function.

6.1. Introduction

In the last decade, fetal magnetocardiography (fMCG) has emerged as an

attractive non-invasive technique for *in-utero* assessment of cardiac function, allowing high resolution measurements of fetal cardiac electrophysiology from the second trimester of pregnancy to term (Comani *et al.* 2004, Horigome *et al.* 2000, Peters *et al.* 2001, Van Leeuwen *et al.* 2004a, van Leeuwen *et al.* 1999, Wakai *et al.* 2003). Previous fMCG studies investigated the cardiac time intervals in healthy fetuses and demonstrated an increase in the duration of P wave and QRS complex with gestational age (Stinstra *et al.* 2002a, Horigome *et al.* 2000, van Leeuwen *et al.* 2004c). These changes reflect in part the increase in cardiac muscle mass associated with fetal growth. Although the increase in cardiac size throughout development should be also associated with an increase in signal strength, this relationship is less straightforward to be determined because the recorded signal amplitude is influenced by physical factors unrelated to cardiac electrophysiology, arising from the lack of control on the fetuses position and orientation relative to the sensing system, and from the variable geometry of fetal and maternal tissue compartments surrounding the fetal heart (Stinstra and Peters 2002b). Only a few studies have attempted to minimize these confounds by using source reconstruction techniques, which estimate the strength of the *primary* current sources, *i.e.* the fetal cardiac currents (Horigome *et al.* 2001, van Leeuwen *et al.* 2004a). However, the reconstruction algorithms were applied in simplified experimental settings by considering either half-space or spherically symmetric volume conductors, with *minimal or no* anatomical information about the fetal-maternal conductor. Although these simplified models permit closed-form analytical solutions of the forward problem and do not require imaging of

the fetal-maternal unit, their restrictive assumptions may significantly affect the accuracy of the inverse biomagnetic solution (Tao *et al.* 2012b, Stinstra and Peters 2002).

In this study we use a recently developed approach for the estimation of fetal cardiac vectors which combines fMCG recordings and realistic approximations of the volume conductor obtained from individual 3D ultrasound images of the fetal-maternal anatomy (Tao *et al.* 2012b). Our main objective was to derive improved estimators of the cardiac vectors and to obtain normative values for three quantitative measures of the cardiac vector morphology, *i.e.* the QRS peak-amplitude, QRS duration, and time-amplitude integral. Using recordings from 23 healthy pregnancies, we report herein the dependence of these parameters on gestational age and estimated fetal weight, as well as with respect to estimates of ventricular mass obtained from m-mode measurements of ventricular dimensions, from the end of the second trimester of pregnancy to birth.

6.2. Methods

6.2.1. Subjects and data acquisition

The data collection was part of a longitudinal study of fetal cardiac function using multichannel magnetocardiographic recordings. Twenty-three healthy pregnant women underwent a series of three to four visits from 22 to 36 weeks of gestation, for a total of 77 recordings. Among them, 17, 22, 21 and 17 recordings were performed at gestational ages in the ranges of 22-26, 26-30, 30-34 and 34-37 weeks of gestation,

respectively. The study protocol was approved by the Human Subjects Committee of the Kansas University Medical Center. Informed consent was obtained from all participant mothers in the study.

The biomagnetic signals were recorded with an 83-channel fetal biomagnetometer (CTF Systems Inc., subsidiary of VSM MedTech Ltd.), housed in a magnetically shielded room. Pregnant women were asked to rest in a comfortable supine position during the fMCG recordings on a reclining pneumatic chair, which can be moved horizontally and vertically for optimal positioning under the cryostat. The spatial distribution of the axial gradiometer sensors with a 5 cm baseline ensures a full coverage of the maternal abdomen, with the cryostat being placed above the upper abdominal surface. For each subject, a continuous 4 minute recording (1200 Hz sampling rate and 0.5-200 Hz pass band filter) was acquired.

Ultrasound examinations were performed immediately prior to or immediately after the fMCG recording using a GE Logiq-P5 ultrasound system interfaced with a 4C 1.4-4.8 MHz wide band convex transducer. The objective of the ultrasound examination was threefold: to acquire 3D images of the fetal-maternal anatomical compartments that allow building realistic approximations of the volume conductors; to perform standard biometric measurements of the fetus to estimate the fetal weight; and to obtain morphometric measurements of the fetal heart. To derive individual approximations of the volume conductors, we used the so-called *free-hand* 3D ultrasound, in which a 3D digitizer attached to the ultrasound probe records the positions and orientations of the probe for subsequent co-registration and

reconstruction of the volumetric data. For this task, we used the Stradwin 3D Ultrasound Acquisition and Visualization software (Cambridge University, UK) and a TrakSTAR positioning digitizer system (Ascension Technology Corp., USA) attached to the ultrasound probe. The calibration of the probe-digitizer system was performed with an ultrasound phantom. For each subject, series of B-scan images were recorded by scanning the maternal abdominal surface from side to side and from the upper to lower abdomen for a total number of 5000 to 6000 frames per subject. Co-registration of the ultrasound images with the fMCG sensor array was accomplished using three fiducial markers placed at non-collinear locations on the maternal abdomen (right side, left side, and sternum). The center of the ultrasound probe was placed at the location of each marker, and the corresponding frames were recorded in Stradwin. These frames were later used to identify the marker locations on the volumetric image, but were excluded from subsequent processing. The marker positions relative to the fMCG sensors were determined in the biomagnetometer by localizing three coils placed at those locations.

Standard biometric measurements (*femur length*, *abdominal circumference* and *head circumference*) were performed using the features built into the GE Logiq-P5 ultrasound system. These measurements were used for subsequent estimation of the fetal weight using the Hadlock formula (Hadlock *et al.* 1984). During the same session, measurements of heart dimensions were also performed by a pediatric cardiologist using M-mode images (figure 6.1). For this task, a four-chamber image of the fetal heart was acquired and the M-mode cursor was positioned perpendicular to

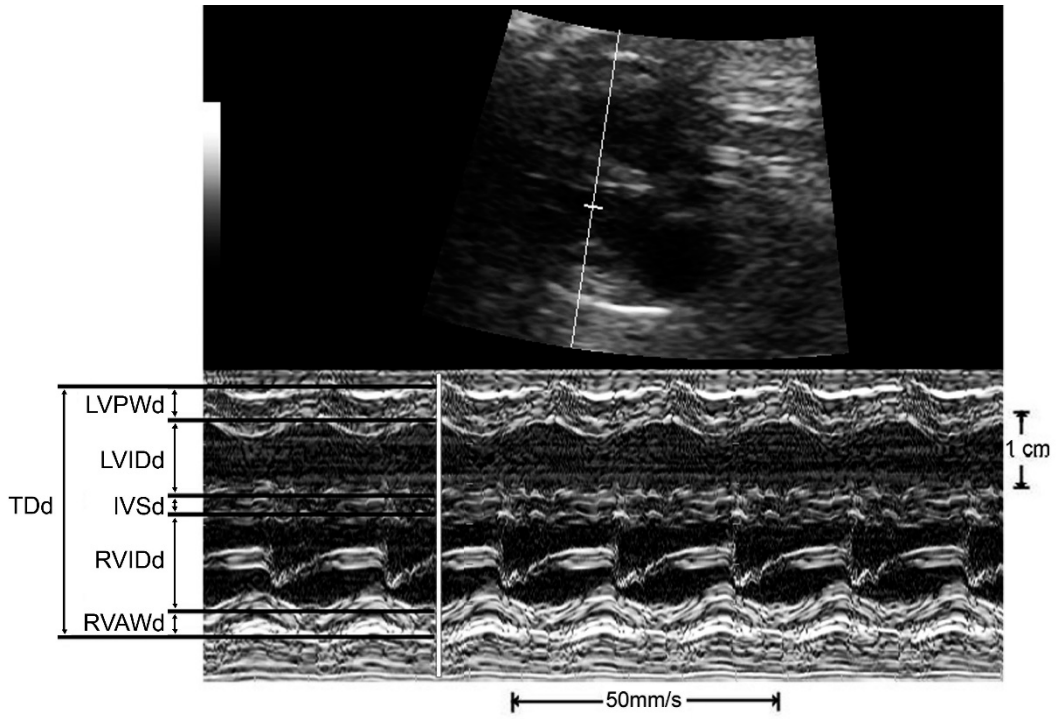

Figure 6.1 Exemplification of M-mode measurements performed in a fetus at 29 weeks, 2 days. The solid vertical white line marks the time of the diastole. The measured cardiac dimensions are shown on the left. LVPWd: left ventricular posterior wall dimension in diastole; LVIDd: left ventricular internal dimension in diastole; IVSd: interventricular septal thickness at diastole; RVIDd: right ventricular internal dimension in diastole; RVAWd: right ventricular anterior wall dimension in diastole; TDd: the transverse heart diameter in diastole.

the intra-ventricular septum under the atrio-ventricular valves, recording and storing a total of 6 to 8 cardiac cycles. The intra-ventricular septum thickness (IVSd), left ventricular chamber size (LVEDd) and left ventricular free wall thickness (LVPWd) were measured at end-diastole using the standard M-mode border measurement convention. The transverse heart diameter (TDd) was also measured from the anterior wall outer edge to the posterior wall outer edge at the maximum internal dimension of the ventricular endocardium. Satisfactory M-mode measurements were achieved only in 78% of the scans (60 cases). The unsuccessful M-mode screening in the remaining

cases was due to suboptimal fetus position or image quality, which prevented the acquisition of the 4-chamber view and/or positioning of the ultrasound beam perpendicular to the interventricular septum and ventricular walls. It must be noted that an unsuccessful M-mode screening in some subjects/gestational ages has reduced the number of recordings that could be used to assess the relationship between fMCG metrics and the ventricular dimensions, but did not prevent using the corresponding fMCG data to characterize the relationship with gestational age and estimated fetal weight, since the standard biometric measurements (*femur length*, *abdominal circumference* and *head circumference*) used for this analysis were available in all cases.

6.2.2. fMCG data pre-processing

The fMCG signals were filtered using the Independent Component Analysis (ICA) Infomax algorithm in EEGLAB (Delorme and Makeig 2004). ICA has been applied previously in multichannel fetal magnetographic studies to extract and characterize contributions from spatially distinct electrophysiological sources (*e.g.* (de Araujo *et al.* 2005, Mantini *et al.* 2006, Popescu *et al.* 2007). When ICA is used for filtering purposes, the signal of interest is reconstructed in the sensors from a subset of independent components, *i.e.* after removing the components that show clearly identifiable temporal patterns corresponding to other sources (*e.g.* maternal cardiac activity). We adopted this approach to minimize the risk of fetal cardiac signal loss. At the next processing step, the fetal QRS signals (R-peaks) were determined using

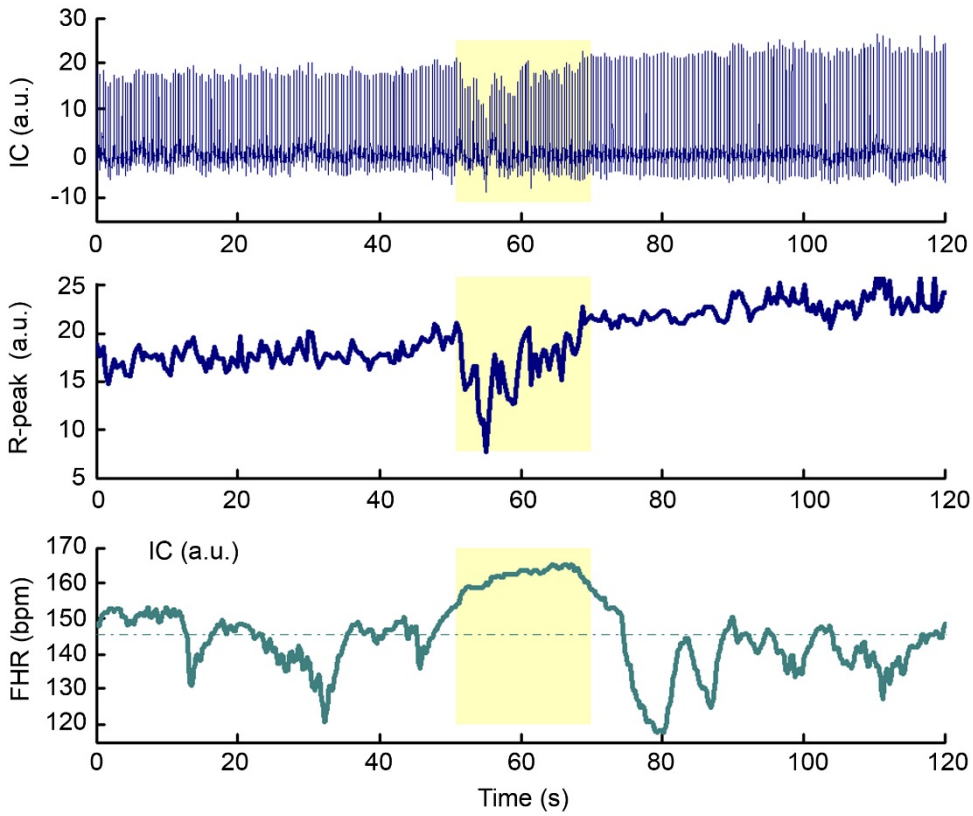

Figure 6.2 Identification of fetal movement using actocardiography. The exemplified fMCG signals were recorded in the third trimester of gestation (31 weeks and 2days). The upper trace shows a fetal cardiac independent component (IC), and the middle trace shows the R-peak amplitude trace. Signal variability due to fetal movement is noticed on the temporal segment shaded in yellow (around 60 sec) and is accompanied by fetal heart rate (FHR) acceleration (bottom trace).

a QRS detection algorithm relying on the cross-correlation of the signal with a manually selected QRS-template (Grimm *et al.* 2003). Given that the duration of the recording was constant, the number of averaged beats varied according to differences in heart rate (mean value=554, SD=47, pooled across all subjects and gestational ages analyzed for this study). The presence of gross fetal body movements during the fMCG recordings was ascertained using actocardiography (Zhao and Wakai 2002). Specifically, when visually identified R-peak amplitude variations across the

corresponding independent components were associated with significant increases in fetal heart rate and changes in QRS morphology on the temporal segments before and after movement, this was considered indicative of gross body movements (figure 6.2). Vigorous body movements may cause trunk rotation or shifting of the cardiac source with respect to the sensing system. Since this increase also the risk for less accurate volume conductor modeling, the corresponding datasets were excluded from further analysis. Other fetal movements (due to, e.g., slight limb movements without a change in overall position) that were reflected only in brief, transient QRS changes, led to the automatic exclusion of the corresponding segments of data (QRS complexes that were not passing the correlation threshold criterion). For all datasets with no indication of gross fetal body movements, the averaged fetal cardiac beat was estimated and used for the subsequent source reconstruction.

6.2.3. Ultrasound data analysis

We adopted a standardized approach to model the fetal body and amniotic sac (AS) compartments of the volume conductor (Tao *et al.* 2012). For each subject, we approximated the fetal body by merging an ellipsoid (fitted to the fetal trunk) and a sphere (fitted to the fetal head), determined from a set of fiduciary points and standard biometric measurements (head and abdominal circumferences). Similarly, we modeled the AS as an ellipsoid derived from a set of fiduciary points used to determine its long and short axes. This step was followed by an interactive local correction of the ellipsoid boundaries, as described in our previous report (Tao *et al.*

2012). The 3D ultrasound image volume was then re-sliced using fixed size planes oriented in the axial direction relative to the maternal abdomen. Re-sliced frames were saved along with the coordinates of the fiduciary points and were further processed in Matlab to determine the surface of the maternal abdomen. Following this, images were transformed to Analyze format (Biomedical Imaging Resource, Mayo Foundation) to allow for the segmentation and triangularization of the feto-maternal compartments performed with CURRY 5.0 (Compumedics Neuroscan). Triangularization of the boundary surfaces was done using average triangle sides of 5 mm, 10 mm, and 20 mm for the fetal body, AS and abdominal compartments, respectively. The source space was defined as a regular grid of points (3 mm spacing) inside the fetal trunk.

6.2.4. Source reconstruction

The gain matrix was computed using the boundary element method (BEM) with a linear-collocation approach (Mosher *et al.* 1999), which has been shown in previous feasibility studies to provide accurate solutions and efficient computational times (Tao *et al.* 2012). At early gestational ages (<28 weeks), we considered three-layer volume conductor models, with conductivities of 0.22, 1.4, and 0.05 S/m (Oostendorp *et al.* 1989, Stinstra and Peters 2002b) for compartments ascribed to the fetal body, amniotic fluid and surrounding tissues, respectively. For late gestational ages (>28 weeks), the source reconstruction results obtained with the three compartment model were contrasted against those obtained with a fourth compartment model, where a

fourth layer with uniform thickness (5 mm) and conductivity of $2x10^{-6}$ S/m was added using a 3-D dilation of the fetal body compartment to account for the potential presence of vernix (Tao et al, 2012). The model providing a better fit to the measured data was selected for each individual case, given also that a goodness-of-fit criterion was satisfied. This strategy was adopted to circumvent the lack of information about the presence and/or uniformity of the vernix. The implementation of the BEM in our study assumes nested volume conductor compartments; the existence of holes in the vernix that can affect the amplitude and distribution of the forward magnetic field (Stinstra and Peters 1998) is therefore expected to affect the goodness-of-fit for each of the two models tested. The quality of fit was evaluated by means of the explained data variance computed across all channels and over the whole QRS interval. The reconstruction results with explained data variance greater than 75% were considered to reflect a good fitting, whereas an explained variance between 50% and 75% was considered to reflect a moderate fitting. The data was discarded from the statistical analysis if the explained variance was lower than 50%.

The source reconstruction was performed using a recursive Multiple Signal Classification (MUSIC) algorithm (Mosher and Leahy 1998), which searches over the source space to find locations for which a linear combination of columns in the gain matrix projects onto the signal subspace, with a threshold subspace correlation set to 0.95. Once a dipole is identified, its gain is appended to a model matrix and the algorithm is repeated to search for another source. The rank of the signal subspace was selected by searching for a distinct drop in the magnitude of data matrix

eigenvalues. The recursions stopped when the number of dipoles found was equal to the signal subspace rank, or when no more sources satisfying the threshold subspace correlation could be found. The dipole magnitudes were estimated by multiplying the data matrix by the pseudo-inverse of dipole gains matrix. The vector magnitude was subsequently derived by a vector summation of all estimated dipoles.

6.2.5. Statistical analysis

The metrics used to characterize the vector magnitude (VM) morphology were the QRS peak amplitude or *peak vector magnitude* (pVM), QRS duration, and QRS *time-amplitude integral* (TAI). The QRS complex was delineated manually, with the onset and offset identified on the reconstructed QRS traces as the first/last point marking a significant deviation in signal slope from the PQ segment (for QRS onset) or ST segment (for QRS offset), respectively (the analyzer was not blinded to the results). The time-amplitude integral was determined as the area under the VM signal between the QRS onset and offset. A regression analysis (performed in *GraphPad Prism*) was used to characterize the relationship between each of these metrics and the gestational age, estimated fetal weight, and estimated total ventricular muscle mass, respectively. The total (left and right) ventricular muscle mass was estimated as:

$$TVM = \rho \cdot \left(V^{walls} + V^{IVS} \right) \qquad (6.1)$$

where ρ=1050 g/cm^3 is the myocardial density (Myerson *et al.* 2002), and V^{walls} and V^{IVS} are the volumes of the outer ventricular walls and intra-ventricular septum, respectively. The volume of the ventricular walls was approximated by the difference

between volumes of epicardial and endocardial shells, each approximated by prolate semi-ellipsoids with short (transverse axes) equal to TDd and TDd-2LVPWd, respectively:

$$V^{walls} = \frac{4}{3}\pi \cdot 0.5 \cdot \left[\frac{\alpha \cdot TDd^3}{4} - \frac{(TDd - 2LVPWd)^2(\alpha \cdot TDd - LVPWd)}{4} \right] \quad (6.2)$$

where the parameter α denotes the ratio of the outer ellipsoid long axis to its short axis and was considered α=0.75 based on the regression equations of the cardiac dimensions reported by Firpo *et al*. (Firpo *et al.* 2001). The symmetry of the adopted model is consistent with the fact that in the fetus the LV and RV face nearly the same systemic afterload, and, as a result, the thickness of the free ventricular walls is essentially the same and the LV to RV mass ratio is close to unity (Bhat *et al.* 2004, Firpo *et al.* 2001). The volume of the intra-ventricular septum was approximated from the cross-sectional area of the inner ellipsoid multiplied by the IVSd:

$$V^{IVS} = \pi \cdot 0.5 \cdot \left(\frac{TDd}{2} - LVPWd \right) \cdot (\alpha \cdot TDd - LVPWd) \cdot IVSd \quad . \quad (5.3)$$

Two statistical models were tested for each cardiac vector metric, *i.e.* the commonly used linear regression model and a nonlinear power growth model. We tested the power model based on previous observations relating heart dipole moments to heart and body weight in animal studies (Nelson *et al.* 1975). Outliers were automatically identified and excluded in the fitting process using the ROUT method available in the GraphPad Prism (Motulsky and Brown, 2006). The model with the best goodness of fit was selected in each case based on the coefficient of determination. Mean values and standard deviation of the cardiac vector metrics were also estimated separately for gestational ages of 24, 28, 32, and 36 weeks, by grouping the sample data into 4

week-wide bins centered around these targeted gestational ages, and adjusting for gestational age using the corresponding regression equation.

6.3. Results

Out of the 77 total recordings, 12 recordings were discarded due to gross fetal body movements identified using actocardiography, and 1 recording needed to be excluded due to a co-registration problem. The retention rate was 76%, 86%, 81% and 88% for gestational age ranges of 22-26, 26-30, 30-34 and 34-37 weeks, respectively. Figure 6.3 exemplifies the reconstructed cardiac vector magnitude for the same subject at three gestational ages. The amplitude of the averaged QRS observed in the sensor signals exhibits significant variation across measurements at different gestational ages, which is associated to changes in the fetus positioning and source-to-sensors configuration. As a consequence of these changes, there is no obvious increase in the QRS peak-amplitude in the sensor-signals with gestational age. On the other hand, the reconstructed cardiac vector magnitude shows the expected increase in peak-amplitude, thus confirming that the source reconstruction can reduce the confounding effects introduced by a different positioning of the fetus relative to the sensors when measurements are repeated throughout gestation.

Out of the 64 recordings that were analyzed using the source reconstruction procedure, 14 datasets were characterized by a poor fitting (explained data variance lower than 50%) and were excluded from the regression analysis. Out of the 50 remaining cases, good fitting (> 75 % explained data variance) was obtained in 41

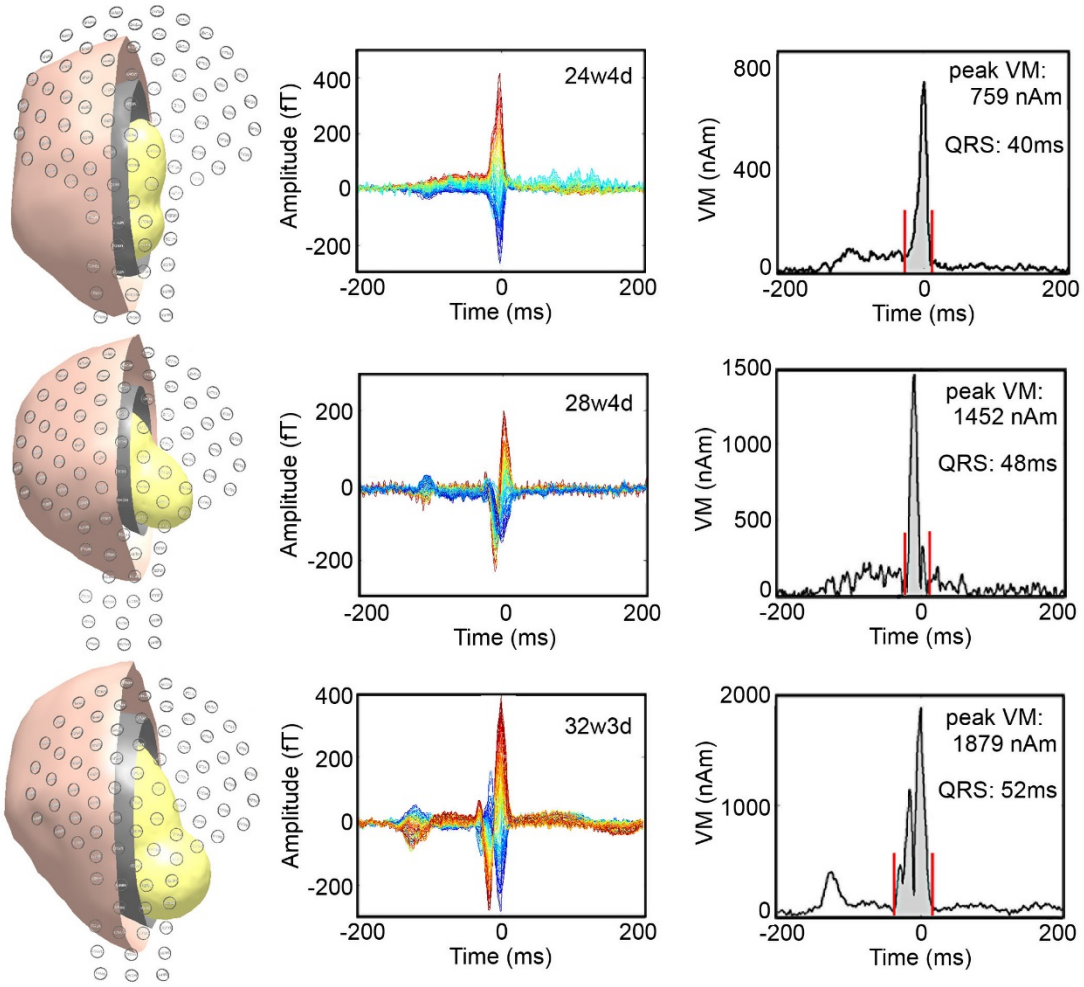

Figure 6.3 Exemplification of reconstructed cardiac vectors from fMCG recordings performed in the same subject at three gestational ages. Panels on the left show the volume conductor co-registered with the sensor array. The fetus was in cephalic presentation at 24 and 32 weeks and in a breech presentation at 28 weeks. The middle panels show the averaged fMCG data, and the right panels show the corresponding reconstructed vector magnitude (VM). The area under the QRS is shaded in gray.

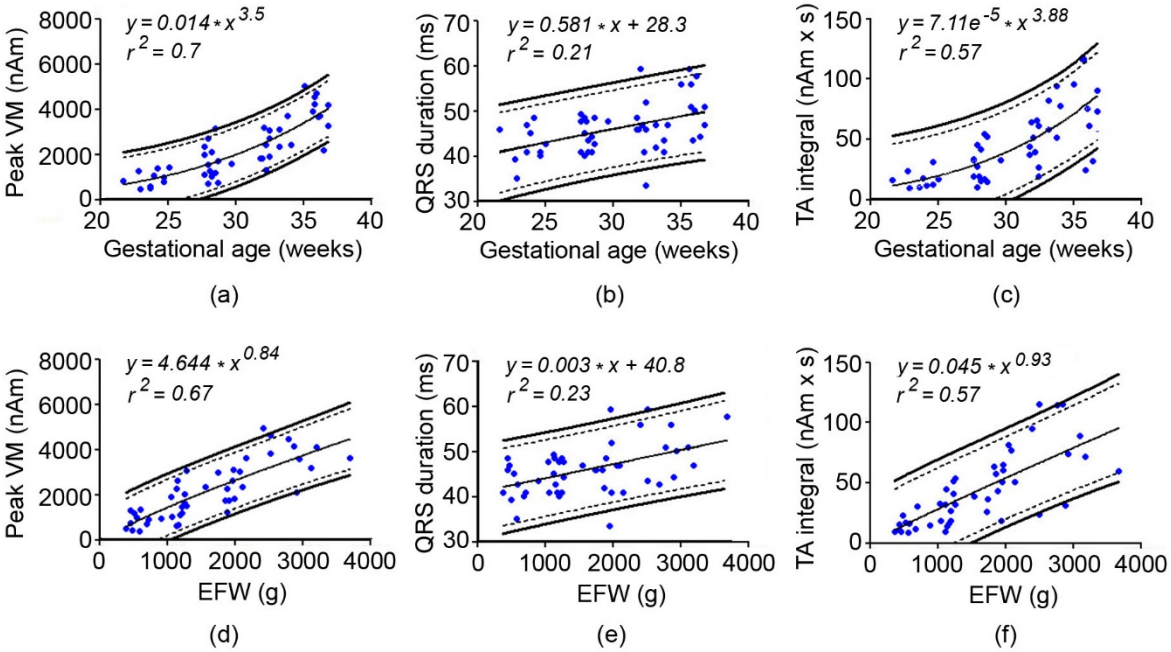

Figure 6.4 Developmental changes of the peak vector magnitude (VM, panels a, d), QRS duration (b, e) and time-amplitude (TA) integral (c, f,) are shown with respect to gestational age (upper panels) and the estimated fetal weight (EFW, lower panels). All scatter plots show the line of regression, and the 90% (dotted lines) and 95% (continuous lines) prediction intervals.

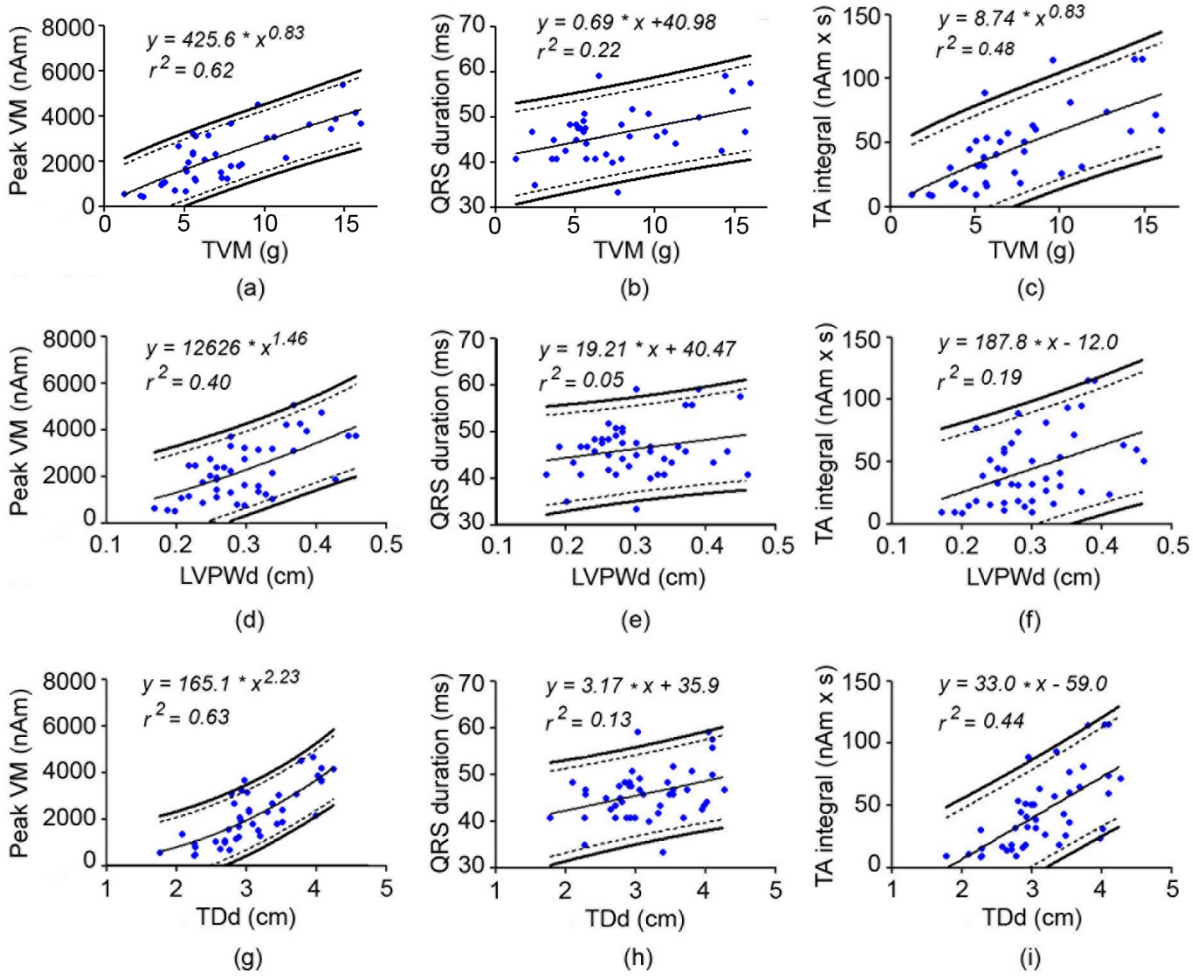

Figure 6.5 Developmental changes of the peak vector magnitude (a, d, j), QRS duration (b, e, h), and time-amplitude integral (c, f, i) are shown with respect to the total ventricular mass (TVM), left ventricular posterior wall thickness (LVPWd), and heart transverse diameter (TDd), respectively. All scatter plots show the line of regression, and the 90% (dotted lines) and 95% (continuous lines) prediction intervals.

Table 6.1 Mean values of the fetal cardiac vector parameters adjusted for gestational age. Results were obtained using the reconstructed cardiac vectors with good or moderate fitting were (50 out of 77 cases).

GA(weeks)	*n*	Peak VM (nAm)	QRS duration (ms)	TA integral (nAm s)
24	10	941.65 ± 331.38	43.58 ± 4.61	15.88 ± 7.29
28	14	1588.43 ± 745.78	44.61 ± 3.32	28.34 ± 14.25
32	15	2190.69 ± 607.35*	45.13 ± 6.01	50.50 ± 19.81
36	11	3840.21 ± 937.45*	50.58 ± 6.1	76.68 ± 34.71

** indicates one outlier was excluded from the corresponding data sets*

Table 6.2 Mean values of the morphometric fetal cardiac measurements adjusted for gestational age. Results were obtained using data from all available M-mode measurements (60 out of 77 cases).

GA(weeks)	*n*	TDd (cm)	TVM (g)	IVSd (cm)	LVPWd (cm)
24	11	2.29 ± 0.28	2.87 ± 0.82	0.23 ± 0.054	0.24 ± 0.0543
28	17	2.85 ± 0.19	5.21 ± 0.98	0.28 ± 0.046	0.28 ± 0.0391
32	17	3.28 ± 0.25	7.57 ± 1.43	0.33 ± 0.056	0.31 ± 0.0685
36	15	3.91 ± 0.39	12.54 ± 3.49	0.38 ± 0.071	0.35 ± 0.0629

cases, and moderately good fitting (between 50 % to 75 % explained data variance) was obtained in 9 cases. Figure 6.4 shows the results of the regression analysis for the three cardiac vector metrics with respect to the gestational age and estimated fetal weight. The mean values of the cardiac vector metrics and cardiac dimensions measured in our study and adjusted for gestational age are summarized in Tables 6.1 and 6.2, respectively. The ventricular dimensions obtained from m-mode measurements (Table 6.2) were in the range reported by other prenatal echocardiography studies (*e.g.* Tan et al., 1992; Firpo *et al.*, 2001). The 3-compartment model was more appropriate in 79% of the recordings performed after 28 weeks of gestation, while the 4-compartment model (including an uniform layer of vernix) was more appropriate only in the remaining 21%. No trend has been observed when comparing the goodness of fit for the 3- and 4-compartment models separately for gestational ages between 28 and 32 weeks and 32 to 36 weeks. Since the presence and uniformity of the vernix throughout gestation cannot be predicted on an individual basis, the model providing a better goodness-of-fit was selected on a case-by-case basis as previously explained. Support for such an empirical approach comes also from previous studies investigating the vernix presence and distribution in large numbers of subjects (Visscher *et al.* 2005), which point out to a bimodal distribution, with most fetuses having a surface coverage of less than 10% or greater than 90% in late gestation.

Figure 6.5 (upper row of panels) illustrates the scatter plots of the three cardiac vector metrics versus the total ventricular mass. The normal growth of the fetal heart

assessed from M-mode measurements is associated with an increase in the peak-vector magnitude, with the exponent of the regression equation being close to the one characterizing the relationship between the peak vector magnitude and the estimated fetal weight. This allows to estimate a ratio of ventricles mass to body weight of about 0.45%, which is in line with the general observation that the total heart weight is about 0.6% of the body weight in mammals. The changes in the cardiac vector metrics are also shown in figure 6.5 with respect to the LVPWd and TDd. These normative data may sub-serve future studies using the reconstructed cardiac vector to investigate pathologic conditions, and are free of the geometric assumptions used in the estimation of the ventricular mass.

6.4. Discussion

The longitudinal study of 23 healthy pregnancies reveals a positive correlation of the amplitude and duration of the fetal cardiac vector magnitude with gestational age and estimated fetal weight from 22 to 37 weeks of gestation. The relationship between the peak-VM values obtained from fMCG and the estimated fetal weight resembles the one predicted analytically by studies in vertebrate animals (Nelson *et al.* 1975), which indicated a power growth model of the form $y = 3.43 \cdot x^{0.826}$. The exponent parameter of both models are in good agreement, yet the multiplicative constant (scaling factor) estimated in our study is higher (*i.e. 4.64* vs. *3.43*). This discrepancy can be partly due to the modeling approximations made by each study, including the assumed (default) electrical conductivity values of the volume conductor

compartments. On the other hand, the peak-VM values obtained in our study are significantly higher compared to those reported by previous fMCG studies using simplified (spherical or half-space) volume conductor models (Horigome *et al.* 2001, van Leeuwen *et al.* 2004a). This confirms previous findings from simulation studies, which indicated that the simplified volume conductors may lead to underestimation of the VM (Tao *et al.*, 2012).

The mean QRS duration measured on the reconstructed cardiac vectors in our study shows an increase from 43.6 ms at 24 weeks to 50.5 ms at 36 weeks of gestation. These values are in the range reported by previous studies (Stinstra *et al.* 2002b), which used measurements of cardiac time intervals performed directly on the sensor signals. The increase in QRS duration with gestational age and fetal weight is consistent with the increase in ventricular mass; however, the *rate* of increase in QRS duration is significantly less than the rate of increase in ventricular mass. Furthermore, when compared to the cardiac vector strength, the corresponding r^2 values indicate that a relatively smaller variability in QRS duration is explained by fetal age, estimated fetal weight or ventricular mass. While these findings agree with observations from previous reports (*e.g.* Stinstra *et al.* 2002a), we cannot rule out that that the signal processing (involving template matching and averaging) may lead to some distortion of the QRS due to physiological beat-to-beat variability or trigger jitter (Schneider *et al*, 2001), which results in a smoothing effect following averaging.

In our study, we considered that the presence of vernix caseosa can affect the distribution of the magnetic field after 28 weeks of gestation. To address this aspect,

we compared the 3-compartment model against the 4-compartment model and we found a significantly lower success rate of the 4-compartment model across subjects. This can be partly due to the fact that the non-uniform coverage or the presence of holes in the vernix may considerably affect the accuracy of the 4-layer model with nested compartments, as indicated by previous simulation studies (Stinstra and Peters 2002b). A second objective of our study was to determine the success rate of the proposed methodology in providing good estimators of the cardiac vectors. The gross fetal body movement was found to be one factor that affects the success rate of the fMCG analysis. Using actocardiographic criteria, vigorous fetal body movements were observed in ~17% of the recordings. Real time ultrasound studies had reported that fetuses at early gestation tend to have more frequent transient body movements (Nasellopaterson *et al.* 1988). The fMCG recording time in our study was much shorter compared to the ultrasound study, and this may explain why we observed only a slight increase of the *overall* incidence of fetal body movement around 24 weeks of gestation. Another aspect that affects the overall success rate of the methodology arises from the fact that among the recordings with no evidence of fetal movement, ~21% did not provide appropriate goodness-of-fit according to the criteria used in our study. A low goodness of fit may arise from different factors, ranging from geometrical and electrical conductivity approximations used in our approach to the fact that gross body movements were possible in some cases during the time interval when the fetus could not be monitored, *i.e.* between the fMCG recordings and the ultrasound recording. Together with data affected by fetal body movements, this leads

to an overall attrition rate of ~34%, which is acknowledged as a limitation of the methodology.

The normal range of the cardiac vector metrics reported in our study can assist future studies aiming to characterize the sensitivity of fMCG for indentifying electrophysiological markers of fetal cardiac hypertrophy *in-utero*. Since the cardiac vector magnitude depends on the myocardial mass, we posit that fetuses with cardiac hypertrophy may show abnormalities of the cardiac vector parameters. The peak vector magnitude and QRS integral appear more suited for such applications, since they exhibit a more significant dependency on the myocardial mass compared to the QRS duration. The increased risk for fetal cardiac hypertrophy is associated with a broad range of conditions, such as intra-uterine growth retardation, pulmonary valve and aortic stenosis, closure of the ductus arteriosus, tetralogy of Fallot, or maternal diabetes. The ultrasonographic fetal heart monitoring is the standard method in clinical settings, but additional investigational techniques, such as fMCG, may prove to have diagnostic value in cases of inadequate imaging due to factors like maternal obesity and/or suboptimal fetal positioning. For example, maternal obesity which does not impact fMCG recordings ((Peters *et al.* 2001) can prevent a complete fetal cardiac ultrasound imaging in nearly one third of diabetic pregnant women (Sekhavat *et al.* 2010), whereas diabetes mellitus is at the same time associated with a high incidence of fetal cardiac hypertrophy (Rizzo *et al.* 1992, Veille *et al.* 1992, Gandhi *et al.* 1995b). The methods used in our study rely on several approximations of the volume conductor and require additional investigations to characterize the sensitivity

and specificity of the fMCG source estimators for the detection of cardiac hypertrophy. Due to the necessity of a simultaneous successful estimation of the cardiac vector parameters and confirmation of cardiac hypertrophy from echocardiographic examinations, a relatively high demand must be placed in such investigations on the number of enrolled subjects, as our findings show that this requirement may be only fulfilled in approximately half of the recordings.

CHAPTER 7 CARDIAC VECTORS ESTIMATED BY MAGNETOCARDIOGRAPHY AND REALISTIC APPROXIMATIONS OF THE VOLUME CONDUCTOR IN FETUSES OF DIABETIC MOTHERS: COMPARISON TO HEALTHY FETUSES

Our previous study has reported the developmental changes of cardiac vectors in 23 uncomplicated pregnancies which rely on a standardized methodology for fetal cardiac vector estimation. The current study uses the same methodology to analyze developmental changes of fetal cardiac vector metrics, i.e. QRS peak-amplitude, duration and time-amplitude integral, measured on the reconstructed cardiac vectors, for fetuses of diabetic mothers (FODM). Fetal magnetocardiographic (fMCG) recordings and realistic approximations of the volume conductors were obtained for seven FODM between 23 weeks and 36 weeks. We compared the cardiac vector metrics as well as cardiac dimensions (transverse heart diameter, left ventricular free wall thickness, and the intra-ventricular septum thickness) measured with m-mode ultrasound of FODM to the data of measured previously from control subjects. The results show promise of applying the techniques to clinical settings in that estimated cardiac vector parameters show progressively higher values with gestational age for the FODM group relative to the control group. We observed also that the results exhibit a significant variance across subjects, especially in late gestation. Additional studies that include measures of maternal hyperglycemia and hyperinsulinemia are necessary to fully characterize the sensitivity of the source estimators for detection of

fetal cardiac hypertrophy on diabetic pregnancies.

7.1. Introduction

Pregestational and gestational diabetes mellitus affect an average of 1.3% and 7.6% of all pregnancies, respectively (Corrigan *et al.* 2009), which could together result in around 3% FODM with congenital cardiac diseases (MeyerWittkopf *et al.* 1996). In particular, fetal cardiac hypertrophy characterized by thickened intraventricular septum or ventricular free walls appeared to have the highest occurrence. Early studies have indentified the dependence of fetal cardiac hypertrophy on maternal hyperglycemia and hyperinsulinemia. Strict maternal metabolic control may delay this process but cannot eliminate it (Cooper *et al.* 1992). Thus, the early detection of fetal hypertrophic symptoms is critical for monitoring or prompt interventions, which can reduce the risks of congestive heart failure and postnatal complications.

Fetal magnetocardiography (fMCG) has emerged as an attractive technique for *in-utero* assessment of the fetal cardiac *electrophysiology*. fMCG was shown to provide high quality recordings despite maternal obesity, which can be an issue for diabetic mothers during ultrasound screening (Comani *et al.* 2004). Several studies have demonstrated unique advantages of fMCG in characterizing fetal arrhythmias in obese patients in terms of cardiac wave morphology or QRS complex duration, where conventional ultrasound-based methods can fail (Comani *et al.* 2004, Leeuwen *et al.* 2000). Recently, a few fMCG studies attempted to model the fetal heart as a *primary current source (i.e.* the fetal cardiac currents) and investigate the correlation between the fetal hypertrophic condition with the strength of the current source (Horigome *et*

al. 2001, Van Leeuwen *et al.* 2004a). This method has the advantage of minimizing cofounding effects arising from the lack of control on the fetuses' position and orientation relative to the sensing system, and from the variable geometry of fetal and maternal tissue compartments surrounding the fetal heart (Stinstra *et al.* 2002a), thus providing more accurate estimation of the fetal heart electrophysiology.

Our previous studies have improved this method by modeling the fetal cardiac current in a realistic approximation of volume conductor and using also a multiple cardiac current sources model (Tao *et al.* 2012a). We applied the developed standardized methodology to 23 healthy pregnancies and we established the normative date base in terms of cardiac vector metrics (i.e. QRS peak-amplitude, duration and time-amplitude integral) and cardiac dimensions (transverse heart diameter, left ventricular free wall thickness, and the intra-ventricular septum thickness). In this study, we analyzed the cardiac vector metrics as well as cardiac dimensions of seven FODM using the same methodology. We then compared the data obtained from FODM against the control data obtained in one of our study published previously. The hypertrophic subjects identified by cardiac vector metrics will be characterized by the cardiac dimension measurements. The aim of this study is to provide a preliminary investigation of the usefulness of fMCG in characterizing fetal hypertrophy for FODM as early as 23 weeks of gestation.

7.2. Methods

The data collection was part of a longitudinal study of fetal cardiac function using

multichannel magnetocardiographic recordings. Eight diabetic pregnant women underwent a series of three to four visits from 23 to 36 weeks of gestation, for a total of 30 recordings. Among them, 27 recordings were successfully performed (data from 3 recordings were discarded because of co-registration errors between fMCG sensors and ultrasound recordings). In these 27 recordings, 5, 8, 7 and 7 recordings were performed at gestational ages in the ranges of 22-26, 26-30, 30-34 and 34-37 weeks of gestation, respectively. The study protocol was approved by the Human Subjects Committee of the Kansas University Medical Center. Informed consent was obtained from all participant mothers in the study.

We applied the same methodology described in chapter five to diabetic subjects. fMCG signal recordings was collected using an 83-channel fetal biomagnetometer (CTF Systems Inc., subsidiary of VSM MedTech Ltd.) immediately before or after ultrasound screening. For each subject, series of B-scan images were recorded for a total number of 5000 to 7000 frames per subject. The number of frames is slightly larger for diabetic subjects relative to the control group since maternal diabetes is often associated with obesity and the fetuses are larger in size. Standard ultrasound measurements (IVSd, LVEDd, LVPWd, and TDd) were collected at different gestational ages. Satisfactory M-mode measurements were achieved only in 83% of the scans (25 cases). The same cardiac vector metrics as in chapter five (peak amplitude, QRS duration, and QRS time-amplitude integral) were used for characterizing the VM morphology for diabetic subjects. The dependency between each metric and the measured cardiac dimensions (IVSd, LVPWd, TDd) was assessed

using regression analysis.

7.3. Results

Figure 7.1 shows the difference of developmental changes between FODM (fetus of diabetic mothers) and the control group. Out of 30 FODM recordings, 3 cases are not included in the statistical analysis due to co-registration errors between fMCG sensors setting and ultrasound recordings. Among the remaining cases, a good volume conductor fitting was obtained in 8 cases, moderate fitting in 14 cases and low-quality fitting in 5 cases. Peak vector magnitude and time amplitude integral of the two groups didn't show significant differences in early gestation (< 28wks). However, the differences became significant with the increase in gestational age, particularly around the age of 36 weeks. As shown in table 6.1, the observed adjusted mean peak vector magnitude and adjusted mean time amplitude integral of FODM can be twice higher than for the control subjects. The observed results are consistent with previous studies showing that the hearts of fetuses of diabetic mothers have a significantly larger cardiac size than that of a group of normally grown fetuses (Veille et al. 1993). On the other side, the mean QRS duration of FODM is constantly higher than the control subjects, which can indicate a decreased left ventricular systolic function for FODM (Murkofsky et al. 1998) from early gestation. The observation of decreased left ventricular function is consistent with the higher measurements of left ventricular posterior wall diameter (LVPWd) which is shown in figure 7.2.

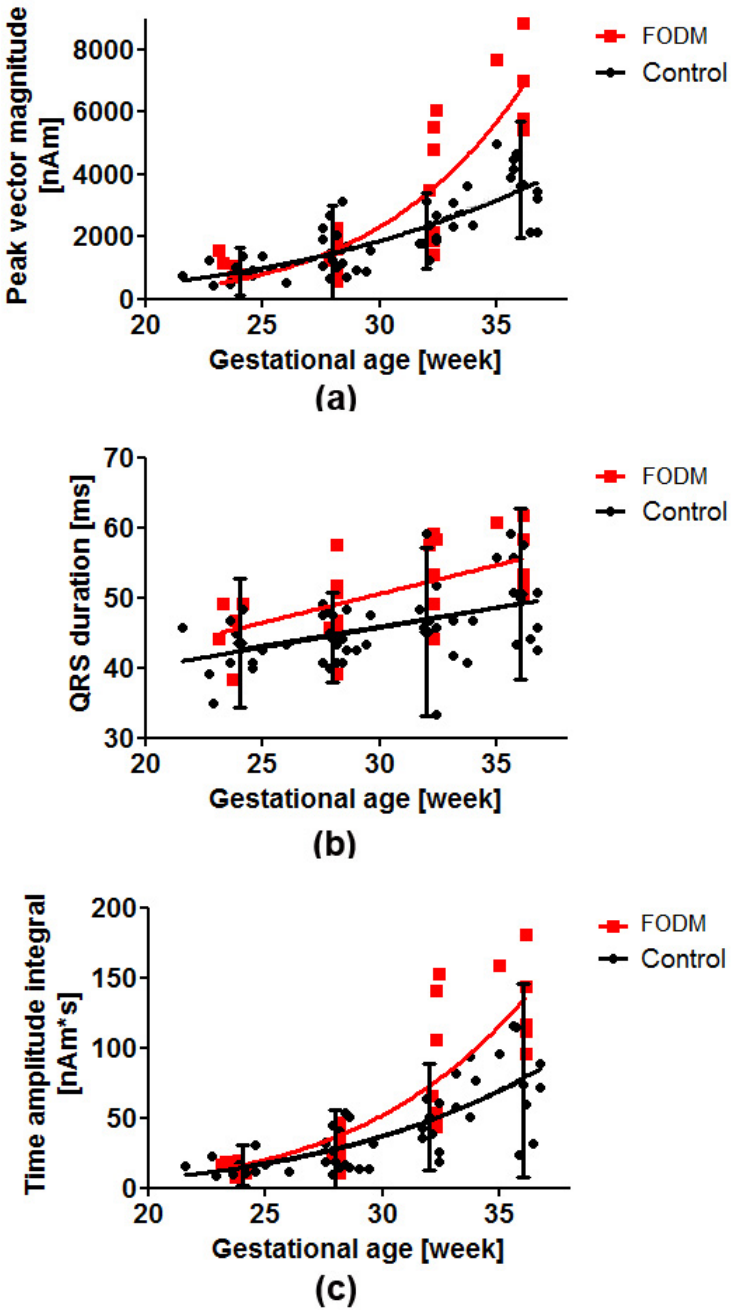

Figure 7.1 Dependence of the peak vector magnitude, QRS duration, and time-amplitude integral on the gestational age.

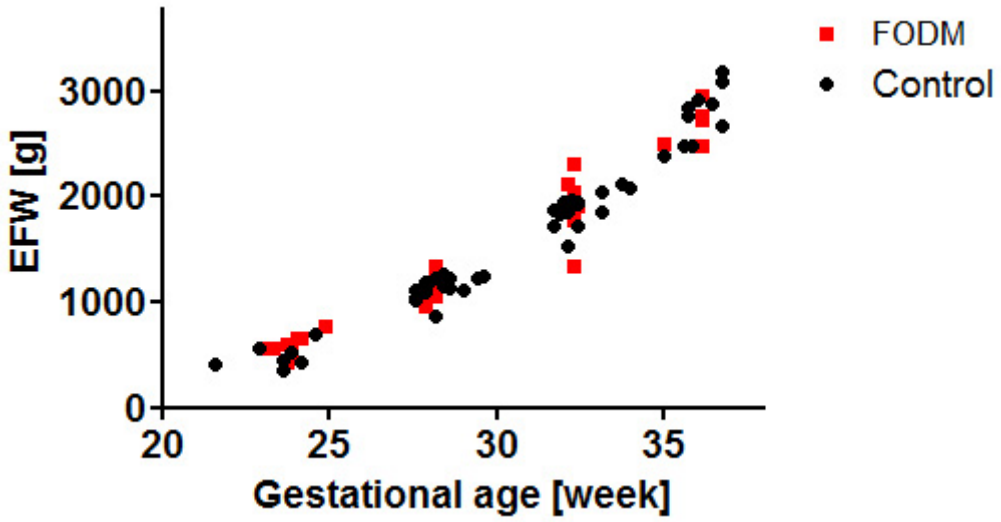

Figure 7.2 Estimated fetal weight for Control (black) and FODM group (red) from 23 to 36 weeks of gestation.

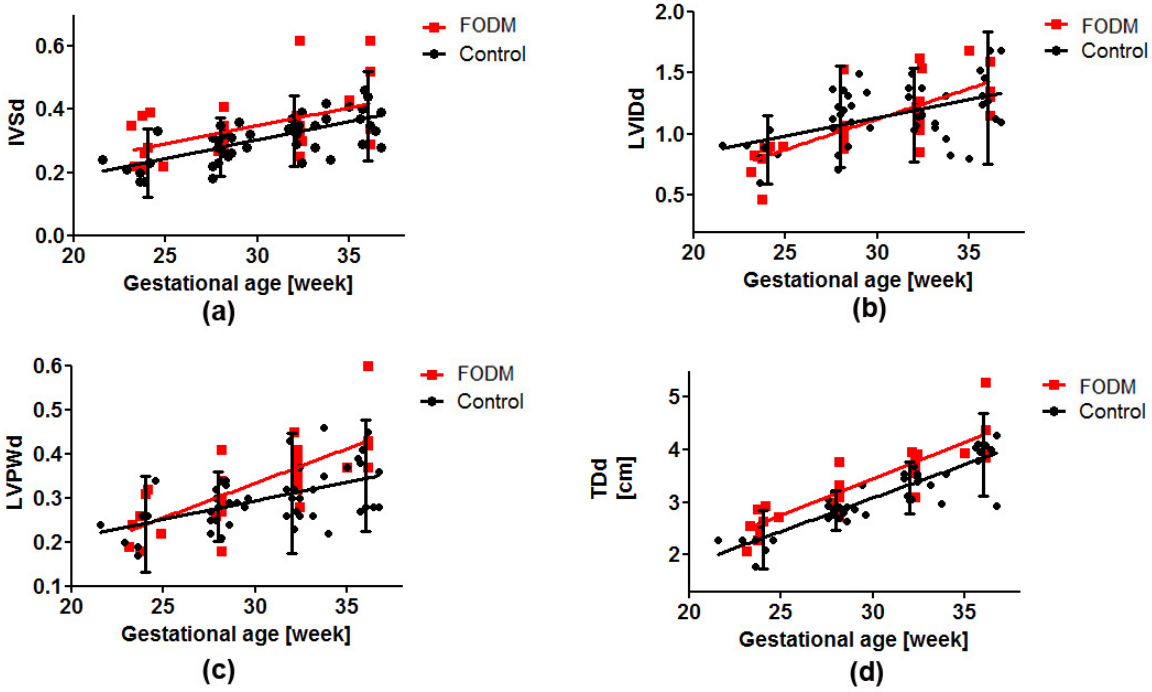

Figure 7.3 Developmental changes of M-mode measurements of control (black) and FODM (red) group, following linear regression.

Consistent with the observations of cardiac vector magnitude and QRS duration, IVSd and TDd in FODM group were constantly higher than in the control group. Increased IVSd and TDd ultrasound measurements indicate increased cardiac size and this

phenomenon was also observed by (Veille *et al.* 1992). LVPWd for FODM was similar to control fetuses in early gestation. In late gestation, LVPWd for FODM is still higher than the normal fetus but the condition was not as severe, while LVIDd were not significantly different between the two groups.

The estimated fetal weight and femur length between FODM and control fetuses (figure 6.3) are similar across all periods of gestation. Therefore, nutrition condition and growth retardation cannot explain the difference in cardiac vector metric and cardiac diameter measurements between FODM and normal fetuses.

Table.7.1 Mean values of the estimated cardiac metrics and cardiac dimensions adjusted for control and diabetic group

Variable	GA (weeks)	mean ± SD	
		Control	FODM
Peak vector magnitude (nAm)	24	877.80 ± 379.05	1117.05 ± 397.25
	28	1470.94 ± 765.27	1220.21 ± 622.56
	32	2190.63 ± 607.35	3433.91 ± 1847.07
	36	3840.21 ± 937.45	6783.56 ± 1473.04
QRS duration (ms)	24	43.58 ± 4.61	45.58 ± 4.5
	28	44.31 ± 3.21	48.52 ± 5.43
	32	45.13 ± 6.01	52.91 ± 5.69
	36	50.58 ± 6.1	55.36 ± 4.88
Time-amplitude integral (nAm*s)	24	15.88 ± 7.29	16.05 ± 5.85
	28	25.93 ± 14.82	26.26 ±11.66
	32	50.52 ± 18.88	83.08 ± 45.61
	36	76.68 ± 34.71	131.89 ± 34.52
TDd (cm)	24	2.29 ± 0.28	2.58 ± 0.25
	28	2.85 ± 0.19	3.24 ± 0.35
	32	3.28 ± 0.25	3.68 ± 0.28
	36	3.91 ± 0.39	4.29 ± 0.58
IVSd (cm)	24	0.23 ± 0.054	0.29 ± 0.076
	28	0.28 ± 0.046	0.32 ± 0.046
	32	0.33 ± 0.056	0.36 ± 0.11
	36	0.38 ± 0.071	0.44 ± 0.13
LVPWd (cm)	24	0.24 ± 0.0543	0.25 ± 0.05
	28	0.28 ± 0.0391	0.29 ± 0.065
	32	0.31 ± 0.0685	0.36 ± 0.054
	36	0.35 ± 0.0629	0.44 ± 0.092

7.4. Discussion

Our previous studies proved a positive correlation of the amplitude and duration of the fetal cardiac vector magnitude with gestational age and estimated fetal weight for normal fetuses. We applied the same methodology to eight diabetic subjects and compare the results to the normal pregnancies. Our study reveals higher values of

reconstructed cardiac vector magnitude for fetuses of diabetic mothers (FODM) than the control group, especially at late gestation. According to our results, the onset of cardiac vector anomalies start as early as 23 weeks of gestation with a symptom of prolonged mean QRS duration (as shown in figure 6.1). This observation is complemented by higher M-mode measurements (IVSd and TDd in figure 6.2), which agrees with previous fetal echocardiographic investigations (Veille et al. 1993, Hornberger 2006, Sekhavat et al. 2010), indicating that that the onset of hypertrophy most likely occurs even before 20 weeks of gestation with documentation of increased ventricular septal thickening relative to fetuses of non-diabetic pregnancies.

Measurements of the reconstructed peak vector magnitude between the two groups were similar in early gestation, but a discrepancy becomes progressively larger from mid to late gestation, indicating an accelerated growth pattern of the fetal heart in the mid and third trimesters compared to fetuses of non-diabetic pregnancies, even when adjusted for fetal weight. During the first and second trimester, reconstructed peak-VMs for FODM group are similar to the ones obtained in the control group. One explanation for this is that in the in the first half of pregnancy, the fetus is exposed primarily to hyperglycemia, which, without secondary hyperinsulinemia, results in slowing of fetal growth (Creasy and Resnick 1999) including fetal heart development. During the second half of pregnancy, hypertrophic islet cells respond to hyperglycemia with an increase in insulin production. This potent combination of hyperinsulinemia, a major anabolic hormone, and hyperglycemia, a major anabolic fuel, results in a cascade of third-trimester events that culminate in a striking increase

in fat stores and a modest 12% increase in protein stores (Fee and Weil 1960). One consequence of accelerated fetal growth from middle to late gestation is the cardiomegaly which results in the elevation of cardiac peak VM, as shown in our studies.

CHAPTER 8 CONCLUSION AND DISCUSSION

The fMCG signal morphology is difficult to be interpreted accurately due to the uncertainties of fetal position and orientation relative to the sensing system. To circumvent this drawback, several previous studies proposed the estimation of the fetal cardiac vectors using simplified volume conductors models. The proposed study aims to evaluate an innovative methodology for the estimation of fetal cardiac signal strength from fMCG data using realistic volume conductor models.

To achieve this goal, we develop a standard methodology which takes advantage of a free hand 3D ultrasound system to obtain 3D ultrasound image volumes, and to build realistic approximations of the volume conductor. This method has been tested in simulation studies and shows better performance compared to the use of simplified volume conductor models.

We developed standard measurements to describe the morphology of the fetal cardiac vector: QRS peak-amplitude, QRS duration and QRS time-amplitude integral; and applied the described method on a group of 23 healthy pregnant women to build a standard database for normal cardiac vector parameters. The same method was later tested on 7 diabetic mothers. The results on diabetic pregnant subjects show promise of applying the techniques to clinical settings, but additional studies in a larger population are necessary to characterize the sensitivity of the source estimators for detection of fetal cardiac hypertrophy.

REFERENCE

ACOG 1997 Acog committee opinion. New ultrasound output display standard. Number 180, november 1996. Committee on obstetric practice. American college of obstetricians and gynecologists *International journal of gynaecology and obstetrics: the official organ of the International Federation of Gynaecology and Obstetrics* **57** 227-8.

Alexander G R, Himes J H, Kaufman R B, Mor J and Kogan M 1998 A united states national reference for fetal growth *Obstet Gynecol* **87** 163-8.

Ang E S B C, Jr., Gluncic V, Duque A, Schafer M E and Rakic P 2006 Prenatal exposure to ultrasound waves impacts neuronal migration in mice *Proceedings of the National Academy of Sciences of the United States of America* **103** 12903-10.

Barratt D C, Penney G P, Chan C S, Slomczykowski M, Carter T J, Edwards P J and Hawkes D J 2006 Self-calibrating 3d-ultrasound-based bone registration for minimally invasive orthopedic surgery *Ieee Transactions on Medical Imaging* **25** 312-23.

Baule G and McFee R 1963 Detection of the magnetic field of the heart. *Am. Heart J* **66** 95-6.

Bell A and Sejnowsky T 1995 An information-maximization approach to blind separation and blind deconvolution *Neural Comput* 1129-59.

Berg S, Torp H, Martens D, Steen E, Samstad S, Hoivik I and Olstad B 1999 Dynamic three-dimensional freehand echocardiography using raw digital ultrasound data *Ultrasound in Medicine and Biology* **25** 745-53.

Bhat A H, Corbett V, Carpenter N, Liu N, Liu R L, Wu A, Hopkins G, Sohaey R, Winkler C, Sahn C S, Sovinsky V, Li X K and Sahn D J 2004 Fetal ventricular mass determination on three-dimensional echocardiography - studies in normal fetuses and validation experiments *Circulation* **110** 1054-60.

Baule G and McFee R 1963 Detection of the magnetic field of the heart. *Am. Heart J* **66** 95-6.

Brisinda D, Comani S, Meloni A M, Alleva G, Mantini D and Fenici R 2005 Multichannel mapping of fetal magnetocardiogram in an unshielded hospital setting Prenatal Diagnosis 25 376-82.

Buchanan T A 1995 Pregnancy in preexisting diabetes *In:* Harris MI C C, Stern MP, Boyko EJ, Reiber GE, Bennett PH (ed.) *Diabetes in america. 2nd edition* Baltimore, MD: National Institutes of Health.

Carpenter R J, Deter R L and Park S K 1984 Sonographic estimation of fetal weight - the value of femur length in addition to head and abdomen measurements *Radiology* **150** 535-40.

Chaoui R, Hoffmann J and Heling K S 2004 Three-dimensional (3d) and 4d color doppler fetal echocardiography using spatio-temporal image correlation (stic) *Ultrasound in Obstetrics & Gynecology* **23** 535-45.

Clausen T D, Mathiesen E, Ekbom P, Hellmuth E, Mandrup-Poulsen T and Damm P 2005 Poor pregnancy outcome in women with type 2 diabetes *Diabetes Care* **28** 323-8.

Cohen D, Edelsack E and Zimmerman J 1970 Magnetocardiograms taken inside a shielded

room with a superconducting point contact magnetometer *Applied Physics Letters* **16** 278-80.

Comani S, Liberati M, Mantini D, Gabriele E, Brisinda D, Di Luzio S, Fenici R and Romani G L 2004 Characterization of fetal arrhythmias by means of fetal magnetocardiography in thee cases of difficult ultrasonographic imaging *Pace-Pacing and Clinical Electrophysiology* **27** 1647-55.

Coustan D R 1995 Gestational diabetes *In:* MI C C, Stern MP, Boyko EJ, Reiber GE, Bennett PH (ed.) *Diabetes in america. 2nd edition* Baltimore, MD: National Institutes of Health.

Cremer M 1906 ¨uber die direkte ableitung der aktionstrome des menschlichen herzens von oesphagus and ¨uber die elektrokardiogram des fetus *M¨unchener Medizinischen Wochenschrift* 811- 3.

Cooper M J, Enderlein M A, Tarnoff H and Roge C L 1992 Asymmetric septal hypertrophy in infants of diabetic mothers - fetal echocardiography and the impact of maternal diabetic control *American Journal of Diseases of Children* **146** 226-9.

Corrigan N, Brazil D P and McAuliffe F 2009 Fetal cardiac effects of maternal hyperglycemia during pregnancy *Birth Defects Research Part a-Clinical and Molecular Teratology* **85** 523-30.

Creasy R and Resnick R 1999 *Maternal-fetal medicine. 4th edition* Philadelphia WB Saunders.

Cremer M 1906 ¨uber die direkte ableitung der aktionstrome des menschlichen herzens von oesphagus and ¨uber die elektrokardiogram des fetus *M¨unchener Medizinischen Wochenschrift* 811- 3.

Cuffin B 1978 Of the use of electric and magnetic data to determine electric sources in a volume conductor *Ann Biomed Eng* 173-93.

Cuneo B F, Ovadia M, Strasburger J F, H. Zhao T P, Schneider J and Wakai R T 2003 Prenatal diagnosis and in utero treatment of torsades de pointes associated with congenital long qt syndrome *Am. J. Cardiol.* **91** 1395-98.

Czapski P, Ramon C, Huntsman L L, Bardy G H and Kim Y 1996 Effects of tissue conductivity variations on the cardiac magnetic fields simulated with a realistic heart-torso model *Physics in Medicine and Biology* **41** 1247-63.

de Araujo D B, Barros A K, Estombelo-Montesco C, Zhao H, da Silva A C R, Baffa O, Wakai R and Ohnishi N 2005 Fetal source extraction from magnetocardiographic recordings by dependent component analysis *Physics in Medicine and Biology* **50** 4457-64.

Delorme A and Makeig S 2004 Eeglab: An open source toolbox for analysis of single-trial eeg dynamics including independent component analysis *J Neurosci Methods* 9-21.

Durrer D, Dam R v, Freud G, Janse M, Meijler F and Arzbaecher R 1970 Total excitation of the isolated human heart *Circulation* **41** 899-912.

Ellison R C and Restieaux N J 1972 *Vectorcardiography in congenital heart disease* Philadelphia Saunders

Fee B and Weil W B 1960 Body composition of a diabetic offspring by direct analysis

American Journal of Diseases of Children **100** 718-9.

Fenster A, Landry A, Downey D B, Hegele R A and Spence J D 2004 3d ultrasound imaging of the carotid arteries *Current drug targets. Cardiovascular & haematological disorders* **4** 161-75.

Ferguson A S, Zhang X and Stroink G 1994 A complete linear discretization for calculating the magnetic-field using the boundary-element method *IEEE Transactions on Biomedical Engineering* **41** 455-60.

Firpo C, Hoffman J I E and Silverman N H 2001 Evaluation of fetal heart dimensions from 12 weeks to term *American Journal of Cardiology* **87** 594-600.

Gandhi J A, Zhang X Y and Maidman J E 1995a Fetal cardiac-hypertrophy and cardiac-function in diabetic pregnancies *American Journal of Obstetrics and Gynecology* **173** 1132-6.

Gandhi J A, Zhang X Y and Maidman J E 1995b Fetal cardiac hyertrophy and cardiac function in diabetic pregnancies *American Journal of Obstetrics and Gynecology* **173** 1132-6.

Gee A, Prager R, Treece G and Berman L 2003 Engineering a freehand 3d ultrasound system *Pattern Recognition Letters* **24** 757-77.

Grimm W, Sharkova J, Funck R and Maisch B 2003 How many patients with dilated cardiomyopathy may potentially benefit from cardiac resynchronization therapy? *Pace-Pacing and Clinical Electrophysiology* **26** 155-7.

Hadlock F P, Harrist R B, Carpenter R J, Deter R L and Park S K 1984 Sonographic estimation of fetal weight - the value of femur length in addition to head and abdomen measurements *Radiology* **150** 535-40.

Hamada H, Horigome H, Asaka M, Shigemitsu S, Mitsui T, Kubo T, Kandori A and K. Tsukada 1999 Prenatal diagnosis of long qt syndrome using fetal magnetocardiography *Prenat. Diagn* **19** 677-80.

Hamalainen M, Hari R, Ilmoniemi R J, Knuutila J and Lounasmaa O V 1993 Magnetoencephalography - theory, instrumentation, and applications to noninvasive studies of the working human brain *Reviews of Modern Physics* **65** 413-97.

Hämäläinen M S and Sarvas J 1989 Realistic conductor geometry model of the human head for interpretation of neuromagnetic data *IEEE Trans. Biomed. Eng.* **36** 165-71.

Hendler I, Blackwell S C, Treadwell M C, Bujold E, Sokol R J and Sorokin Y 2004 Does advanced ultrasound equipment improve the adequacy of ultrasound visualization of fetal cardiac structures in the obese gravid woman? *American Journal of Obstetrics and Gynecology* **190** 1616-9.

Horigome H, Shiono J, Shigemitsu S, Asaka M, Matsui A, Kandori A, Miyashita T and Tsukada K 2001 Detection of cardiac hypertrophy in the fetus by approximation of the current dipole using magnetocardiography *Pediatric Research* **50** 242-5.

Horigome H, Takahashi M, Asaka M, Shigemitsu S, Kandori A and Tsukada K 2000 Magnetocardiographic determination of the developmental changes in pq, qrs and qt intervals

in the fetus *Acta Paediatr* **89**.

Hornberger L K 2006 Maternal diabetes and the fetal heart *Heart* **92** 1019-21.

Houston L E, Odibo A O and Macones G A 2009 The safety of obstetrical ultrasound: A review *Prenatal Diagnosis* **29** 1204-12.

Ilmoniemi R J, Hämäläinen M S and Knuutila J 1985 The forward and inverse problems in the spherical model *In:* Weinberg H, Stroink G and Katila T E (eds.) *Biomagnetism: Applications and theory* New York: Pergamon Press.

Jens A J (ed.) 2012. *Child development - 13 edition*: Pearson.

Kahler C, Grimm B, Schleussner E, Schneider A, Schneider U, Nowak H, Vogt L and Seewald H J 2001 The application of fetal magnetocardiography (fmcg) to investigate fetal arrhythmias and congenital heart defects (chd) *Prenatal Diagnosis* **21** 176-82.

Kähler C, Schleussner E, Grimm B, Schneider A, Schneider U, Nowak H and Seewald H 2002 Fetal magnetocardiography: Development of the fetal cardiac time intervals *Prenat Diagn* **22**.

Kandori A, Miyashita T, Tsukada K, Horigome H, Asaka M, Shigemitsu S, Takahashi M, Terada Y, Mitsui T and Chiba Y 1999 A vector fetal magnetocardiogram system with high sensitivity *Review of Scientific Instruments* **70** 4702-5.

Kariniemi V, Ahopelto J, Karp J and Katila T 1974 The fetal magnetocardiogram *J Perinat Med* **2** 214–6.

Kleiner R, Koelle D, Ludwig F and Clarke J 2004 Superconducting quantum interference devices: State of the art and application's *Proceedings of the Ieee* **92** 1534-48.

Krupa A 2006 Automatic calibration of a robotized 3d ultrasound imaging system by visual servoing. *In:* IEEE, ed. Proceedings of the 2006 IEEE International Conference on Robotics and Automation: 4136-41.

Kybic J, Clerc M, Faugeras O, Keriven R and Papadopoulo T 2005 Fast multipole acceleration of the meg/eeg boundary element method *Physics in Medicine and Biology* **50** 4695-710.

Leeuwen P v, Lange S, Klein A, Geue D, Zhang Y, Krause H J and Gronemeyer D 2000 Assessment of intra-uterine growth retardation by fetal magnetocardiography *Proc. BIOMAG* 603-7.

Leuthold A, Wakai R and Martin C 1999 Noninvasive in utero assessment of pr and qrs intervals from the fetal magnetocardiogram *Early Hum Dev* 235-43.

Malmivuo J C and Plonsey R 1995 *Bioelectromagnetism- principles and applications of bioelectric and biomagnetic fields* New York Oxford Univeristy Press.

Mantini D, Hild K E, Alleva G and Comani S 2006 Performance comparison of independent component analysis algorithms for fetal cardiac signal reconstruction: A study on synthetic fmcg data *Physics in Medicine and Biology* **51** 1033-46.

Martin J A, Hamilton B E, Sutton P D, Ventura S J, Menacker F and Munson M L 2003 Births:

Final data for 2002 *National vital statistics reports : from the Centers for Disease Control and Prevention, National Center for Health Statistics, National Vital Statistics System* **52** 1-113.

Mazzeo J R 1994 Noninvasive fetal electrocardiography *Medical Progress through Technology* **20** 75-9.

Menendez T, Achenbach S, Beinder E, Hofbeck M, Klinghammer L, Singer H, Moshage W and Daniel W G 2001 Usefulness of magnetocardiography for the investigation of fetal arrhythmias *American Journal of Cardiology* **88** 334-+.

MeyerWittkopf M, Cook A, McLennan A, Summers P, Sharland G K and Maxwell D J 1996 Evaluation of three-dimensional ultrasonography and magnetic resonance imaging in assessment of congenital heart anomalies in fetal cardiac specimens *Ultrasound in Obstetrics & Gynecology* **8** 303-8.

Moorman A, Webb S, Brown N A, Lamers W and Anderson R H 2003 Development of the heart: (1) - formation of the cardiac chambers and arterial trunks *Heart* **89** 806-14.

Moorman A F M and Lamers W H 1994 Molecular anatomy of the developing heart *Trends in Cardiovascular Medicine* **4** 257-64.

Mosher J C and Leahy R M 1998 Recursive music: A framework for eeg and meg source localization *IEEE Transactions on Biomedical Engineering* **45** 1342-54.

Mosher J C and Leahy R M 1999 Source localization using recursively applied and projected (rap) music *Ieee Transactions on Signal Processing* **47** 332-40.

Mosher J C, Leahy R M and Lewis P S 1995 Matrix kernels for meg and eeg source localization and imaging. *In:* Acoustics, Speech, and Signal Processing, 1995. ICASSP-95., 1995 International Conference on: 2943-6 vol.5.

Mosher J C, Leahy R M and Lewis P S 1999 Eeg and meg: Forward solutions for inverse methods *IEEE Transactions on Biomedical Engineering* **46** 245-59.

Murkofsky R L, Dangas G, Diamond J A, Mehta D, Schaffer A and Ambrose J A 1998 A prolonged qrs duration on surface electrocardiogram is a specific indicator of left ventricular dysfunction *Journal of the American College of Cardiology* **32** 476-82.

Motulsky H M and Brown RE 2006 Detecting outliers when fitting data with nonlinear regression – a new method based on robust nonlinear regression and the false discovery rate, *BMC Bioinformatics*, 7:123.

Myerson S G, Montgomery H E, World M J and Pennell D J 2002 Left ventricular mass - reliability of m-mode and 2-dimensional echocardiographic formulas *Hypertension* **40** 673-8.

Nasellopaterson C, Natale R and Connors G 1988 Ultrasonic evaluation of fetal body movements over 24 hours in the human-fetus at 24 to 28 weeks gestation *American Journal of Obstetrics and Gynecology* **158** 312-6.

Nelson C V, Hodgkin B C and Gastonguay P R 1975 Dipole-moment of hearts of various species *Annals of Biomedical Engineering* **3** 308-14.

Oostendorp T F, Oosterom A v and Jongsma H W 1989a Electrical properties of biological tissues involved in the conduction of foetal ecg *Med. Biol. Eng. Comput.* 322-4.

Oostendorp T F, Vanoosterom A and Jongsma H W 1989b The effect of changes in the conductive medium on the fetal ecg throughout gestation *Clinical Physics and Physiological Measurement* **10** 11-20.

Oostendorp T F, Vanoosterom A and Jongsma H W 1989c Electrical-properties of tissues involved in the conduction of fetal ecg *Medical & Biological Engineering & Computing* **27** 322-4.

Peters M, Crowe J, Pieri J F, Quartero H, Hayes-Gill B, James D, Stinstra J and Shakespeare S 2001 Monitoring the fetal heart non-invasively: A review of methods *Journal of Perinatal Medicine* **29** 408-16.

Pieri J F, Crowe J A, Hayes-Gill B R, Spencer C J, Bhogal K and James D K 2001 Compact long-term recorder for the transabdominal foetal and maternal electrocardiogram *Medical & Biological Engineering & Computing* **39** 118-25.

Popescu E, Popescu M, Bennett T, Lewine J, Drake W and Gustafson K 2007 Magnetographic assessment of fetal hiccups and their effect on fetal heart rhythm *Physiol Meas.* **28** 665-76.

Popescu M, Popescu E-A, Fitzgerald-Gustafson K, Drake W B and Lewine J D 2006a Reconstruction of fetal cardiac vectors from multichannel fmcg data using recursively applied and projected multiple signal classification *IEEE Transactions on Biomedical Engineering* **53** 2564-76.

Popescu M, Popescu E A, Fitzgerald-Gustafson K, Drake W B and Lewine J D 2006b Reconstruction of fetal cardiac vectors from multichannel fmcg data using recursively applied and projected multiple signal classification *IEEE Transactions on Biomedical Engineering* **53** 2564-76.

Quartero H W P, Stinstra J G, Golbach E G M, Meijboom E J and Peters M J 2002 Clinical implications of fetal magnetocardiography *Ultrasound in Obstetrics & Gynecology* **20** 142-53.

Rizzo G, Arduini D, Capponi A and Romanini C 1995 Cardiac and venous blood flow in fetuses of insulin-dependent diabetic mothers: Evidence of abnormal hemodynamics in early gestation *American Journal of Obstetrics and Gynecology* **173** 1775-81.

Rizzo G, Arduini D and Romanini C 1992 Accelerated cardiac growth and abnormal cardiac flow in fetuses of type-i diabetic mothers *Obstetrics and Gynecology* **80** 369-76.

Sahn C S, Sovinsky V, Li X K and Sahn D J 2004 Fetal ventricular mass determination on three-dimensional echocardiography - studies in normal fetuses and validation experiments *Circulation* **110** 1054-60.

Sarvas J 1987a Basic mathematical and electromagnetic concepts of the bio-magnetic inverse problems *Phys Med Biol* **32** 11-22.

Sarvas J 1987b Basic mathematical and electromagnetic concepts of the bio-magnetic inverse problems *Phys. Med. Biol.* **32** 11-22.

Schlitt H A, Heller L, Aaron R, Best E and Ranken D M 1995 Evaluation of

boundary-element methods for the eeg forward problem - effect of linear interpolation *IEEE Transactions on Biomedical Engineering* **42** 52-8.

SE R, MB B, AA F, G H, PR K, I S, B T, M T, Vbra J, G W, C L, H E, D W, P M and H a P 2001. A biomagnetic instrument for human reproductive assessment. *In: Biomag2000 Proceedings 12th Int Confon Biomagnetism.*

Sekhavat S, Kishore N and Levine J C 2010 Screening fetal echocardiography in diabetic mothers with normal findings on detailed anatomic survey *Ultrasound in Obstetrics & Gynecology* **35** 178-82.

Stinstra J, Golbach E, van Leeuwen P, Lange S, Menendez T, Moshage W, Schleussner E, Kaehler C, Horigome H, Shigemitsu S and Peters M J 2002a Multicentre study of fetal cardiac time intervals using magnetocardiography *Bjog-an International Journal of Obstetrics and Gynaecology* **109** 1235-43.

Stinstra J, Golbach E, van Leeuwen P, Lange S, Menendez T, Moshage W, Schleussner E, Kaehler C, Horigome H, Shigemitsu S and Peters M J 2002b Multicentre study of fetal cardiac time intervals using magnetocardiography *BJOG : an international journal of obstetrics and gynaecology* **109** 1235-43.

Stinstra J G and Peters M J 2002 The influence of fetoabdominal tissues on fetal ecgs and mcgs *Archives of Physiology and Biochemistry* **110** 165-76.

Tan J, Silverman N H, Hoffman J I, Villegas M, Schmidt K G 1992. Cardiac dimensions determined by cross-sectional echocardiography in the normal human fetus from 18 weeks to term. *Am J Cardiol* **70** 1459-67.

Tao R, Popescu E-A, Drake W B, Jackson D N and Popescu M 2012a The effect of volume conductor modeling on the estimation of cardiac vectors in fetal magnetocardiography *Physiol. Meas.* 4.

Tao R, Popescu E-A, Drake W B, Jackson D N and Popescu M 2012b Effect of volume conductor on cardiac vector estimation in fmcg *Physiol. Meas.* 651-65.

Van Leeuwen P, Beuvink Y, Lange S, Klein A, Geue D and Gronemeyer D 2004a Assessment of fetal growth on the basis of signal strength in fetal magnetocardiography *Neurology & clinical neurophysiology : NCN* **2004** 47-.

van Leeuwen P, Beuvink Y, Lange S, Klein A, Geue D and Grönemeyer D 2004b Assessment of fetal growth on the basis of signal strength in fetal magnetocardiography *Neurology & clinical neurophysiology : NCN* 47.

van Leeuwen P, Hailer B, Bader W, Geissler J, Trowitzsch E and Gronemeyer D H W 1999 Magnetocardiography in the diagnosis of fetal arrhythmia *British Journal of Obstetrics and Gynaecology* **106** 1200-8.

van Leeuwen P, Lange S, Klein A, Gene D, Zhang Y, Krause H J and Gronemeyer D 2004c Reproducibility and reliability of fetal cardiac time intervals using magnetocardiography *Physiological Measurement* **25** 539-52.

Veille J, Hanson R, Sivakoff M, Hoen H and Ben-Ami M 1993 Fetal cardiac size in normal,

intrauterine growth retarded, and diabetic pregnancies *Am J Perinatol* **10** 275-9.

Veille J C, Sivakoff M, Hanson R and Fanaroff A A 1992 Interventricular septal thickness in fetuses of diabetic mothers *Obstetrics and Gynecology* **79** 51-4.

Visscher M O, Narendran V, Pickens W L, LaRuffa A A, Meinzen-Derr J, Allen K and Hoath S B 2005 Vernix caseosa in neonatal adaptation *Journal of perinatology : official journal of the California Perinatal Association* **25** 440-6.

Wakai R T, Leuthold A C, Cripe L and Martin C B 2000 Assessment of fetal rhythm in complete congenital heart flock by magnetocardiography *Pace-Pacing and Clinical Electrophysiology* **23** 1047-50.

Wakai R T, Leuthold A C and Martin C B 1998a Atrial and ventricular fetal heart rate patterns in isolated congenital complete heart block detected by magnetocardiography *Am. J. Obstet. Gynecol* **179** 258-60.

Wakai R T, Leuthold A C and Martin C B 1998b Atrial and ventricular fetal heart rate patterns in isolated congenital complete heart block detected by magnetocardiography *American Journal of Obstetrics and Gynecology* **179** 258-60.

Wakai R T, Strasburger J F, Li Z, Deal B J and Gotteiner N L 2003 Magnetocardiographic rhythm patterns at initiation and termination of fetal supraventricular tachycardia *Circulation* **107** 307-12.

Weber H, Copel J, Reece E, Green J and Kleinman C 1991 Cardiac growth in fetuses of diabetic mothers with good metabolic control *J Pediatr* 103-7.

Weissman A, Goldstick O, Geva A and Zimmer E Z 2003 Computerized analysis of fetal heart rate indices during oral glucose tolerance test *Journal of Perinatal Medicine* **31** 302-6.

Yagel S, Cohen S M, Shapiro I and Valsky D V 2007 3d and 4d ultrasound in fetal cardiac scanning: A new look at the fetal heart *Ultrasound in Obstetrics & Gynecology* **29** 81-95.

Zhang Z 1995 A fast method to compute surface-potentials generated by dipoles within multilayer anisotropic spheres *Physics in Medicine and Biology* **40** 335-49.

Zhao H and Wakai R 2002 Simultaneity of foetal heart rate acceleration and foetal trunk movement determined by fetal magnetocardiogram actocardiography *Phys Med Biol* **47** 839-46.

Zheng H R, Liu L L, Williams L, Hertzberg J R, Lanning C and Shandas R 2006 Real time multicomponent echo particle image velocimetry technique for opaque flow imaging *Applied Physics Letters* **88**.